Modeling and Measurement of the Maximum Pit Size on Ferrous Alloys Exposed to Atmospheric Conditions

---

A Thesis

Presented to the Faculty of the School of Engineering and Applied Science
University of Virginia

In Partial Fulfillment of the
Requirements for the Degree of
Master of Science (Materials Science and Engineering)

by

Mara Elizabeth Shedd
December 2012

APPROVAL SHEET

The dissertation is submitted in partial fulfillment of the

requirements for the degree of

Master of Science (Materials Science and Engineering)

Mara E. Shedd

Mara E. Shedd
(Author)

This dissertation has been read and approved by the examining Committee:

Robert G. Kelly

Dr. Robert G. Kelly
(Thesis Advisor)

James T. Burns

Dr. James T. Burns
(Committee Chair)

William E. Keene

Mr. William E. Keene
(Committee Member)

Accepted for the School of Engineering and Applied Science:

James H. Aylor

Dean, School of Engineering and Applied Science
December 2012

Abstract

Localized corrosion sites or pits form on stainless steels exposed to atmospheric conditions when a defect forms in the passive layer, leaving the material susceptible to corrosion and the development of local acidified environments. These pits can continue to propagate and serve as initiation sites for cracking, which can then cause failure of the material. A method to predict the maximum pit size that could develop on an alloy under certain environmental conditions is therefore desirable for the many applications of stainless steels. Recently, a computational model has been developed that can predict the maximum pit radius by analyzing the localized corrosion site as a galvanic couple, with the pit as the anode and the surrounding surface as the cathode. The amount of current that is supplied by the cathode, the amount of current necessary to maintain the anode, and the ohmic drop between the anode and the cathode all control stability of the localized corrosion site and place a limit on the size to which a pit can grow. Predicted model values have compared well to literature values of outdoor exposures out to twenty-six years.

The goal of this study was to evaluate the computational model by comparing predicted model values to pit depths observed on laboratory exposures, in which environmental conditions, such as relative humidity and temperature were controlled. In conjunction, the sensitivity of the model to several input parameters also was investigated.

Exposures of four ferrous alloys 304L, 316L, Custom 465, and Aermet with loading densities of 240 and 600 $\mu g/cm^2$ deposited sodium chloride and relative humidity 90 and 95% were performed. After a one year exposure, pit sizes were < 2 um for the

stainless steel alloys. On the Aermet exposures, large pit sizes > 200 μm were observed along with the occurrence of general corrosion.

To enhance the pitting process stainless steel alloys 304L, Custom, and 316L were studied with deposited ferric chloride and exposed to three relative humidity values of 98, 85, and 64%. The geometry of the thin electrolyte was studied by using several deposition methods. Smaller pit depths were found under drops of ferric chloride, while pit depths closer to the predicted pit values were observed under thin films. With decreasing relative humidity, general corrosion appeared on the 304L samples along with localized corrosion.

The input parameters examined include the pit stability product, the Tafel slope, the corrosion potential, the repassivation potential, and the deliquescence properties of the mixed salt. The repassivation potential and the deliquescence properties of the mixed salt were found to have the greatest effect on predicted model values.

Acknowledgements

I would first like to thank my advisor, Dr. Robert Kelly, for all his support and guidance while a graduate student as well as an undergraduate at the University of Virginia. I will be forever grateful for the countless opportunities he has given me. I would also like to acknowledge my other committee members, Dr. James Burns and Mr. William Keene for their assistance with my research.

At Virginia Tech, I would like to thank Dr. James Schiffbauer for his assistance with the focused ion beam. In addition, I would like to acknowledge all of the faculty and students in the Center for Electrochemical Science and Engineering who have helped me over the years. In particular, thanks to Jen Warner, Cortney Crane, Katie Fleming, and Amber Lass for making my time in CESE very enjoyable.

The financial support from Dan Dunmire, Director of Corrosion Policy and Oversight, US Office of the Secretary of Defense, is also gratefully acknowledged.

Most of all, I would like to thank my family and friends for all of their support. Having my family close by has been an added bonus of graduate school that I will always treasure. Finally, last but surely not least, I would like to thank Eric. Thank you for always believing in me and for all of your tremendous encouragement and support. I could not have done it without you.

Table of Contents

List of Tables

List of Figures

List of Symbols

a	pit radius
A	constant dependent on material and environment for power law
A	atomic weight
d_{pit}	pit depth
C_i	concentration
C_s	saturation concentration
D_i	diffusivity
E_{corr}	corrosion potential
E_L	potential at the edge of the cathode
E_{rp}	repassivation potential
F	Faraday's constant
G^{ex}	excess Gibbs energy
h	pit depth
i	current density
i_c	cathodic current density
i_{lim}	limiting current density
i_p	passive current density
i_{eq}	equivalent current density
I_c	net cathodic current
$I_{cath,max}$	maximum cathodic current
$I_{LC,\ min}$	minimum anodic current
k	rate constant
LD	loading density
m_{salt}	molality
MW_{salt}	molecular weight
n	constant dependent on material and environment for power law
n	number of electrons transferred
N_i	flux
OCP	open-circuit potential
P	pressure
r_{eq}	equivalent radius
$R_{c,min}$	equivalent cathode radius
$R_{pit,max}$	maximum predicted pit radius
RH	relative humidity
SCE	saturated calomel electrode
$S_{ceq,min}$	equivalent cathode area
t	time of exposure
T	temperature
WL	water layer thickness
x	pit depth
x_i	composition
ρ	density
κ	conductivity
γ_i	activity coefficient
μ_i	chemical potential

1 Introduction

Failure of landing gear in their airplanes due to cracking is a significant concern for the United States Air Force. Stainless steels have replaced the heavy metal coatings used on high-strength steel landing gear, due to their inherent high corrosion resistance. Stainless steels have low general corrosion rates, but under atmospheric exposure conditions, ferrous alloys can experience localized corrosion, in the form of pits or crevices at which cracking then initiates. Pit formation and propagation along with hydrogen uptake from the pits enhance crack formation in ferrous alloys.

Engineers use structural integrity calculations to predict cracking given a starting crack size, but have been unable to account for the damage accumulation from corrosion-induced surface flaws and hydrogen uptake in their calculations. Without this information, calculations could underestimate the potential damage that could occur. The damage input into the integrity calculations to account for corrosion under atmospheric conditions is pit size. The kinetics of pit growth are not well understood, however, making it difficult to predict damage accumulation from atmospheric corrosion. Two of the methods used to measure corrosion damage in the past, accelerated testing and full immersion, can be overly aggressive and thus make the calculations too conservative. No link between these methods and damage observed in the field has been obtained. Therefore, there is significant interest in a method to rank corrosion susceptibility of alloys to localized corrosion under atmospheric exposure conditions.

Power laws models have been developed to predict maximum pit sizes[1], by fitting exposure data for alloys exposed to an environmental condition and then extrapolating to longer times. For long service periods, though, power law estimates are impractical

because they do not account for physical limits on pit size. Small changes in the power law exponent also can lead to significant differences in pit size prediction.

A new method [2-3] uses the nature of atmospheric exposure to look at physical bounds on the pit size due to a coupling of environmental conditions and electrochemical behavior. In this model, the localized corrosion site is analyzed as a galvanic couple, with the pit as the anode and the surrounding surface as the cathode. The amount of current that is supplied by the cathode, the amount of current necessary to maintain the anode, and the ohmic drop between the anode and the cathode all can control the stability of the localized corrosion site and place a limit on the size to which a pit can grow. Using this model, the maximum pit size that could develop on an alloy under atmospheric exposure conditions can be calculated and then input into structural integrity calculations for lifetime prediction.

The calculations to determine the maximum pit radius depend on several factors. The chemistry of the thin electrolyte and the exposure conditions can control the size to which a pit can grow. Different salt compositions affect the conductivity, water layer thickness, and the wetting behavior of the alloy, all of which impact the stability of the localized corrosion site. All of these factors are incorporated into the model and can be independently determined experimentally or with a chemistry modeling software. Other inputs into the model include the electrode kinetics of the anode and the cathode, both of which can be determined experimentally.

The intent of this work was to evaluate the accuracy of the computational model to predict pit radius values that correctly bounded values observed for controlled laboratory exposures. A series of experiments was performed to determine the input

parameters mentioned, necessary for predictions of maximum pit radius using the computational model, as well as the pit sizes observed on laboratory exposures. These results combined with research on the hydrogen uptake and cracking associated with pits then can be used to determine the corrosion susceptibility of ferrous alloys in the field.

2 Background

In this chapter, the mechanism of pitting in stainless steels will be explained, and the literature on modeling the size and shape of pits on ferrous alloys exposed to atmospheric exposure conditions will be discussed. A recent analytical model that has been developed to predict maximum pit sizes will be described, along with several components that influence pit growth and the literature that has validated preliminary predictions from the model. Lastly, the choice of the ferrous alloys for a controlled laboratory exposure to further validate the analytical model and the experimental methods to analyze the pit growth observed will be explained.

2.1 Mechanism of pitting

As mentioned in the introduction, stainless steels have a high corrosion resistance due to the passive layer that forms on the surface of the alloys. However, defects in the passive layer can leave the material vulnerable to the formation of local acidified environments that can prevent the repassivation and reformation of the passive layer. For stainless steels the formation of an acidified environment has been linked to the presence of manganese sulfide inclusions.[4-5] The oxidation of the inclusions to produce sulfates and thiosulfate or the dissolution of the inclusion to produce hydrogen sulfide was thought to produce this environment. However, Ryan et al. proposed that a chromium-depleted region exists around the inclusion leaving the material susceptible to pitting, and Webb et al. have found that deep and narrow inclusions lead to the initiation of pitting.[5-6]

Although the exact mechanism for the initiation of pitting is still being investigated, the propagation of pits is better understood.[7] Once a pit has initiated an

acidified environment is created in a localized area on the surface of the metal. At the bottom of the pit, metal dissolution produces metal cations as shown in Figure 2.1. These cations then undergo hydrolysis reactions that decrease the pH, creating a harsh environment. Also indicated in Figure 2.1, anions such as Cl^- migrate into the pit to maintain charge neutrality due to the increase in cations from the continuous dissolution of the metal, at approximately 40-50 mA/cm^2 for stainless steels.[8] The common cathodic reaction for pitting is oxygen reduction, but because of the acidic nature of the pit, oxygen becomes depleted, and the reaction is moved to the area outside of the pit on the surrounding surface. Thus during pitting, a separation of the cathode and anode occurs. The computational model uses this galvanic couple to predict the maximum pit radius, which will be further explained in later sections.

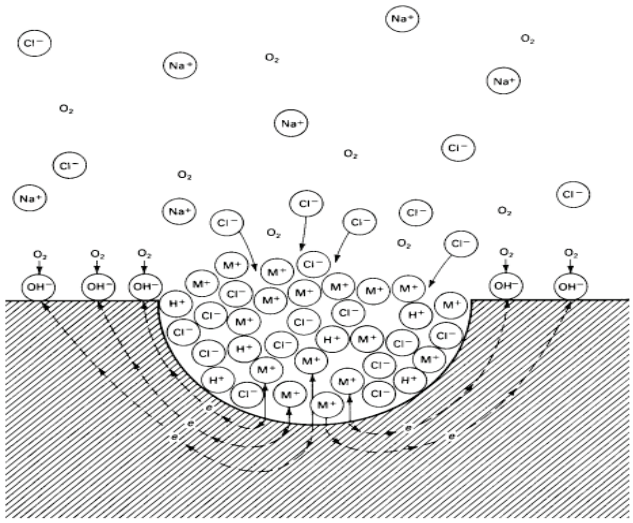

Figure 2.1 Schematic of the mechanism of pitting. Reproduction by permission of ECS – the Electrochemical Society.[7]

2.2 Early methods of predicting pit sizes

Pit growth has been difficult to model in the past. Power laws exist that predict pit size, but they have been found to be accurate predictors only in specific situations.

The literature on long-term exposures of stainless steels to marine environments suggests, however, that a maximum size to which a pit can grow exists. This knowledge combined with literature on the shape and morphology of pits on ferrous alloy exposures provides the foundation for the analytical model that will be discussed.

2.2.1 Power laws

Power laws were developed to predict the maximum pit depth that could form on an alloy as a function of time. Using fitted exposure data, Equation 2.1 is used to model the pit depth for a certain alloy and atmospheric exposure environment. In Equation 2.1, d_{pit} is the maximum pit depth, t is the exposure time, and A and n are constants that are specific to material and exposure condition.[1]

$$d_{pit} = At^n \qquad 2.1$$

Exposure data for four steels (Fe-11Cr, 403, 304, and Fe-25Cr-13Ni-0.8Mo) in three environments (a severe marine site, an industrial site, and a hot-spring site) are plotted in Figure 2.2.[1] For each site, the maximum pit depths found on panels, with area of 150 cm^2, are shown as a function of exposure period on a logarithmic scale. Constant m, equivalent to constant n in Equation 2.1, represents the dependence of the maximum pit depth on exposure time period. A correlation between exposure time and maximum pit depth was observed for the severe marine site, with an m value of approximately 0.60. However, for the hot-spring site, no dependence was observed between maximum pit depth and exposure period, with the maximum pit depths being obtained in the first year of exposure. In addition, although a large increase in pit depth was found over the course of the first year in the hot-spring area, the maximum pit depths only reached 100 μm, a relatively small pit size, and no further growth was observed over the next decade.

Lastly, these three sites show that any small changes in the coefficient will greatly impact the predicted maximum pit size.

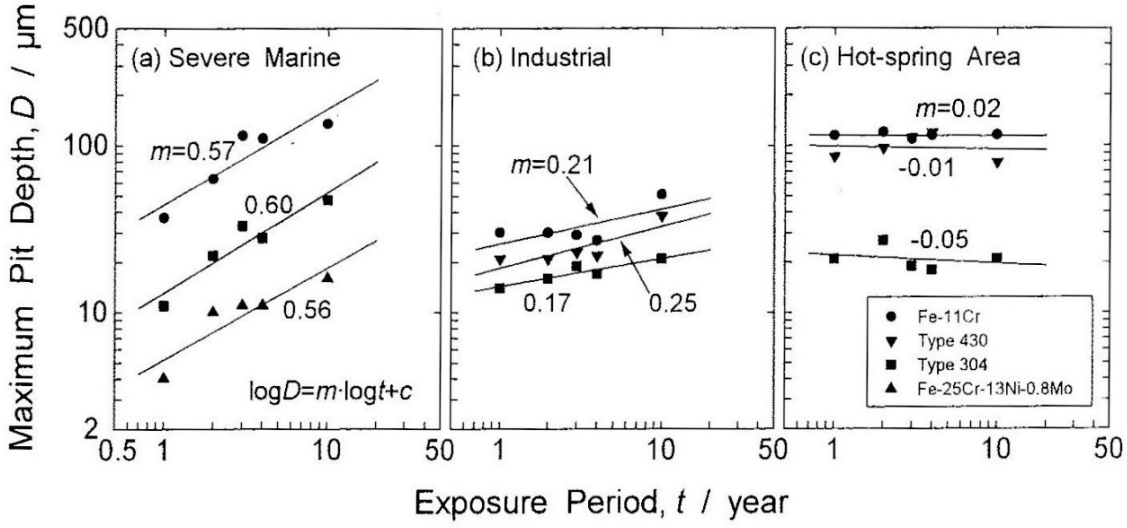

Figure 2.2 The dependence of maximum pit depth for four steels exposed to three environments, a severe marine, an industrial, and a hot-spring site on the length of the exposure period. With permission.[1]

Over the length of an exposure, power laws are useful for predicting maximum pit depth for a certain alloy and environment. However, it is impossible to apply such power laws to other materials and environments. Factors that control pit growth are not incorporated into a power law, so it can be challenging to modify them for the effect of changing material and environment. Power laws also ignore any physical limits on the size to which a pit can grow due to atmospheric exposure conditions. Therefore for an application that requires knowledge of pit sizes after long exposure periods, the extrapolation of power laws out to long times is not always an accurate method to determine these critical sizes.

2.2.2 Evidence of a maximum bound on pit size

The existence of a physical limit on the size to which a pit can grow is supported by the literature on atmospheric corrosion of ferrous alloys. In Nakata et al., pit depths on coastal exposures of 304L and 316L stainless steels were found to increase over five years and then plateau to a constant value over the next ten years.[9] Figure 2.3 shows this trend of an initial increase in pit depth followed by no significant increase in pit depth over the course of the next several years for 304L or 316L.

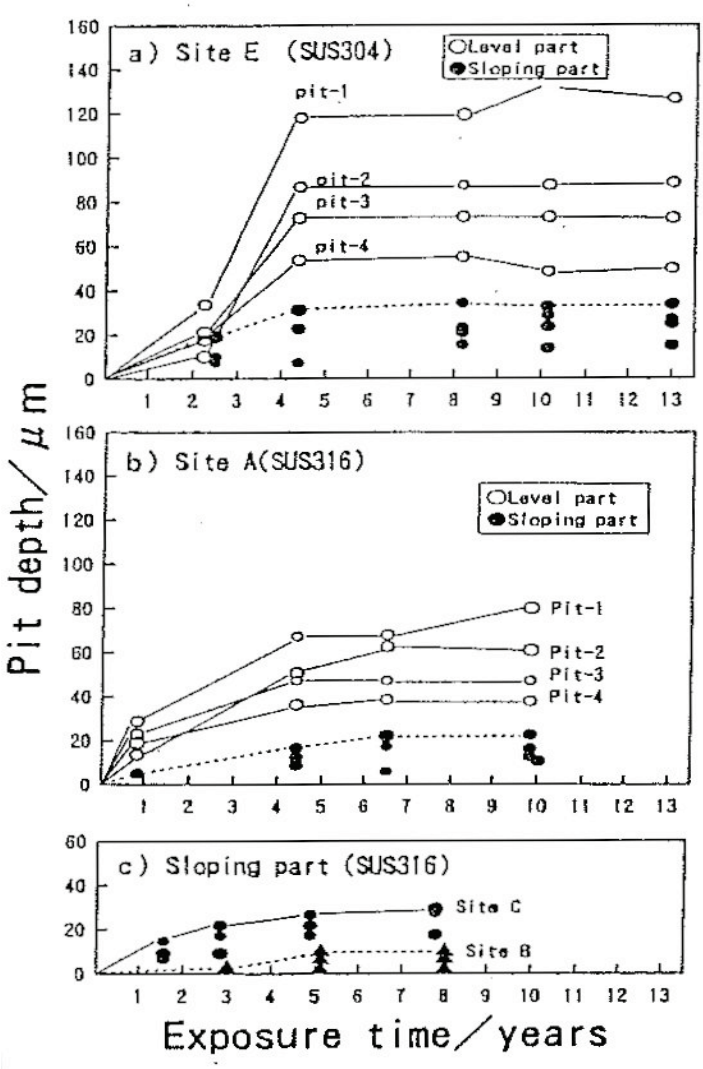

Figure 2.3 The plateau of maximum pit depth to a constant value over the course of thirteen years for 304 and 316SS exposed at different locations on the roof of a building. With permission.[9]

2.2.3 Shape of pits

The literature also supports the existence of a boundary on the shape to which a pit can grow.[10] Figure 2.4 shows the average pit depth as a function of average pit diameter for 304L coastal exposures at different levels of inclination on the eaves of a roof. A hemispherical pit has a ratio of pit depth-to-diameter of one-half. All of the exposures have a ratio equal to or less than this value, indicating that no tunneling was observed and that all pits were either hemispherical or pan-shaped. In Pistorius and Burstein, larger pits were found to be more pan-shaped.[11] The pits in Figure 2.4, however, began pan-shaped and eventually became more hemispherical with time. This trend will be investigated further in this study.

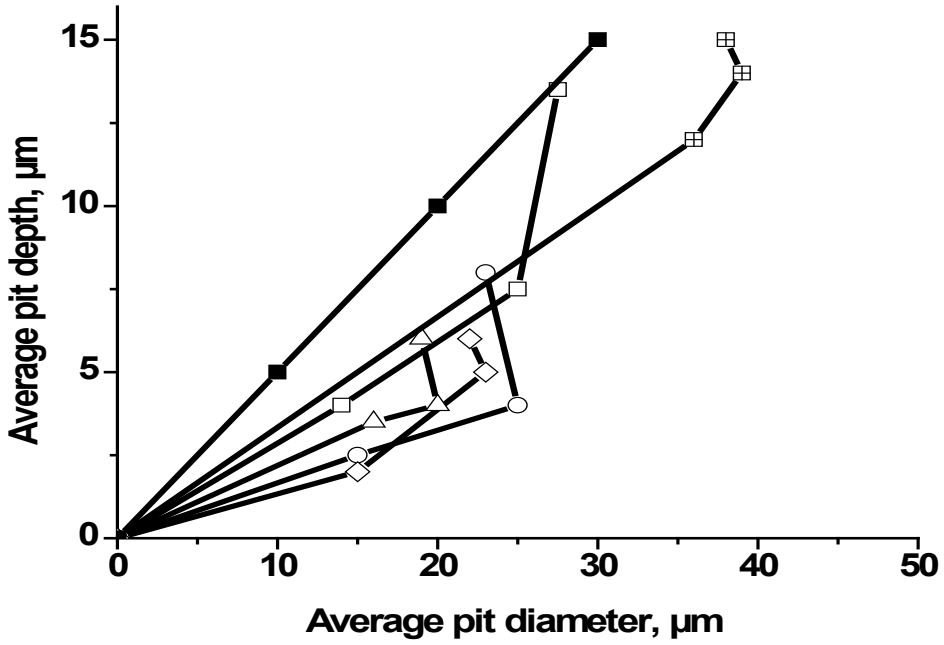

Figure 2.4 Coastal exposures of 304L at different levels of inclination on the eaves of a roof. Average pit depth is plotted versus average pit diameter, showing that the shape of pits was hemispherical or dish-shaped and no tunneling occurred. With permission.[10]

2.2.4 Lacy covering

Pits on stainless steels often are found to have lacy coverings, or a porous metallic cover, over the pits, as discussed in Ernst et al.[12] Lacy coverings inhibit mass transport of ions out of the pit, which as discussed in later sections prevents repassivation, enabling a pit to remain stable. Formation of a lacy covering occurs when the concentration at the mouth of the pits is less than the critical concentration of metal salts at the bottom of the pit, approximately 60-80% of saturation, and thus passivation occurs at the mouth of the pit. With further dissolution of the metal, this passivated surface becomes undercut, allowing ions to diffuse out of the pit. The area surrounding the pit again passivates and the cycle continues to repeat until a porous metallic cover is formed (Figure 2.5). Undercutting has been observed on stainless steel 304 in sodium chloride solutions, so its occurrence will be investigated on the alloys in this study. If undercutting is found to occur on these alloys, using the pit radius of the central hole to compare to the predicted model values may be an underestimation of the actual pit size.

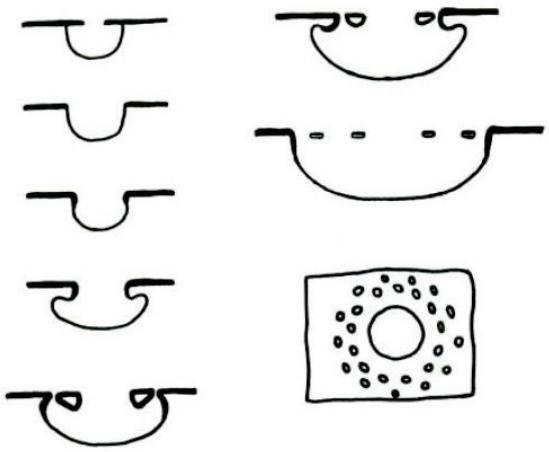

Figure 2.5 Schematic of the formation of a lacy cover. With permission.[12]

2.3 Analytical model

The application of the present research is the prediction of the service life of ferrous alloys out to very long times, but extrapolating the power law mentioned earlier to predict maximum pit sizes is considered unwise as they have not been validated for different exposure scenarios, and they do not have a firm physical foundation.[2] Therefore, a recently published computational model that uses the conditions that result from atmospheric exposures to place a bound on the size to which a pit can grow is more applicable for the goal of determining the maximum pit size that could develop on a ferrous alloy.[2-3]

In an atmospheric environment, a thin electrolyte layer containing salts from the air forms on the surface of the steels. The pit (as the anode) and its surrounding area (as the cathode) can be thought of as a galvanic couple. The stability of the pit and thus its ability to propagate is tied to the ability of the cathode to supply the necessary current to the anode. The cathode current capacity $I_{cath,\ max}$ is defined as the maximum current that can be supplied by the area surrounding the pit. The anode current demand $I_{LC,min}$ is defined as the minimum amount of current needed by the localized corrosion site to remain a critical chemistry at the base of the pit. For the pit to remain stable and to propagate, $I_{cath,max}$ must be greater or equal to $I_{LC,min}$. If $I_{cath,max}$ is less than $I_{LC,min}$ the pit will repassivate or stifle, in which only part of the pit will continue to grow. When $I_{cath,\ max} = I_{LC,min}$., the cathode is just able to supply the current needed by the anode, and the pit radius and thus overall size is at a maximum.

These conditions that determine a localized corrosion site's stability are shown in Figure 2.6. $I_{cath,max}$ is plotted versus $I_{LC,min}$, and the (x,y) coordinate on this plot is

determined by environmental factors, such as relative humidity, loading density of salt, and temperature. In the "anode control" region, $I_{cath,max}$ is larger than $I_{LC,min}$, and the cathode supplies more current than is needed by the anode. The pit is therefore stable, with all the cathodic current necessary to maintain a critical chemistry at the base of the pit. In the "cathode control" region, however, $I_{LC,min}$ is greater than $I_{cath,max,}$ and the cathode is unable to supply sufficient current to the anode. The pit, as mentioned before, will then repassivate or stifle. Lastly the condition for when $I_{cath,max}$ is equivalent to $I_{LC,min}$ is represented by the diagonal line. The anode has just the necessary current it needs to maintain stability, and the pit radius is at its maximum value.

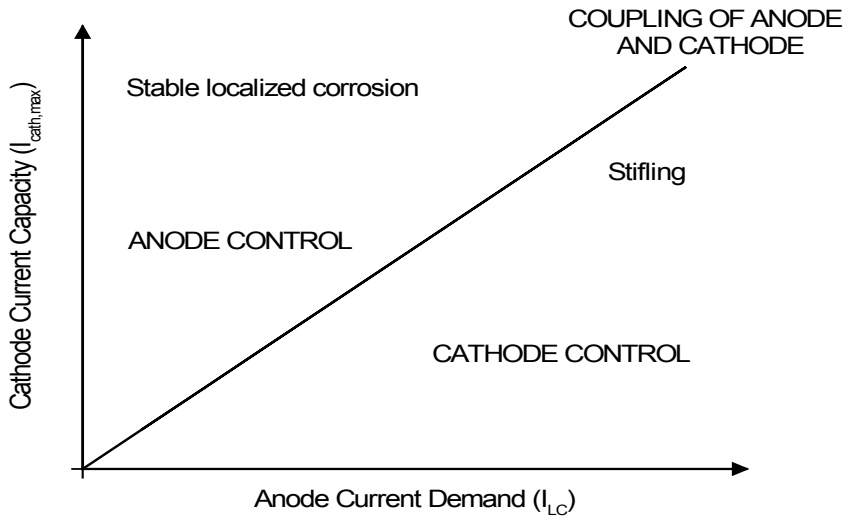

Figure 2.6 Schematic showing how different anode and cathode conditions affect the stability of the localized corrosion site. Reproduction by permission of ECS – the Electrochemical Society.[2]

The computational model predicts the maximum pit radius by equating $I_{cath,max}$ and $I_{LC,min}$ as a function of pit radius. An example of the model's output is shown in Figure 2.7. This plot predicts the maximum pit radius for 304L alloy exposed to 98% RH and a loading density of 100 μg/cm^2 sodium chloride. $I_{cath,max}$ and $I_{LC,min}$ are plotted as a

function of pit radius, and their intersection is equivalent to the maximum pit radius that could occur as discussed earlier. As observed in Figure 2.6, to the left of this interesection, $I_{cath,max}$ is greater than $I_{LC,min}$, and the pit is stable. However, to the right of this intersection, $I_{LC,min}$ is greater than $I_{cath,max}$, and the pit will repassivate. In the next two sections, Section 2.3.1 and 2.3.2, these two values, $I_{cath,max}$ and $I_{LC,min}$, will be further defined and the methodologies used to calculate them will be discussed.

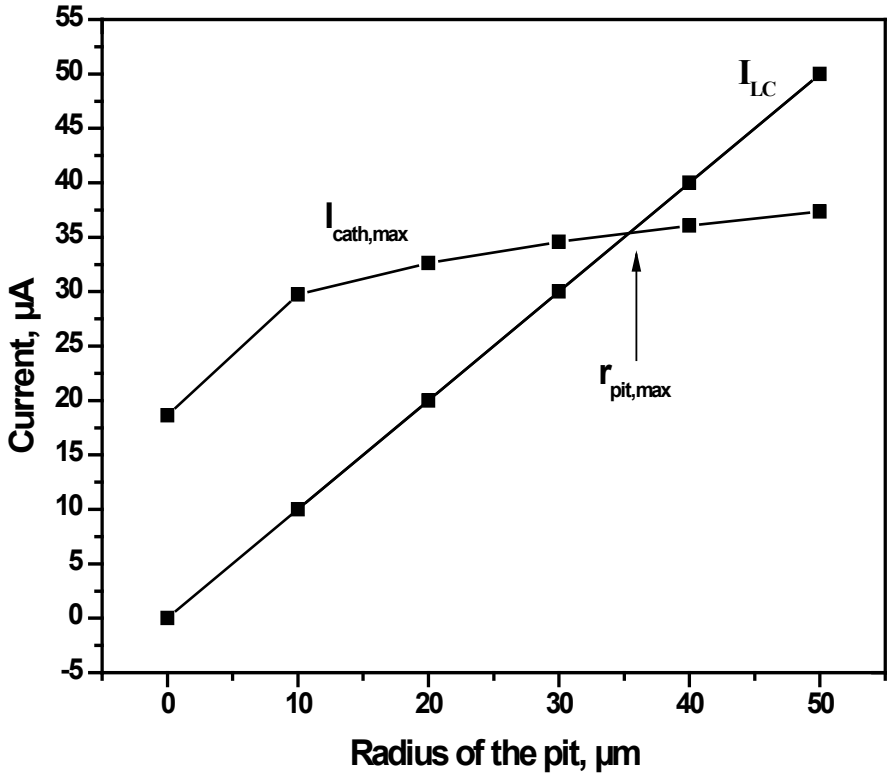

Figure 2.7 The coupling of $I_{cath,\ max}$ to $I_{LC,\ min}$ to determine the maximum pit radius using the computational model. Reproduction by permission of ECS – the Electrochemical Society.[2]

2.3.1 Anode current demand

The anode current demand or $I_{LC,min}$ is linked to the pit radius through the pit stability product, which Galvele determined is a critical value that must be exceeded to maintain a critical chemistry at the base of the pit and prevent repassivation and is

equivalent to the minimum anodic current divided by the pit radius.[13] Several models, in the past, predicted stability based on pH or composition. These models, however, do not accurately simulate the conditions within the pit. Pickering and Frankenthal, therefore, developed a model based on the diffusion and electrical migrations of ions that assumed pitting always occurred under acidified conditions.[14] Galvele later modified it to include four other assumptions, producing the stability model used today.[13] His first two assumptions are shown in Figure 2.8 and detailed in Equations 2.2 and 2.3.

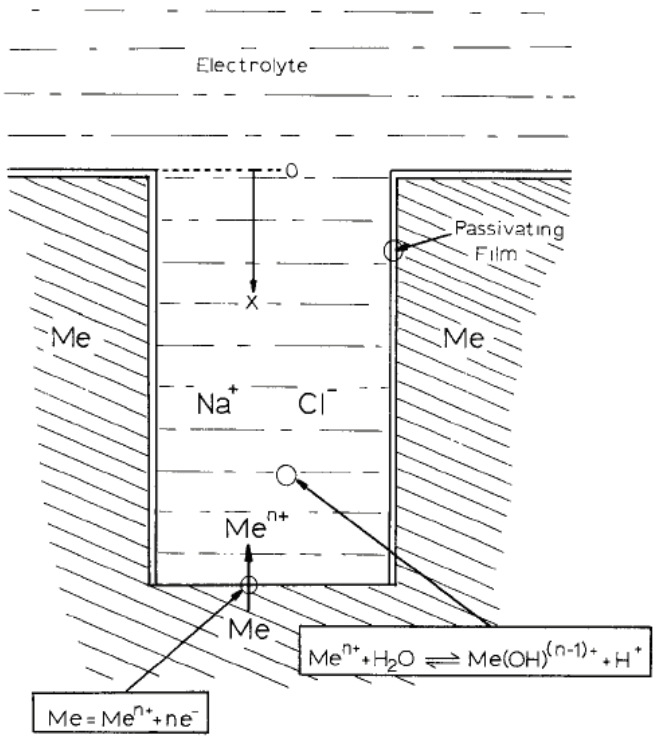

Figure 2.8 Galvele's one-dimensional pit model, showing the dissolution of the metal to form metal cations that then undergo hydrolysis. Reproduction by permission of ECS – the Electrochemical Society.[13]

Galvele's first assumption was that the metal undergoes a dissolution reaction at the base of the pit, in which metal cations and electrons are produced (Equation 2.2).

$$Me \leftrightarrow Me^{n+} + ne^{-} \qquad 2.2$$

Under his second assumption, these metal cations then undergo hydrolysis (Equation 2.3).

$$Me^{n+} + H_2O \leftrightarrow MeOH^{(n-1)} + H^{+} \qquad 2.3$$

The products of these two reactions are transported away, under diffusion control, from the pit by an aggressive anion salt in his third modification to Pickering and Frankenthal's model. Unlike their model, which assumed acidic pH values, Galvele's last assumption was that the pH could have any value. Thus because the pH could have alkaline values when determining the concentrations in Equations 2.2 and 2.3, the equations must be rewritten to include the additional OH^- ions at pH values higher than 7 (Equation 2.4).

$$2Me^{n+} + H_2O + OH^{-} \leftrightarrow 2Me(OH)^{(n-1)+} + H^{+} \qquad 2.4$$

An equation of flow for the species (Equation 2.5) with N_i the flux, D_i the diffusivity, and C_i the concentration and Equation 2.4 can then be used to calculate the concentrations of the ions.

$$N_i = -D_i \frac{dC_i}{dx} \qquad 2.5$$

Assuming steady state conditions and with the boundary condition of x=0 at the pit mouth to the pit bottom (x) the concentrations are calculated in Galvele and Vetter. [12,15] The resulting concentrations are linked to the pit stability product, with x the pit depth and i the current density by Equation 2.6, with k an equilibrium constant.[12] Using this

relation, the concentration of the ions can therefore be calculated, knowing the position and current density.

$$\frac{n*F*D_1}{*K_1} C_4 * C_5 + n * F * D_4 * C_4 = x * i + k \qquad 2.6$$

A specific pH value or concentration of H^+ ions is considered to be necessary to sustain an aggressive solution in the base of a pit exists for each metal. This value was determined for several metals by Galvele, using a Pourbaix diagram. By using the solubility product of the oxide film, he calculated the pH at which a solution containing metal ions would be in equilibrium with the oxide film. Using a metal ion concentration of 10^{-6} mol/L, iron, cobalt, and nickel were calculated to have a critical pH in the range of 9-10. Zinc has a critical pH of 8.7, while aluminum's is even lower at a pH of 5.

Using the an approximation of the current density of a one-dimensional pit at initiation of 1 A/cm^2 and the critical pH, the pit stability product or the x*i value at which stability is maintained in a localized corrosion site is shown for iron in Figure 2.9.[12] With a critical pH of 10, and a current density of 1 A/cm^2, the pit stability product is equivalent to 10^{-6} A/cm or 10^{-4} A/m for a pit. This pit stability product value, however, was developed for a one-dimensional pit, and thus cannot be directly used in the computational model of the present work because it assumes a hemispherical pit. The pit stability product value for a hemispherical pit is equivalent to I/r, which is simply x*i multiplied by a constant value to take into account geometry. This geometry calculation will be examined further in Section 2.4.1.

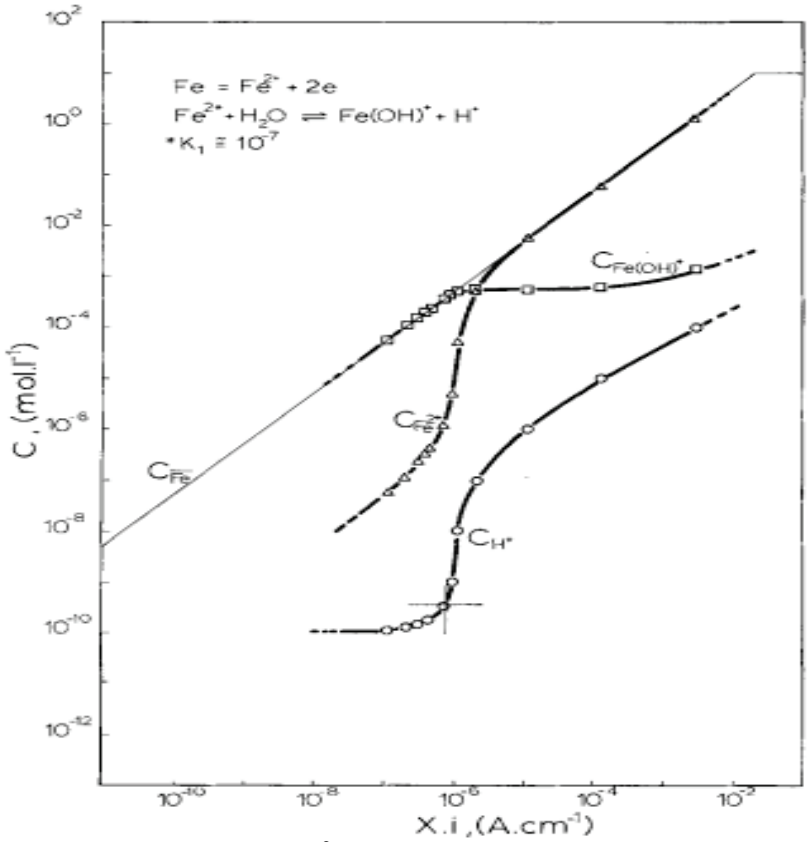

Figure 2.9 Concentrations of Fe, Fe^{2+}, $Fe(OH)^{+}$, and H^{+} as a function of x*I, with the critical pH and pit stability product marked with a + symbol. Reproduction by permission of ECS – the Electrochemical Society.[12]

In conclusion, the anode demand can be thought of as the pit stability product, linking the minimum anodic current to the pit radius as I/r. These values are then set equal to the cathodic current as a function of pit radius in order to predict the maximum pit radius that could develop on an alloy.

2.3.2 Cathode current capacity

Similarly to the anode current demand, the cathode current capacity, or the determination of the maximum cathodic current as a function of pit radius, can be determined by examining the cathode separately from the anode. The cathode, with a thin layer of electrolyte covering it and with a constant resistance, can be looked at as a real cathode with length L. The potential distribution for a real cathode is shown in

Figure 2.10. At the mouth of the pit, the potential is at its lowest value, E_{rp}, or the repassivation potential. The E_{rp} is the lowest potential at which stable pitting can still occur.[2] At further distances from the pit, the potential increases, eventually reaching the open-circuit potential of the alloy in the solution present on the surface. Beneath a plot of the potential the current density shows the opposite trend. The current density is at its highest value at the mouth of the pit, and decreases at further distances until there is no net cathodic current because it is all used to match the local passive cathodic current density.

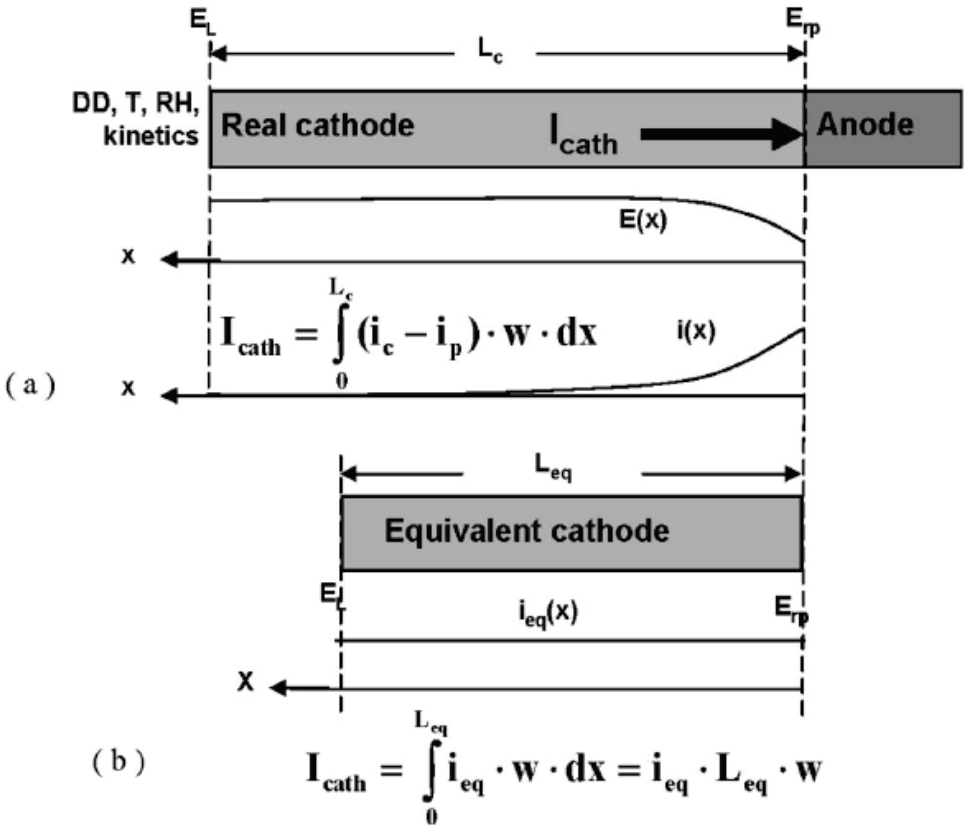

Figure 2.10 Schematic comparing the real cathode to the equivalent cathode. Reproduction by permission of ECS – the Electrochemical Society.[3]

The maximum cathodic current for a real cathode is equivalent to the spatial integration under the cathodic current density curve. Determining this integration can be difficult because it requires a detailed knowledge of the spatial distribution of the solution composition and electrochemical behavior and must be solved numerically, so an equivalent cathode can be used in place of a real cathode (Figure 2.10). The equivalent cathode has the same spatial integration as the real cathode, but it has a constant current density, called the equivalent current density. The equivalent current density is the average current density over a range of potentials, from E_L to E_{rp} (Equation 2.7). E_L is defined as the potential at the edge of the cathode (furthest from the pit) and E_{rp} as the repassivation potential. The two current densities in Equation 2.7 are the cathodic current density i_c and the passive current density of the cathode i_p.

$$i_{eq} = \frac{\int_{E_L}^{Erp}(i_c - i_p)dE}{E_L - E_{rp}} \qquad 2.7$$

To calculate the maximum cathode current, the equivalent current density is then input into Equation 2.8, where the total net cathodic current I_c is equivalent to the area of the cathode multiplied by the equivalent cathodic current density $i_{eq.}$

$$I_c = i_{eq}\pi r_{eq}^2 \qquad 2.8$$

Equation 2.9 is derived using equations 2.7 and 2.8 and several other equations to take into account the hemispherical shape of the pit. Though the derivations will not be discussed in detail for this study, they can be found in Chen and Kelly.[2] This equation provides the link between the maximum cathodic current to the pit radius. These values can then be used to determine the intersection with the minimum anodic current as shown in Figure 2.7.

$$\ln I_{c,max} = \frac{4\pi\kappa WL\Delta E_{max}}{I_{c,max}} + \ln\left[\frac{\pi e r_a^2 \int_{E_{corr}}^{E_{rp}} (i_c - i_p) dE}{\Delta E_{max}}\right] \qquad 2.9$$

To calculate the maximum cathodic current, several parameters are input into Equation 2.9. The maximum cathodic current is determined for a large cathode area, thus E_L approaches E_{corr}. Other parameters for the model, such as E_{corr} and I_{pass} are determined from cathodic polarization scans. Lastly, variables in the equation including the conductivity κ and the water layer thickness WL are determined analytically using the relative humidity (RH), temperature, and loading density of the deposited salt. All of these inputs will be discussed in the next section.

The equivalent cathode area is the area needed on an alloy exposed to specific environmental conditions to support $I_{cath,max}$. This value can be calculated using Equation 2.10, with $S_{ceq,min}$ as the equivalent cathode area and with many of the same input parameters used in Equation 2.9.

$$ln S_{ceq,min} = \frac{\frac{4\pi WL(\Delta E_{max})^2}{\int_{E_{corr}}^{E_{rp}} (i_c - i_p) dE}}{S_{ceq,min}} + (1 + \ln\pi + 2\ln r_a) \qquad 2.10$$

To calculate the equivalent cathode radius, $R_{c,min}$ Equation 2.11 is used.

$$R_{c,min} = \sqrt{\frac{S_{ceq,min}}{\pi}} \qquad 2.11$$

These two equations are useful for calculating the area that is needed to support a pit of a certain size and will be discussed further in several sections.

2.4 Determination of input parameters used in the model

Many of the input parameters into the computational model are determined experimentally, such as the pit stability product, the repassivation potential, and the cathodic kinetics. Others, including the water layer thickness and the conductivity, are

determined analytically using the chemical properties of salts modeled with OLI software. A background on all of the parameters mentioned will be presented in this section. Further detailed information on experimentally or analytically determining them will be presented in Section 4.

2.4.1 Pit stability product

As mentioned in Section 2.3.1, in the computational model, the pit stability product value, or I/r for a hemispherical pit, is equivalent to the anode current demand. Physically, it can be thought of as the degree to which the pit is occluded by its geometry to prevent diffusion out of the pit and thus dilution and repassivation. The pit stability product is measured using an artificial pit electrode methodology.[16-19]

The artificial pit electrode technique has its origins in the work of Tester and Isaacs,[20] who used the electrode to study the diffusion-controlled growth of a pit underneath a salt layer that formed at the metal interface. Also called the lead-in-pencil method, the artificial pit electrode is prepared by mounting a wire in insulated epoxy. Only a cross-sectional area of the wire is exposed and active, making calculation of current density easier as mentioned in Frankel.[21] When undergoing pitting, the entire area uniformly corrodes forming a one-dimensional pit that has a solution chemistry similar to that of a pit on an alloy.

The artificial pit electrode was later used in Gaudet and Newman to determine that activation-controlled growth of pits occurred at a specific potential and concentration of metal ions.[22] The two studies mentioned were further linked by Newman and Isaacs, who found that pitting occurred under both activation and diffusion-control.[23] Finally in Laycock and Newman, as well as in some earlier studies, the artificial pit electrode

technique was used to determine the pit stability produce of stainless steels 302 and 316.[16]

The detailed experimental method for determining the pit stability product will be discussed in Section 4.4, but a brief background on the experimental procedure and calculations to determine the value will be presented here. The experimental procedure presented in Laycock and Newman and later in Ernst and Newman to determine the pit stability product includes a potentiostatic hold at a high potential to first form the pit,[16,19] followed by a second potentiostatic hold at a lower potential to reduce noise in the last step, and lastly the voltammetry scan, over which the potential is scanned and the pit undergoes several of the transformations (Figure 2.11). Over the course of the scan, the pit first undergoes diffusion-controlled growth until pit growth transitions to the activation-controlled region at point a. From point a to point b, the salt film begins to thin and essentially disappears. The potential then is reversed and as it continues to increase, a salt film precipitates. Due to the ohmic drop of the salt film, the dissolution current density is now lower than it was at the beginning of the scan.

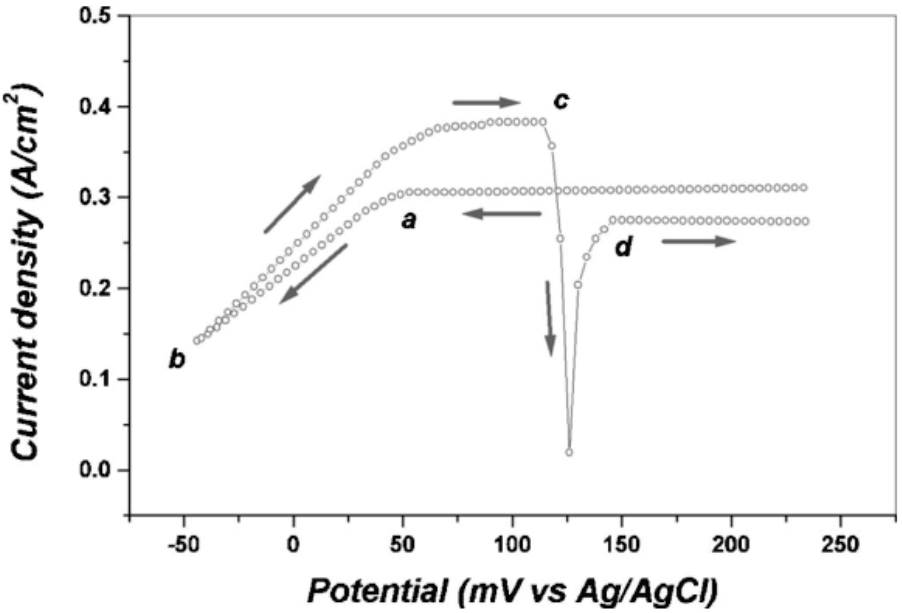

Figure 2.11 The cyclic voltammetry scan for a pit grown at +240 mV (Ag/AgCl) on 302 SS in 1 M NaCl at 40°C [ref]. The transition from diffusion to activation-controlled pit growth is observed at point a. The scan reverses at point b, and a salt film is precipitated at point c. Due to ohmic drop the dissolution current density is now lower at point d. Reproduction by permission of ECS – the Electrochemical Society. [17]

A large amount of information is contained in the voltammetry scan. However for determination of the pit stability product, only the limiting current density (i_L), or the current density as the pit transitions from diffusion-controlled growth to activation-control, is extracted for use. Before using the i_L in a calculation, diffusion-controlled growth is confirmed, as shown in Laycock and Newman, by plotting pit depth versus $1/i_{lim}$, as shown in Figure 2.12.[16] For this example of pit growth on stainless steels 316 and 302, diffusion-controlled growth is confirmed by a linear relationship between the two values.

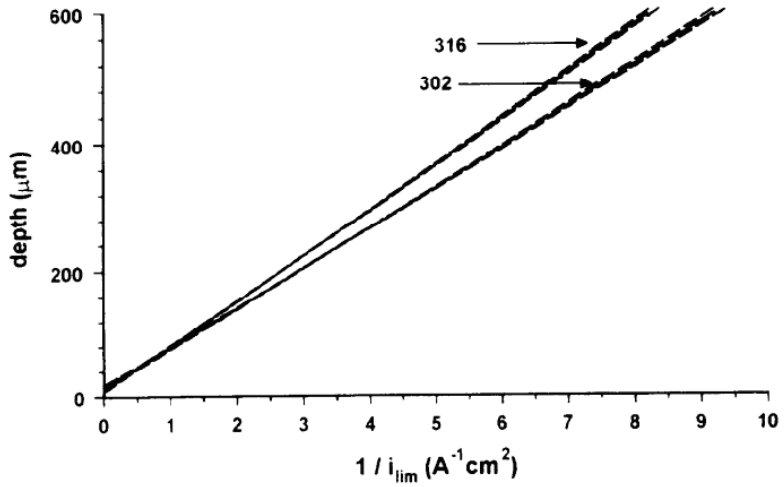

Figure 2.12 The linear relationship of pit depth to $1/i_{lim}$ confirming diffusion-controlled pit growth on 316 and 302SS. With permission.[16]

Once diffusion-controlled growth has been confirmed i_L along with the depth h, number of electrons transferred n, and Faraday's constant F are used in the calculation of the saturation concentration (Equation 2.12).[17]

$$DC_s = \frac{i_L h}{nF} \qquad 2.12$$

The depth is calculated using Equation 2.13, with A the equivalent atomic weight and ρ the density. The integrated charge is determined from the current vs. time plot for diffusion-controlled growth of the pit during the potentiostatic holds and for the voltammetry scan up until point a in Figure 2.12.

$$h = \frac{A}{nF\rho}\int i\, dt \qquad 2.13$$

The pit stability product is related to the concentration gradient, through Equation 2.14, with D the cation diffusivity, a the pit radius, I the anodic current density in the pit, and ΔC the concentration difference of cations between the base of the pit to its mouth.

$$D * \Delta C = \frac{2\pi}{3nF} * ia \qquad 2.14$$

Assuming all pits have a constant value of DΔC and that the concentration gradient outside of the pit is negligible, the saturation concentration determined in Equation 2.12 can be used in place of DΔC.

Using a similar method, values for the pit stability product for a one-dimensional pit for stainless steel 304 were found to range from 0.3 A/m to 0.6 A/m.[11] As mentioned earlier, for the computational model, values must be converted to take into account the hemispherical shapes of pits used in the model. For a hemispherical pit, the pit stability product is equivalent to I/r, which is calculated by multiplying the pit stability product by a constant value of 2π or 6.3, as shown in Equation 2.15. This constant is determined by accounting for a hemispherical area in Equation 2.12. The pit stability values for a hemispherical pit were found to range from 1 A/m to 3 A/m for stainless steels.

$$\left(\frac{3i_L h}{2\pi}\right) * 2\pi = \frac{I}{r} \qquad 2.15$$

2.4.2 Repassivation potential

The repassivation potential E_{rp}, as mentioned, is the potential at the mouth of the pit, and the lowest potential at which pitting still can occur. The E_{rp} has not been used as a critical potential for pitting in the past because it has been found to decrease with an increase in pit depth.[24-25] The determination of this potential by cyclic polarization scans with a fast scan rate or on a shallow pit have overestimated the value, while the E_{rp} determined for deeper depths has been too low. However, Sridhar et al. found that with increasing pit depth and charge density, the E_{rp} eventually reaches a constant value after the pit has reached deep enough values as shown in Figure 2.13.[26-29] The methodology used in this study included a potentiostatic hold to grow a pit, followed by a slow

cathodic scan. Potentiostatic holds were performed at varying lengths of time to obtain E_{rp} values for different depths. The repassivation potential was recorded for each as the potential when the current density reached 10^{-2} A/m^2. With increasing charge density and pit depth the E_{rp} decreased, but eventually leveled off at a constant value at large pit depths. An artificial pit electrode was used with the same electrochemical procedure described for this study. The procedure as found in Dunn et al. will be described in more detail in Section 4.3.[29]

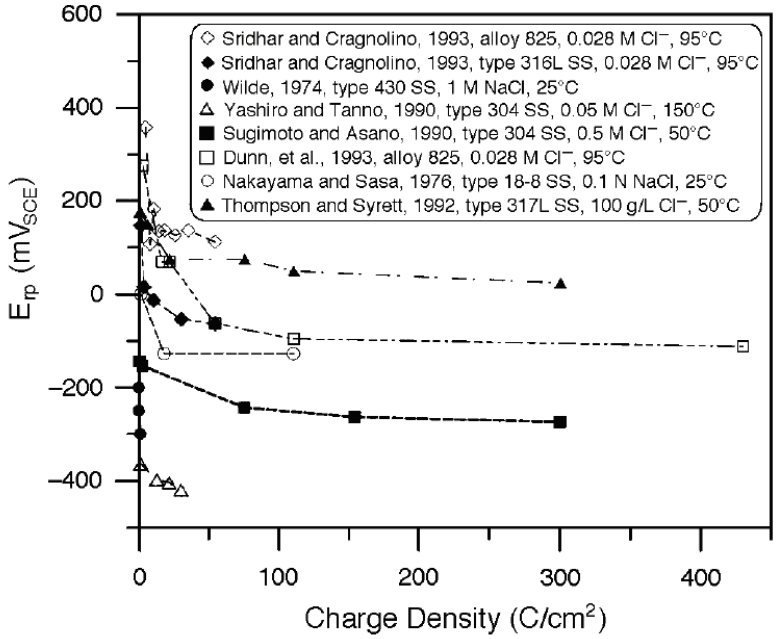

Figure 2.13 Literature values indicate repassivation potential levels off to a constant value at high charge density values. With permission.[29]

2.4.3 Cathodic polarization scans

A cathodic polarization scan is an electrochemical technique in which the potential is scanned from a potential above the corrosion potential down to a predetermined potential below the corrosion potential. The cathodic polarization scans performed for this study were scanned from -100 mV_{SCE} above the corrosion potential to

-900 mV_{SCE}. Several values, such as the corrosion potential and current density, are calculated from this polarization curve. For this study, these two values along with the Tafel slope were used to determine the integration in Equation 2.9. The polarization scan itself could also be used to determine the integration to determine the equivalent current density, which will be discussed further in future sections.

Cathodic polarization scans will be used in this study to determine the cathodic kinetics of ferrous alloys in various concentrations of salt, corresponding to the RH of the controlled laboratory exposure of the alloy. When a ferrous alloy with deposited salt on its surface is exposed to a particular RH value, the salt concentration on the surface will reach an equilibrium concentration. For sodium chloride solutions, experimental data such as that shown in Figure 2.14, can be found in the literature. Experimental values do not exist for other salts, so chemical relationships, such as concentration to RH, will be determined using OLI software.

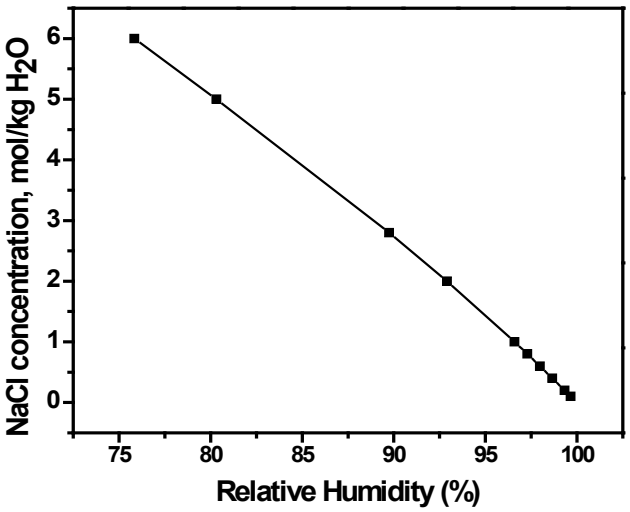

Figure 2.14 Literature values for the increase of sodium chloride concentration with the decrease in relative humidity. Reproduction by permission of ECS – the Electrochemical Society.[3]

2.4.4 Determination of water layer thickness

The deposited salt on the surface of the ferrous alloys is a thin electrolyte with a certain water layer thickness, WL. Chen and Kelly have developed Equation 2.16 to calculate the water layer thickness as a function of several parameters as shown.[2-3]

$$WL = \frac{LD(1+m_{salt}(RH,T)\times MW_{salt})}{m_{salt}(RH,T)\times\rho(RH,T)\times MW_{salt}} \qquad 2.16$$

The loading density LD, the molality m_{salt}, the density ρ, and the molecular weight MW_{salt} are used to analytically calculate the water layer thickness. Two of the parameters, the molality and the density, are dependent on the environmental conditions, such as the relative humidity and temperature. Therefore as mentioned in Section 2.4.3, the relationship between density and concentration to relative humidity are necessary to determine for calculation of the input parameters for the computational model.

2.5 Literature validation

After development of the computational model, the predicted model values were compared to literature values for outdoor marine exposures to confirm that it accurately bounded maximum pit sizes. A loading density of 600 μg/cm^2 sodium chloride was determined to be a realistic loading density for an outdoor exposure by comparison to data on loading density obtained for marine exposures in Japan[30] and used along with a RH of 98% in the model to calculate the predicted model values for both stainless steel 304 and 316. These values then were compared to outdoor exposures of 304, ranging from 0.4 to 13 years, and 316, ranging from 1 to 26 years (Figure 2.15 and 2.16). All of the predicted model values accurately bounded the literature values for pit depth.

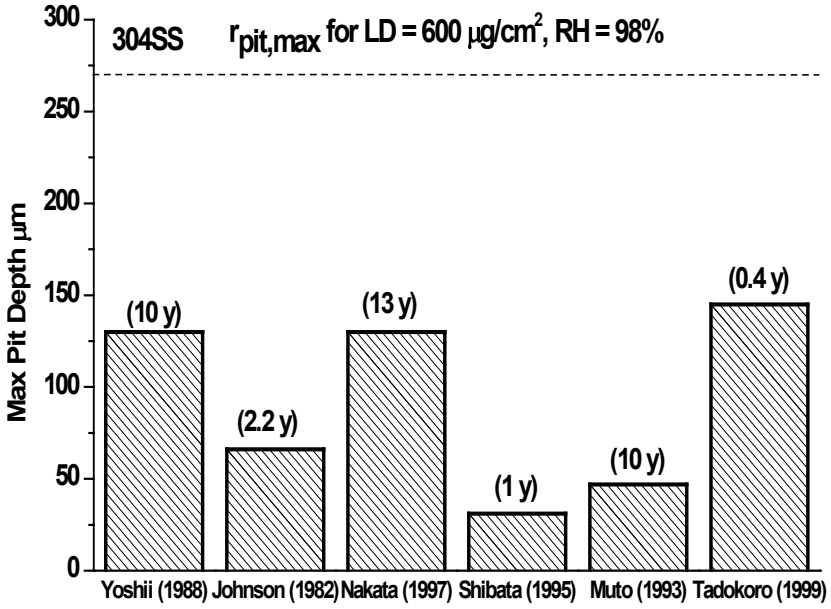

Figure 2.15 Validation of the computational model by comparison of the predicted pit radius to maximum pit depth found on long-term marine exposures for 304SS. Reproduction by permission of ECS – the Electrochemical Society. [2]

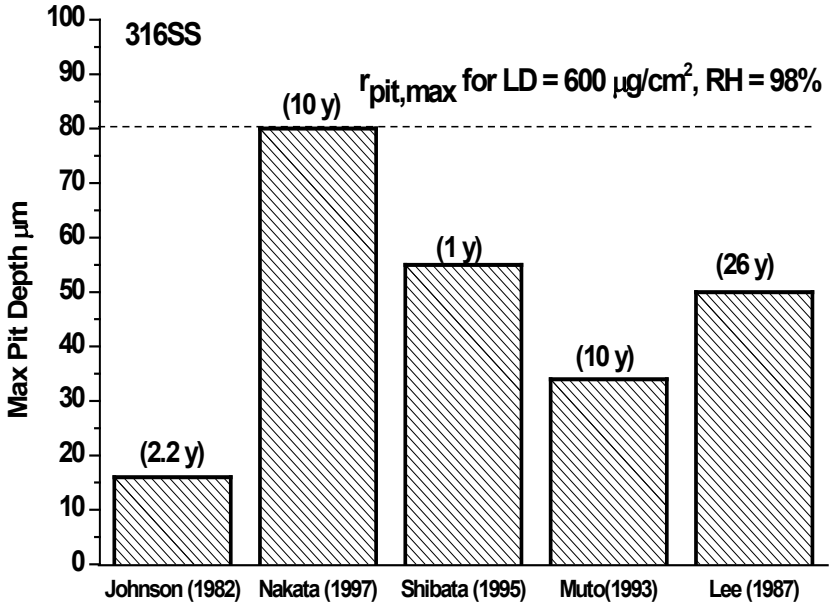

Figure 2.16 Validation of the computational model by comparison of the predicted pit radius to maximum pit depth found on long-term marine exposures for 316SS. Reproduction by permission of ECS – the Electrochemical Society.[3]

2.6 Analysis methods

A focused ion beam and a Hirox digital microscope were used to analyze the pits found on the surface of the exposures. A short background on each will be presented in this section.

2.6.1 Focused ion beam

A dual-beam focused ion beam set-up uses a combination of a focused ion beam and a scanning electron microscope. It can be used to cross-section pits on the surface of a metal to determine if undercutting of the surface exists and to determine the pit radius and depth. To cross-section a pit, the gallium ion beam is projected at an angle onto the surface, sputtering away enough material to achieve a cross-sectional image, created from the secondary ions and sputtering ions left on the surface. Using the high resolution imaging capabilities of the scanning electron microscope the sample then can be imaged to determine the size of pit and if any undercutting of the surface exists.

2.6.2 Hirox digital microscope

A Hirox digital microscope is useful for imaging pits on the surface of a metal because of its three-dimensional imaging capabilities. Using a step motor, the microscope is capable of taking images from the lowest focal plane to the highest and combining them to form a three-dimensional image. The z-resolution is approximately 1 μm for this instrument. Once the three-dimensional image is created for the pit, it can then be analyzed using surface analysis software, Mountains Map Imaging Topography 6.0. The exact procedure for determining pit depth will be explained further in Section 4.7.3 and Appendix A.

2.7 Chemistry modeling – OLI

As mentioned, determining the deliquescence properties of salt solutions is important in the accurate prediction of pit sizes with the computational model. In this study, OLI Systems Analyzer Studio 3.1 will be employed to model these properties using a mixed-solvent electrolyte thermodynamic model that is able to predict the properties of dilute electrolyte solutions to solutions at the fused salt limit. The model has the capabilities to simultaneously model vapor-liquid equilibria, solid-liquid equilibria, pH, and other thermodynamic properties.

Speciation, such as ion paring, acid-base reactions, and complexation accounts for the nonideality of electrolyte solutions and can have an effect on phase equilibria and the solubility of salt, both of which, as mentioned in previous sections, can impact the size to which a pit can grow.[31-32] The nonideality of the solution is the result of three effects: long-range electrostatic effects, middle-range interactions, and short-range interactions. The long-range electrostatic effects are represented in the model by the Pitzer-Debye-Huckel expression, which is dependent on the ionic strength of the solution and predicts the Coulomb interaction between ions.[31-33] The intermolecular interactions between all species in solution are included in the short-range interactions. These interactions are represented using the UNIQUAC expression, originally derived for nonelectrolyte solutions but applicable to a mixed-solvent electrolyte system as well. The middle-range interaction contribution includes the interactions between charged species not included in the long-range effect. In dilute electrolyte solutions, the long-range interactions dominate. For more concentrated electrolyte solutions, the short-range and middle-range interactions become important and must be included.[31-32]

Equations 2.17 and 2.18, for the excess Gibbs energy and for the activity coefficient, are developed to include the three interactions discussed and to predict the nonideality effects on equilibria.[34]

$$\frac{G^{ex}}{RT} = \frac{G^{ex}_{LR}}{RT} + \frac{G^{ex}_{II}}{RT} + \frac{G^{ex}_{SR}}{RT} \qquad 2.17$$

$$ln\gamma_i = ln\gamma_i^{LR} + ln\gamma_i^{MR} + ln\gamma_i^{SR} \qquad 2.18$$

The chemical potentials of the ions and neutral species for chemical equilibria are derived from Equation 2.19. The standard-state chemical potentials, μ_i^0, for aqueous species are determined from the Helgeson-Kirkham-Flower-Tanger equation of state, as a function of temperature and pressure.

$$\mu_i(T,P,x) = \mu_i^{\,0}(T,P) + RTlnx_i\gamma_i(T,P,x) \qquad 2.19$$

Reference state conversions must then be performed before chemical potentials are calculated. Finally, the model uses an algorithm to predict phase and chemical equilibria.

3 Objective

The objective of this study was to experimentally validate a computational model developed by Chen and Kelly to predict pit depths of ferrous alloys exposed to atmospheric conditions. Specifically, this study aimed to develop an experimental approach for controlled laboratory exposures that would accurately simulate the corrosion susceptibility of ferrous alloys to atmospheric corrosion in the field.

4 Experimental

This chapter discusses the methodologies followed for the laboratory experiments, including the material, solutions, and instruments used. The procedure for modeling the maximum pit size that could form on an alloy with Wolfram *Mathematica* 8 and Origin Pro 7.5 will be discussed, along with the chemical modeling of deliquescence properties with OLI Systems Analyzer Studio 3.1 software.

Four alloys were examined in this study for their corrosion resistance to pitting under atmospheric conditions, 304L, 316L, Custom 465, and Aermet 100. The alloys were used in two different forms. Coupons of the alloys were prepared for the study of the cathodic kinetics and for the laboratory exposures. For the artificial pit determination of the anodic kinetics, including the pit stability product and the repassivation potential, wires of material were used for the stainless steels while ribbon of material was used for Aermet.

4.1.1 Coupons for laboratory exposures

Coupons of the alloys were prepared from larger billets of steel. Samples of 316L and 304L with dimensions 2.4 x 2.4 cm were cut from a sheet of annealed material. A rod of as annealed Custom 465 was cut using a IsoMet 400 Linear Precision Saw into coupons with diameter 0.5 cm. Aermet was cut with the same saw from overaged material (950°F) into 1.5 x 2.5 cm rectangular coupons. Compositions for these alloys are listed in Table 4.1 and 4.2.

4.1.2 Wires for artificial pit studies

Wires for the artificial pit studies were obtained from California Fine Wire for 304L and 316L, with a diameter of 50 μm. Custom 465 wire, with diameter 80 μm, was

obtained from Fort Wayne Metals. Aermet 100 wire was not available commercially and could not be manufactured from our material. Therefore, thin ribbon of Aermet, produced from the original material, was used instead of wire for this alloy. The procedure for preparing the ribbon will be discussed in Section 4.2.3. Lastly, the composition for the wires is listed in Table 4.3. The composition for the Aermet ribbon is as listed in Table 4.2.

Table 4.1 Composition of the stainless steels in plate or rod form, wt%[a]

Alloys	C	Mn	P	S	Si	Cr	Ni	Mo	Ti	Fe	N	Co	Cu
304L	.0300	1.72	.028	.016	.051	18.35	8.05	.19	--	71.42	.05	.07	.027
316L	.0300	2.16	.045	.0300	.75	16.40	10.26	2.00	--	69.17	.100	--	--
Custom 465	.0026	.01	.003	.0006	.01	11.53	11.01	.93	1.62	74.88	.002	--	--

a Source of data for 304L Metal Samples Co, for 316L Online Metals and analysis with x-ray fluorescence , and for Custom 465 Fry Steel Co.

Table 4.2 Composition of the high-strength steel plate, wt%[b]

Alloy	C	Mn	P	S	Si	Cr	Ni	Mo	Ti	Fe	Co
Aermet 100	.23	.019	.001	<.001	.02	2.78	10.89	1.21	.01	71.99	12.8
	Nb	Al	Cu	Pb	Sn	B	W	V			
	.009	.01	.009	<.005	<.005	0.002	<.010	<.005			

b Source of data for Aermet 100 Carpenter Co.

Table 4.3 Composition of the stainless steel wires, wt%[c]

Alloys	C	Mn	P	S	Si	Cr	Ni	Mo	Ti	Fe	Co	Nb	Ta	N
304 L	.0300	1.59	.036	.0010	.27	18.48	9.20	--	--	70.26	.13	.001	.001	.001
316 L	.0190	1.36	.030	.0287	.41	17.07	10.66	2.16	--	67.98	--	--	--	.05
Custom 465	.0047	.01	.003	<.0005	.02	11.56	10.98	.92	1.56	74.88	--	--	--	--

c Source of data for 304L and 316L California Fine Wire., for Custom 465 Fort Wayne Metals

4.2 Pit stability product

The anodic kinetics for the four alloys was examined by determining the pit stability product and the repassivation potential using an artificial pit method, in which a one-dimensional pit is grown on a wire electrode. For the pit stability product experiments, a similar electrochemical procedure was used for all the alloys, including a period of open-circuit potential monitoring, a potentiostatic hold at +700 mV_{SCE}, a potentiostatic hold at +450 mV_{SCE}, and a cyclic voltammetry scan. Slight adjustments to the procedure dependent on the alloy will be discussed in the following sections.

4.2.1 304L and 316L anodic kinetics

To begin the pit stability product experiments, wire samples were first prepared. A length of wire approximately 15 cm long was cut from a spool of wire of either 304L or 316L material. The wire was then wrapped around the end of an insulated copper wire and attached with nickel solder. Conductivity was checked with a ohmmeter. Wires were then mounted in Buehler Epothin epoxy resin (Figure 4.1) and left overnight to harden.

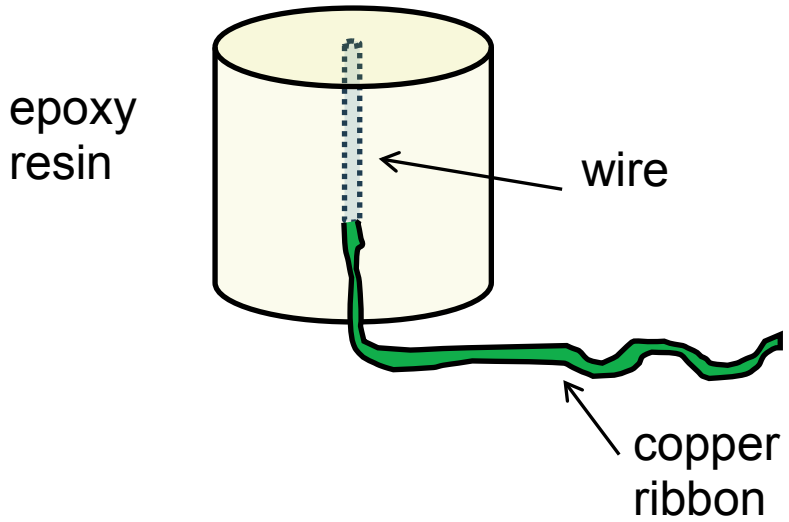

Figure 4.1 Schematic of the artificial pit electrode. Courtesy of Jayendran Srinivasan, University of Virginia.

After sitting overnight, the samples were polished to 600 grit. The exposed area was then rinsed with Millipore water, and the sample was mounted upright by attaching it to a glass support with a rubber band. The glass support with the sample attached was placed into a 300 mL beaker along with a saturated calomel reference electrode and a platinum wire mesh counter electrode. The 304L and 316L samples were tested in three concentrations of sodium chloride, 1, 1.5 and 2.6 M. All solutions were prepared with Fisher Scientific reagent grade chemicals.

Approximately 250 mL of solution was added to the beaker, and the electrochemical section of the experiment was begun using a Gamry PCI4 potentiostat. For the 304L alloy, the electrochemical procedure included a 10 minute open-circuit potential, a potentiostatic hold at +700 mV_{SCE} for 10 minutes, followed by a potentiostatic hold at +450 mV_{SCE} for 1 minute, concluding with a cyclic voltammetry scan from +450 mV_{SCE} to -50mV_{SCE} to +450 mV_{SCE}. The limiting current density was determined from the cyclic voltammetry scan (Figure 4.2) as the limiting current density before entering the active controlled regime part of the cyclic scan. The depth of the pit was calculated from the integrated charge from the potentiostatic holds and the cyclic voltammetry scan. These two values were entered into Equation 2.13 to determine the pit stability product for a one-dimensional pit. The pit stability product values for a one-dimensional pit were then multiplied by a constant value of 6.3, based on the geometry of the pit, to calculate the pit stability product for hemispherical pits.

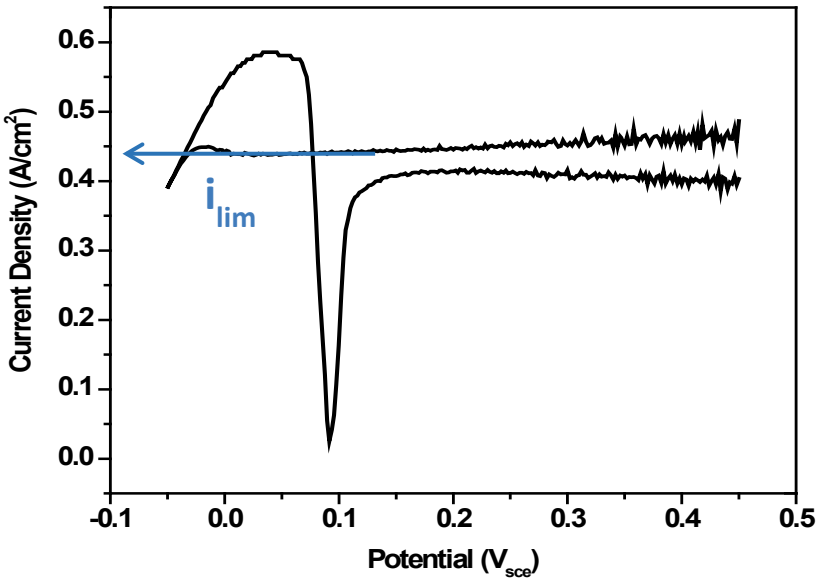

Figure 4.2 The cyclic voltammetry scan for a pit grown on a 304L sample at +700 mV_{SCE} in a 1.5 M sodium chloride solution. The limiting current density i_{lim} is the current at the transition from diffusion to activation-controlled pit growth and is used in the calculation of the pit stability product.

The procedure for the 316L alloy experiments was nearly identical. However for the 316L samples, the cyclic voltammetry scan was carried out from 450 mV_{SCE} to 0 mV_{SCE}. When the cyclic scan was run to -50 mV_{SCE}, the potential went too far into the active controlled regime and poor results were achieved for the reverse scan from -50mV_{SCE} to 450 mV_{SCE}. Though this section of the scan was not necessary for the determination of the pit stability product, a complete cyclic voltammetry scan was obtained by changing the reverse potential to 0 mV_{SCE}.

4.2.2 Custom 465 anodic kinetics

The same experimental procedure was followed for Custom 465. Samples were prepared from a spool of Custom 465 wire and then polished to 600 grit. The alloy was tested in 1, 1.5, and 2.6 M sodium chloride solutions. The electrochemical procedure was again similar to the one used for 304L, except the potentiostatic hold at +700 mV_{SCE} was

held for fifteen minutes compared to ten minutes for 304L. For Custom 465, the electrochemical procedure is as follows, a 10 minute open-circuit potential, a potentiostatic hold at +700 mV_{SCE} for 15 minutes, followed by a potentiostatic hold at +450 mV_{SCE} for 1 minute, concluding with a cyclic voltammetry scan from +450 mV_{SCE} to -50mV_{SCE} to +450 mV_{SCE}. Pit stability product values were then determined from these data.

4.2.3 Aermet 100 anodic kinetics

Aermet is not available in wire form, so material was produced from material at the University of Virginia. A rectangular coupon with dimensions 1.5 x 2.5 cm of Aermet material was polished down using using 60 grit paper to a thickness of approximately 150 μm. It was then cut using an Isomet slow speed saw to rectangular ribbons with dimension 300 μm x 300 μm x 1 cm. Some variation in width was observed between samples. A pure silver conductive epoxy was used to attach the strips of Aermet to a copper wire and left over night to harden. The next day the junction between the copper wire and the Aermet ribbon was wrapped with conductive copper tape and mounted in epoxy resin.

After preparation, the samples were polished to 600 grit. They were then imaged using an optical microscope, and the area of the sample was determined from this image using ImageJ software. Samples were tested in 1.5 and 2.6 M sodium chloride solutions. Like the other alloys, a similar electrochemical procedure was used for Aermet. The only difference in procedure is the potentiostatic hold at +700 mV_{SCE}, which for Aermet was held for six hours to grow a pit with depth two to three times that of the width. The electrochemical procedure for Aermet is therefore a 10 minute open-circuit potential, a

potentiostatic hold at +700 mV_{SCE} for 6 hours, followed by a potentiostatic hold at +450 mV_{SCE} for 1 minute, concluding with a cyclic voltammetry scan from +450 mV_{SCE} to -50mV_{SCE} to +450 mV_{SCE}. Data were collected and then used to calculate the pit stability product values.

4.3 Repassivation potential

The repassivation potential was studied using the same artificial pit method. The artificial pit method as mentioned in Section 2 is a modified version of the procedure used in Dunn et al.[29] The samples for the fours alloys were prepared in the same way as in Section 4.2. Before testing the samples were ground to 600 grit and mounted upright in a beaker. Tests for the repassivation potential were carried out in a 0.6 M sodium chloride solution, prepared from Fisher Scientific reagent grade chemicals. The electrochemical procedure for the experiment included an open-circuit potential for ten minutes, followed by a potentiostatic hold at varying lengths of time, then a potentiodynamic scan from +700 mV_{SCE} vs. Ref. to -800 mV_{SCE}. Vs. Ref. For Custom 465, the potentiostatic hold had length 10 minutes, 20 minutes, 30 minutes, and 60 minutes. For Aermet 100, the potentiostatic hold had length 15 minutes, 30 minutes, 1 hour, 3 hours, and 6 hours. Samples were then analyzed to determine the charged passed in C/cm^2. The repassivation potential was taken as the potential when the current was between 30-40 $\mu A/cm^2$.

4.4 Cathodic polarization scans

Cathodic polarization scans were performed for the four alloys to determine their cathodic kinetics in sodium chloride and ferric chloride solutions. The solution concentrations were chosen by using the relationship of concentration to relative

humidity for that particular salt. The concentration that corresponded to the relative humidity values of the exposures was chosen for the polarization scans.

For the sodium chloride exposures, cathodic polarization scans were performed in 1.5 and 2.6 M sodium chloride solutions, corresponding to 95 and 90% RH. Coupons of the four alloys were used and polished to 1200 grit. Samples were rinsed with Millipore water and acetone, and a 1 cm^2 area was exposed in a flat cell. A saturated calomel reference electrode was used with a platinum wire mesh as the counter electrode. All tests were carried out with a Gamry PCI4 potentiostat. The 304L, 316L, and Custom samples were exposed to a 24 hour open-circuit potential followed by a cathodic scan from +100 mV_{SCE} vs. OCP to -900 mV_{SCE}. Data was then exported to Gamry's Echem Analyst, and the E_{corr}, I_{corr}, and Tafel slope were determined using Gamry's software.

Cathodic polarization scans also were performed in 0.3, 1.4, and 2.8 M ferric chloride solutions, corresponding to 98, 85, and 64% RH. All conditions were the same for the ferric chloride scans except for sample size. Crevice corrosion was encountered when a 1 cm^2 area was exposed, so samples were cut down to smaller areas to prevent crevice corrosion from occurring. The area of the samples was determined by imaging the samples using an optical microscope and then using ImageJ software to measure the area. The rest of the procedure was identical to the sodium chloride scans for the ferric chloride solutions.

4.5 Laboratory exposures

Controlled laboratory exposures of the four alloys were performed under several environmental conditions. The four alloys were first exposed with deposited sodium chloride, with loading densities of 240 $\mu g/cm^2$ and 600 $\mu g/cm^2$ in 90 and 95% RH. The

effect of a thin film versus a drop was then investigated with ferric chloride exposures of 304L. Lastly, full immersion of 304L coupons also was performed.

4.5.1 Sodium chloride exposures

Coupons of the four alloys with dimensions as detailed in Section 4.1 were used for the laboratory exposures. Coupons were polished to three micron using diamond suspension. A cleaning procedure of sonication in distilled water for ten minutes, followed by acetone, and 2-butanone rinses was followed for each sample. The samples were then printed on using a salt-printing procedure as detailed in Schindelholz and Kelly,[35] with 1 M sodium chloride to reach the desired loading density levels of 240 $\mu g/cm^2$ and 600 $\mu g/cm^2$. After printing, samples were placed in controlled humidity glass chambers. A saturated solution of barium chloride was used to achieve a 90% RH and potassium nitrate to reach 95% RH. The samples were removed at five different exposures times, 1 month, 3 months, 6 months, and 1 year.

4.5.2 Ferric chloride exposures – drop

Coupons of 304L, 316L, and Custom 465 were prepared for the first ferric chloride exposure. They were polished to three micron using diamond suspension and then cleaned using a cotton ball, soap, and Millipore water, followed by an acetone rinse. A 1 M ferric chloride solution (Fisher Scientific reagent grade chemicals), filtered through a 0.45 μm Millipore Millex LCR filter, was used to print on the samples using the piezoelectric inkjet printer at the University of Virginia. A fifty micron orfice was used on the printer to deposit drops of a certain size on the surface of the sample. To determine the loading density, the drop size was measured using ImageJ software. Using the volume and the density of drops printed the loading density was calculated. For the

first exposure, a loading density of 100 μg/cm^2 ferric chloride was printed on the coupons over an area of 0.5 x 0.5 cm. After printing, the samples were put into a controlled relative humidity glass container with a saturated solution of potassium sulfate, for a RH of 98%. The coupons were removed at 100 hours, 504 hours, 696 hours, and 1032 hours.

The effects of loading density and relative humidity were investigated in separate experiments. Samples of 304L with loading densities of 250 μg/cm^2 and 400 μg/cm^2 ferric chloride were exposed to a RH of 98% for 168 and 336 hours. Lastly, one sample of 304L was exposed at a lower humidity 64% and with a lower loading density, 40 μg/cm^2 for 168 hours.

4.5.3 Ferric chloride exposures – thin film

Coupons of 304L were used for the thin film experiments. Samples were polished to three micron and cleaned with soap and Millipore water, followed by rinses in 2-butanone and absolute ethanol. An oxygen plasma asher, March PX250, was used to clean the samples to improve the wettability of the surface of the sample. The samples were placed in the plasma cleaner for one hour at 150W. After removal of the samples, a volume of ferric chloride was deposited on each sample, covering the entire 2.4 x 2.4 cm surface. The volumes deposited corresponded to three loading densities, 100, 250, and 400 μg/cm^2 for this drop experiment. Samples were put in glass containers and exposed to three relative humidity points, 98%, 85%, and 64%. The 98% samples were exposed for four days, while the 85 and 64% samples were exposed for three days.

After these initial exposures, to study the progression of pitting with time 304L samples were exposed with a thin film of loading density 250 μg/cm^2 ferric chloride in 85 and 98% RH. Samples were removed after 16 hours, 30 hours, 1 week, and 2 weeks.

4.5.4 Ferric chloride exposures – thin film vs. drop

A thin film and a drop of the same area were studied to investigate the effect of area on pit depth. In the previous experiments detailed a thin film and a drop were studied with the same loading density and volume. These, however, did not have the same area, and thus, depth is dependent on several factors. For the constant area experiments, the hypothesis that the depth is only dependent on the area was tested. All coupons were ground to three micron and cleaned using soap and Millipore water, followed by an acetone rinse. On the first set of coupons, a thin film and a drop were deposited covering the entire surface of a 304L coupon, with dimension 2.4 x 2.4 cm. To obtain the thin film, 18 μL of 0.3 M ferric chloride was deposited on the surface of the coupon. A microscope slide was placed on top of the drop, spreading the solution to the corners of the coupon. To obtain a large drop, 700 μL was deposited on the sample, covering approximately the same area as the thin film. Both samples were then placed in a glass container and exposed to a RH of 98%.

For the second set of coupons, a thin film and a drop with area 44.25 mm^2 were deposited on the two coupons. The thin film was obtained by depositing 4 μL of ferric chloride onto the sample. The bottom of a petri dish, 9 x 50 mm, was then placed on top of the drop, causing the solution to spread to an area of 44.25 mm^2. The same area was marked on the other 304L coupon, and 20 μL of ferric chloride was deposited, producing a drop with area 44.25 mm^2.

4.6 Model calculations

The predicted model values were determined using a combination of Mathematica and Origin software. The procedure followed is described in Sections 4.6.1 and 4.6.2.

4.6.1 Wolfgram *Mathematica* 7.0

A model was developed in *Mathematica* 7.0 based on Equation 2.10, setting the left and right sides of the equation equal and solving for the maximum cathodic current as a function of pit radius. The first step in solving the equation was to enter all of the known values. The water layer thickness and conductivity for a specific loading density and RH were determined using OLI software and then input into the model in *Mathematica*. The E_{corr}, i_{corr}, and Tafel slope, obtained by fitting a line to the cathodic polarization scans, were next input into the model. Finally, the repassivation potential determined from earlier experiments was entered into the model. After entering all of the values, the equation was solved in *Mathematica*, and values of cathodic current as a function of radius were calculated.

4.6.2 Origin Pro 6.5

Origin Pro 6.5 was used to plot the values of cathodic current as a function of pit radius. On the same graph, the pit stability product values, corresponding to the alloy and environmental conditions also were plotted. As mentioned in the Background, the intersection of these two lines corresponds to the maximum pit radius that could form on an alloy. This intersection was determined in Origin, by varying the axis values in order to observe the intersection on the graph. This point was then extracted and labeled the maximum pit radius that could form on an alloy under certain environmental conditions.

4.7 Analysis of exposure samples

The analysis of samples using a Focused Ion Beam and a Hirox Digital Microscope will be discussed in this section. The fitting of pit depth data to distributions using Minitab 16 also will be discussed.

4.7.1 Cleaning procedure

After the laboratory exposures, corrosion product was removed from 304L, 316L, and Custom 465, by dipping the samples in 10% concentrated nitric acid at 60°C for twenty minutes. Since Aermet is not a stainless steel, a nitric acid dip could not be used to remove corrosion product from its surface. In place of the nitric acid dip, Aermet samples were placed in a solution composed of 500 mL of hydrochloric acid, 500 mL of Millipore water, and 3.5 g of hexamethylene tetramine for ten minutes. After the corrosion product was removed from the samples, they were cleaned with soap and Millipore water, and then rinsed with acetone followed by ethanol.

4.7.2 Focused Ion Beam

Samples of 304L and 316L were analyzed at Virginia Tech using a FEI Helios 600 NanoLab Focused Ion Beam system. Using the SEM feature of the dual beam system, pits were located on the surface of the sample, and the surface was ion milled until a cross-section of the pit was observed.

4.7.3 Hirox Digital Microscope KH-7700

Aermet samples from the sodium chloride exposures and the samples from the ferric chloride exposures were analyzed using a Hirox Digital Microscope KH-7700. The general analysis procedure for all of the samples included using the multi-focus function on the Hirox Digital Microscope to create a three-dimensional image of the pit and using Mountains Map Imaging Topography 6.0 to calculate the depths of the pits.

For each sample, twelve areas on the sample were imaged, four areas each across the top, middle, and bottom of the sample. A high-resolution image was taken of each location, and the images were analyzed using Mountains Map to determine the maximum

depth of pits on the sample. In Mountains Map, an automated procedure was created that determined the maximum pit depth of each of the twelve areas. This procedure is described in more detail in Appendix A

The areas of the twelve spots analyzed on the samples are as follows. For the Aermet sample, the twelve spots had area 0.59 mm^2. For the ferric chloride drop experiments, the drop and immediate area around the drop were imaged, with area 0.16 mm^2. For the thin film, the twelve locations imaged had area 0.59 mm^2.

4.7.4 Minitab 16

Probability distributions were fit to the pit depth data obtained in Mountains Map using Minitab 16. For each alloy and each exposure time, the twelve pit depths were analyzed using Minitab's Individual Distribution Identification to determine the correct distribution to use to fit the data. For the Aermet exposures, the lognormal distribution was found to be the best fit, with a high p-value. The largest extreme value was found to have the highest correlation for the ferric chloride exposures. Histograms were created with the probability distributions for all of the pit depth data. These were used to determine the probability of obtaining certain pit depths on the surface of the alloys under specific environmental conditions.

4.8 OLI modeling

Modeling was performed using OLI Systems Analyzer Studio 3.1 to determine the deliquescence properties of both single salt mixtures and ternary salt mixtures. The procedure that was followed to generate data and plots for both mixtures will be detailed in Sections 4.8.1 and 4.8.2.

4.8.1 Binary salt mixtures

The deliquescence properties of single salt mixtures were determined for sodium chloride and ferric chloride using OLI Systems Analyzer Studio 3.1. The procedure that was followed for determining the chemical properties of a binary salt mixture is as follows. To a water stream, a salt was added at standard temperature and pressure, 25°C and 1 atm. The solution was then surveyed by composition from 0 to 7 mol of salt by 0.01 mol increments. The vapor pressure above the varying salt concentrations was monitored and displayed along with data such as the conductivity and density. To determine the relationship of concentration to relative humidity the vapor pressures corresponding to each concentration were divided by the vapor pressure over pure water and multiplied by 100 to obtain the relative humidity values.

Oxygen solubility cannot be determined using this method. To calculate oxygen solubility both oxygen and the salt were added to a water stream, at standard temperature and pressure, 25°C and 1 atm. The oxygen and salt concentrations were varied independently. The oxygen was varied from 0 to 1 mol, in 0.01 increments, while the salt was varied from 0 to 7 mol, in 0.01 increments. The amount of oxygen in the aqueous solution was then listed in the data output by the software.

4.8.2 Ternary salt mixtures

The deliquescence properties of ternary salt mixtures, in which there are two salts in water, also were determined using OLI Analyzer Studio 3.1. The procedure to determine the deliquescence point of the single salts and the mutual deliquescence point of both the salts is as follows. For the $NaCl$-NH_4Cl-H_2O mixture, sodium chloride and ammonium chloride were added to a stream of water, at standard temperature and

pressure, 25°C and 1 atm. The stream was then surveyed by the composition of sodium chloride, from 0 to 7 mol, in 0.01 increments. This survey was done as a precipitation survey, meaning the precipitation of a salt is calculated as the composition of sodium chloride is varied. A precipitation survey was performed twice for the two precipitates that could form in the solution, sodium chloride and ammonium chloride. The data from these two surveys was exported to Excel, where further calculations were performed.

For each of these surveys, the water activity was calculated and displayed as a function of composition of both sodium chloride and ammonium chloride. The composition of sodium chloride, originally output by the software in weight percent was converted to mole fraction, excluding water. The water activity was then plotted versus the mole fraction of sodium chloride for both surveys on the same plot. Their intersection corresponds to the mutual deliquescence point, while the points on either end of the plot correspond to the deliquescence point of each individual salt.

For the other two ternary systems modeled, $NaCl\text{-}FeCl_3\text{-}H_2O$ was surveyed by sodium chloride with precipitates sodium chloride and ferric chloride hexahydrate, while $NaCl\text{-}MgCl_2\text{-}H_2O$ was surveyed by sodium chloride with precipitates sodium chloride and magnesium chloride hexahydrate.

5 Results

Three necessary inputs into the model can be experimentally measured: the pit stability product, the repassivation potential, and the cathodic kinetics. Results for the four alloys for each of these experiments will be discussed. Predicted model values for the maximum pit radius as well as the maximum pit depth found on laboratory exposures also will be discussed. Finally, chemical modeling done using OLI Analyzer Studio 3.1 will be presented.

5.1 Pit stability product values

As discussed in Section 2.4.1, an experimental procedure was developed to determine the pit stability product of the fours alloys.[16-17] Diffusion-controlled growth was confirmed for each alloy by plotting the depth of the pit vs. $1/i_{lim}$. A linear relationship between these two values, as mentioned in the same earlier section, confirms diffusion-controlled growth of a pit.

The pit stability product was first determined for 316L in a 1 M sodium chloride solution. Values for the depth of the pit vs. $1/i_{lim}$ were compared to values found in Laycock and Newman.[16] The experimental values correlated well with the literature values, confirming an accurate experimental procedure and diffusion-controlled growth of a one-dimensional pit (Figure 5.1).

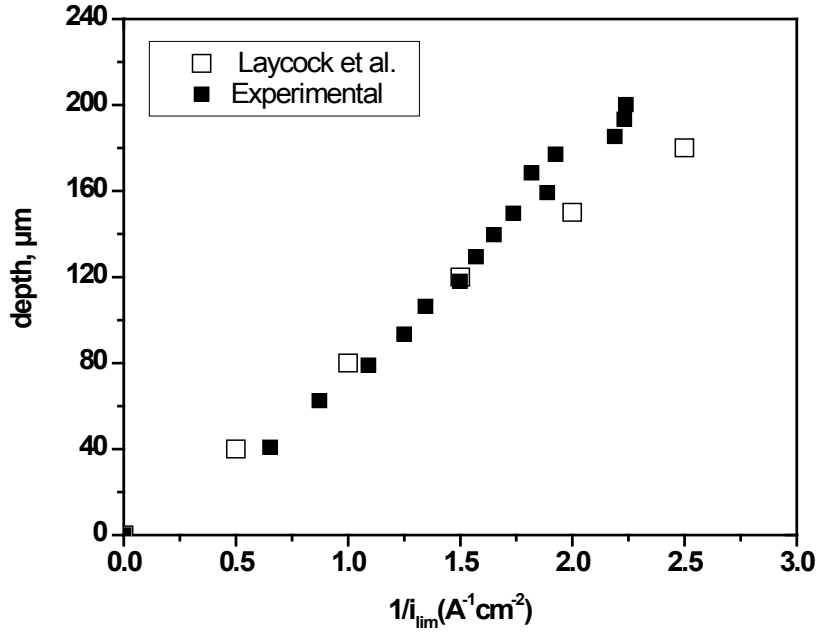

Figure 5.1 Comparison of experimental values for the pit depth versus $1/i_{lim}$ for 316L in a 1 M sodium chloride solution to literature values in Laycock et al.[16]

The fours alloys 316L, 304L, Custom, and Aermet were tested in 1.5 and 2.6 M sodium chloride concentrations, corresponding to 90 and 95% RH. 304L, 316L, and Custom were also tested in 1 M sodium chloride as preliminary experiments. For the 300-series stainless steels, the pit stability values fell between 1-3 A/m, as reported in the literature.[16]

For the 316L alloy, diffusion-controlled growth was confirmed in all three sodium chloride concentrations with a high correlation between pit depth and $1/i_{lim}$ with a R^2 value of 0.9914 for the 1.5 M sodium chloride solution (Figure 5.2). The pit stability product values for 316L ranged between 2 and 3 A/m (Figure 5.3).

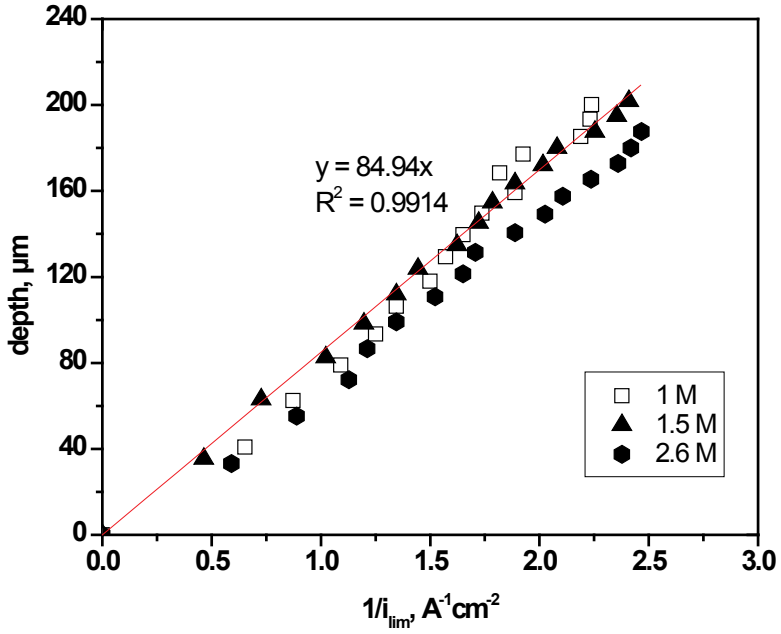

Figure 5.2 Confirmation of diffusion-controlled pit growth for 316L by plotting depth vs. $1/i_{lim}$ in 1, 1.5, and 2.6 sodium chloride solutions.

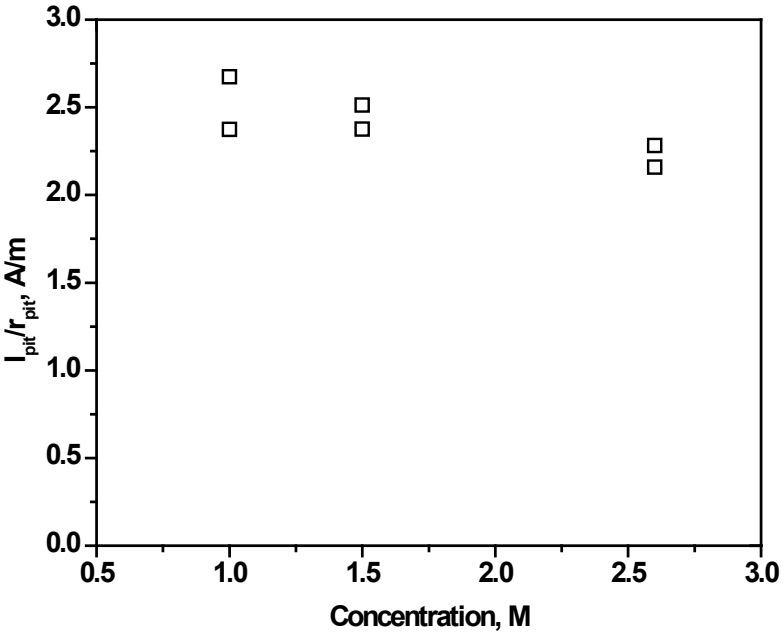

Figure 5.3 Pit stability product values for 316L in 1, 1.5, and 2.6 sodium chloride solutions.

Diffusion-controlled growth also was confirmed for 304L. An R^2 value of 0.9895 was calculated for the experiment in the 1.5 M sodium chloride solution (Figure 5.4). The pit stability product values for 304L were lower than 316L, ranging from 1-3 A/m for the three sodium chloride concentrations (Figure 5.5).

For the last stainless steel, Custom 465, a linear relationship between values of the depth and $1/i_{lim}$ was calculated with a R^2 value of 0.9959 in the 1.5 M sodium chloride solution (Figure 5.6). Values for the pit stability product ranged from 1.5 to 2.5 A/m and were similar to values determined for 316L (Figure 5.7).

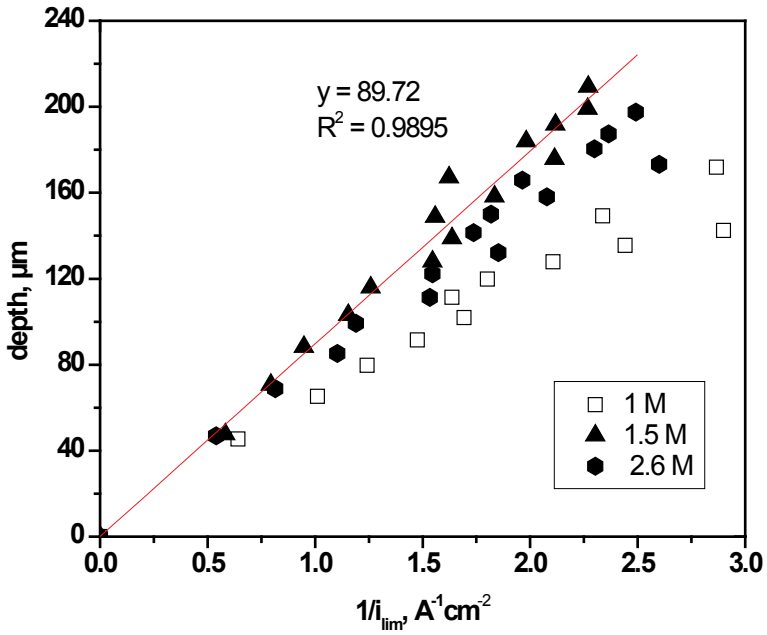

Figure 5.4 Confirmation of diffusion-controlled pit growth for 304L by plotting depth vs. $1/i_{lim}$ in 1, 1.5, and 2.6 sodium chloride solutions.

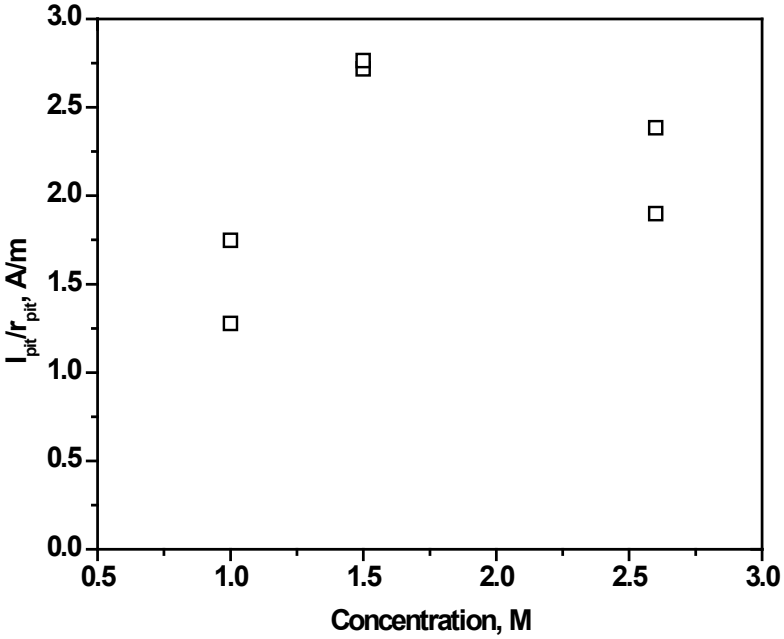

Figure 5.5 Pit stability product values for 304L in 1, 1.5, and 2.6 sodium chloride solutions.

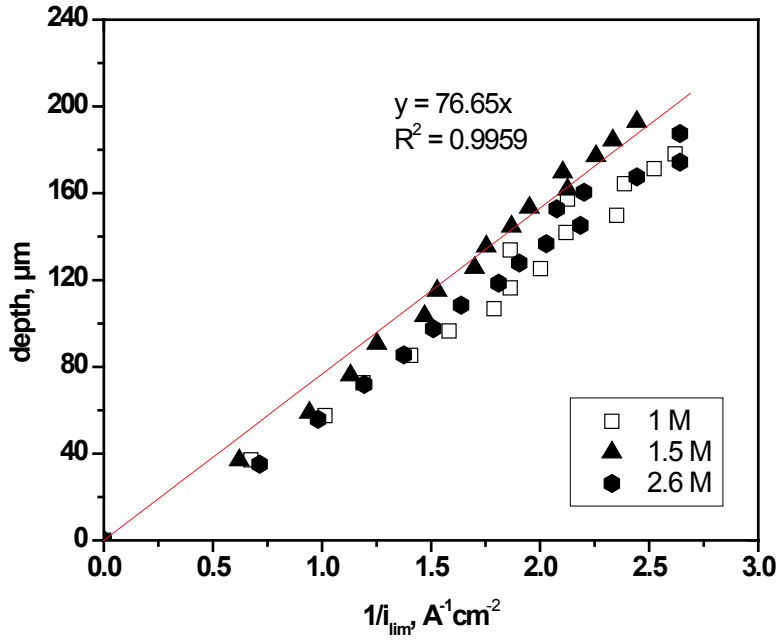

Figure 5.6 Confirmation of diffusion-controlled pit growth for Custom 465 by plotting depth vs. $1/i_{lim}$ in 1, 1.5, and 2.6 sodium chloride solutions.

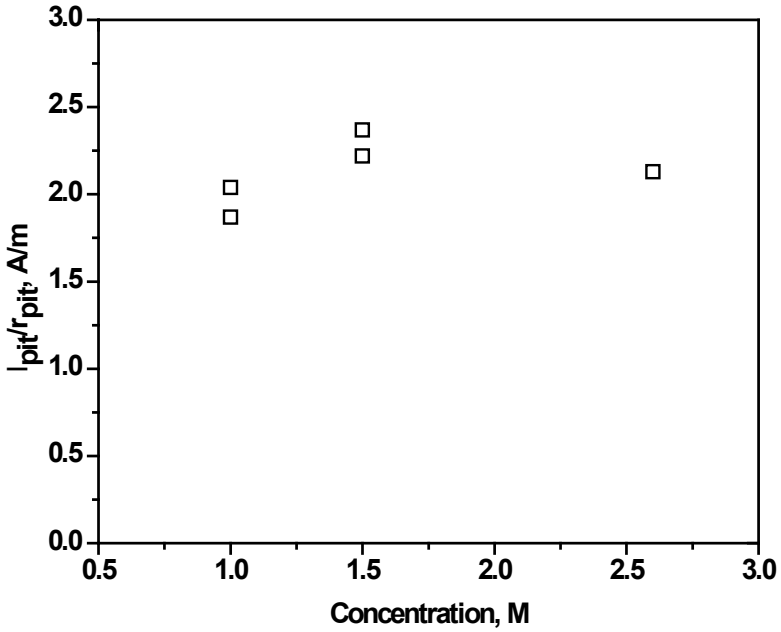

Figure 5.7 Pit stability product values for Custom 465 in 1, 1.5, and 2.6 M sodium chloride solutions.

Because Aermet could not be obtained in wire form, a ribbon of material was used in its place. Figure 5.8 shows the linear relationship between depth and $1/i_{lim}$ was not as strong for Aermet as it was for the other alloys in a 1.5 M sodium chloride solution. These results could be linked to the tendency of Aermet to undergo general corrosion as well as localized corrosion, which will be discussed in Section 5.5.2.

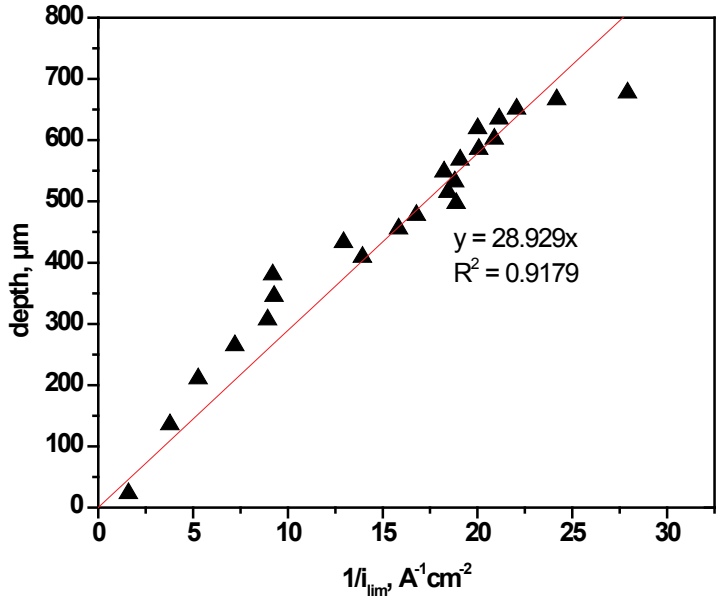

Figure 5.8 Confirmation of diffusion-controlled pit growth for Aermet 100 by plotting depth vs. $1/i_{lim}$ in a 1.5 M sodium chloride solution.

Pit stability product values obtained for Aermet were lower than they were for the other alloys, ranging between 0.5 and 1 A/m (Figure 5.9).

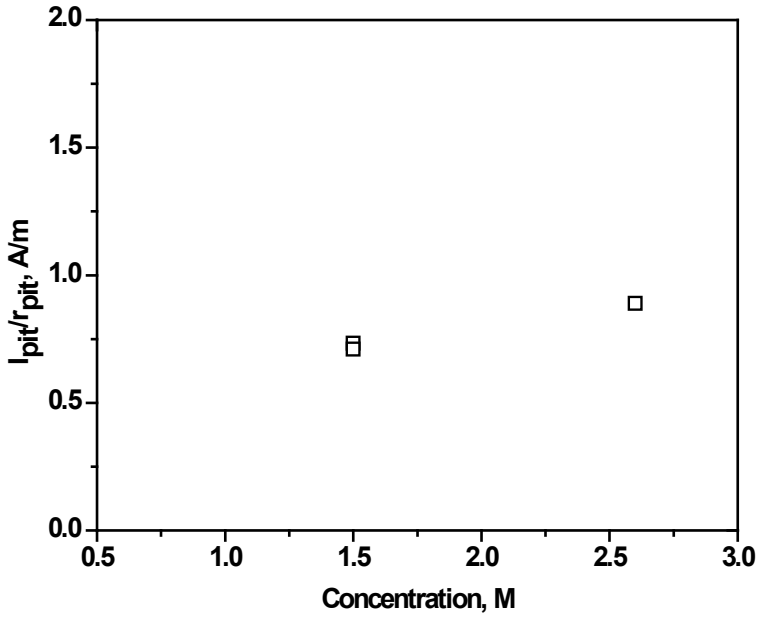

Figure 5.9 Pit stability product values for Aermet 100 in 1.5 and 2.6 M sodium chloride solutions.

5.2 Repassivation potential

The repassivation potentials (E_{rp}) for Custom and Aermet were determined by the artificial pit method, a procedure modified from a methodology found in Dunn et al. discussed in Section 2.4.2.[29] Based on previous research, as the charge density (C/cm^2) increases, the E_{rp} decreases, eventually leveling off after a sufficient amount of charge has been passed.[26] Custom 465 followed this trend. Its E_{rp} began high at -270 mV_{SCE}, with a charge density of 500 C/cm^2, then fell and leveled off at -430 mV_{SCE} and a charge density of 1200 C/cm^2 (Figure 5.10). The E_{rp} of Aermet did not follow a clear trend, with the potential varying widely with charge density from -418 mV_{SCE} to -576 mV_{SCE}. The inability to determine an E_{rp} for Aermet again could be linked to its tendency towards general corrosion, which will be discussed in later sections.

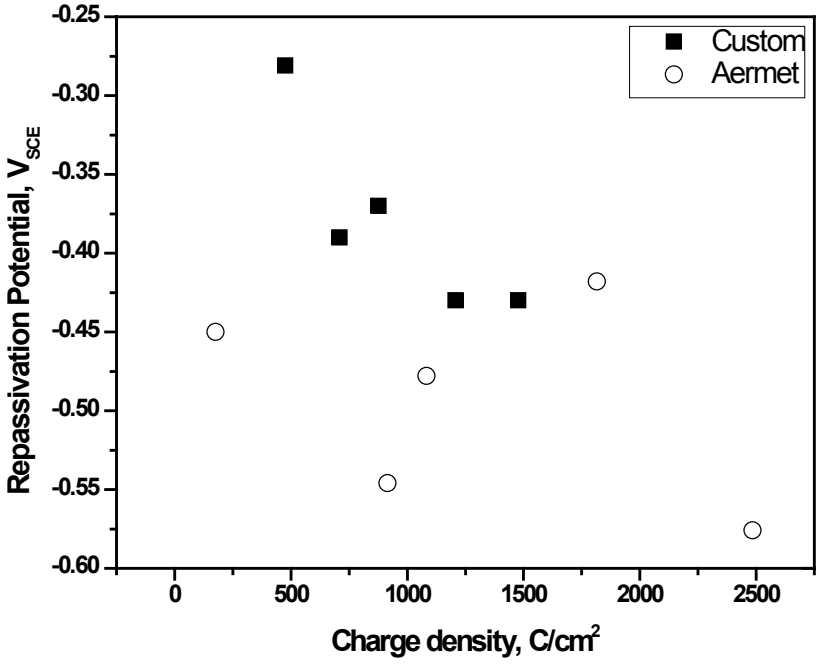

Figure 5.10 The change in repassivation potential with increase in charge density for Custom 465 and Aermet 100 in 0.6 M sodium chloride.

5.3 Cathodic polarization scans

Cathodic polarization scans were performed for the four alloys in sodium chloride and ferric chloride solutions, with concentrations pertaining to the relative humidity of the laboratory exposures. The results from all of these electrochemical scans will be presented.

During the 24-hour open-circuit potential monitoring of 304L in 1.5 and 2.6 M sodium chloride solutions, the potential of the alloy gradually increased in both experiments. The potential of the alloy was higher in the 1.5 M than in the 2.6 M sodium chloride solution (Figure 5.11). The corrosion potential, E_{corr}, values were -27.6 mV_{SCE} and -69.7 mV_{SCE} for 304L in 1.5 and 2.6 M sodium chloride solutions, respectively (Figure 5.12).

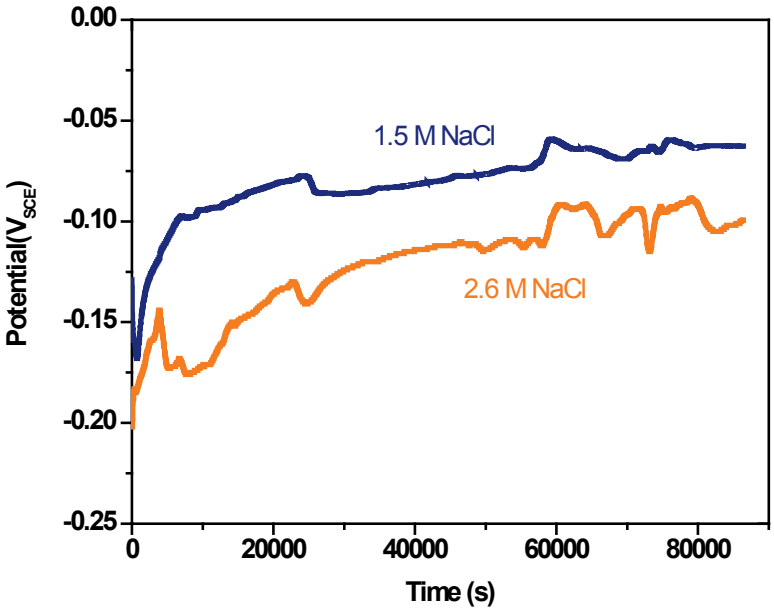

Figure 5.11 The open-circuit potential of 304L increased over the course of twenty-four hours in 1.5 and 2.6 M sodium chloride solutions.

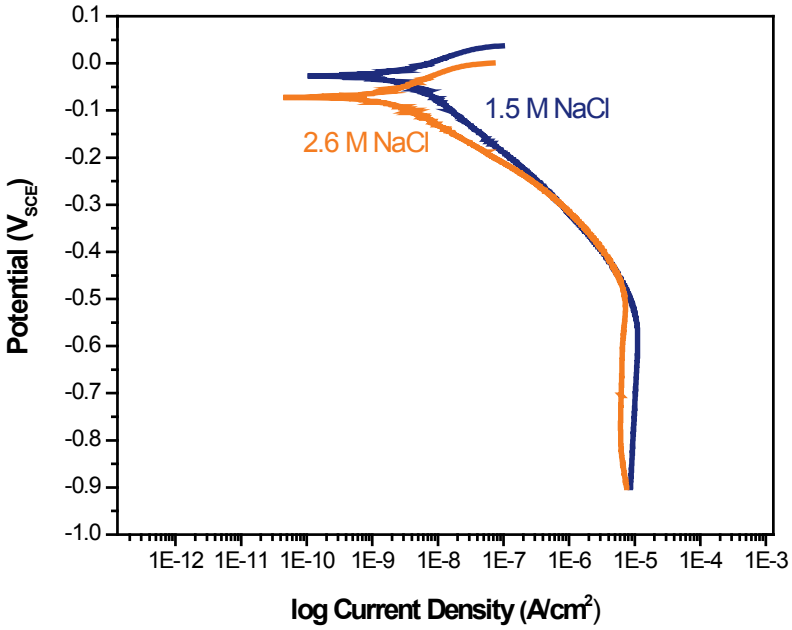

Figure 5.12 The cathodic polarization scans from +100 mV_{SCE} to -900 mV_{SCE} at 0.5 mV/s for 304L in 1.5 and 2.6 M sodium chloride solutions and with corrosion potentials of -27.6 mV_{SCE} and -69.7 mV_{SCE}, respectively.

The open-circuit potentials of 316L and Custom 465 followed a similar trend to 304L during the 24-hour open-circuit potential monitoring, starting out low and gradually rising over the course of the 24 hours (Figures 5.13 and 5.14). The E_{corr} values for 316L were -63.4 mV_{SCE} and -118 mV_{SCE} in 1.5 and 2.6 M sodium chloride solutions, respectively, while the E_{corr} values were the lowest of the stainless steels for Custom 465, at -153 mV_{SCE} and -123 mV_{SCE} in 1.5 and 2.6 M sodium chloride solutions (Figures 5.15 and 5.16).

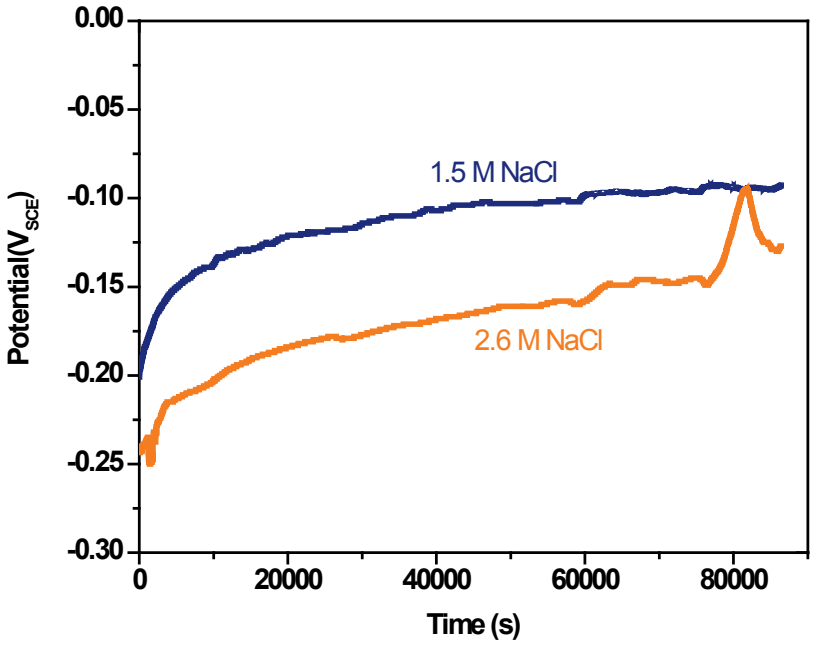

Figure 5.13 The open-circuit potential of 316L increased over the course of twenty-four hours in 1.5 and 2.6 M sodium chloride solutions.

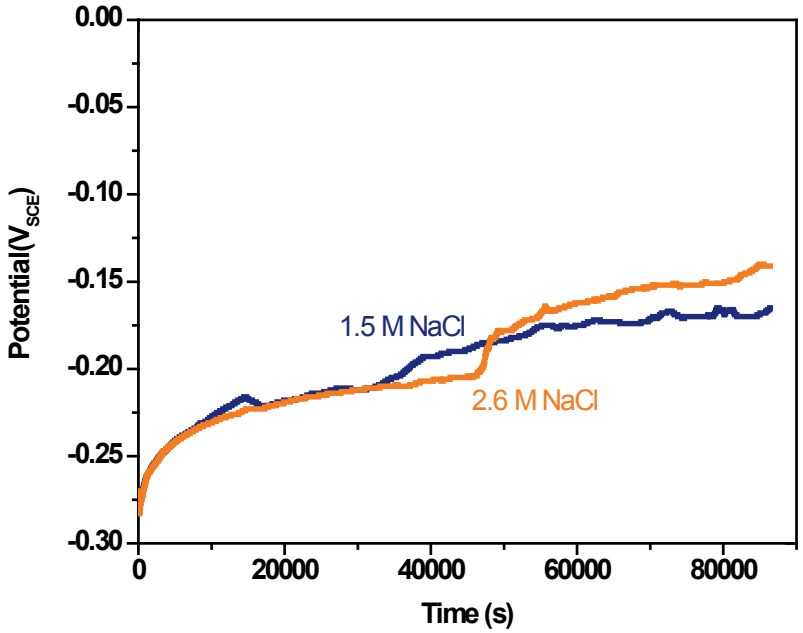

Figure 5.14 The open-circuit potential of Custom 465 increased over the course of twenty-four hours in 1.5 and 2.6 M sodium chloride solutions.

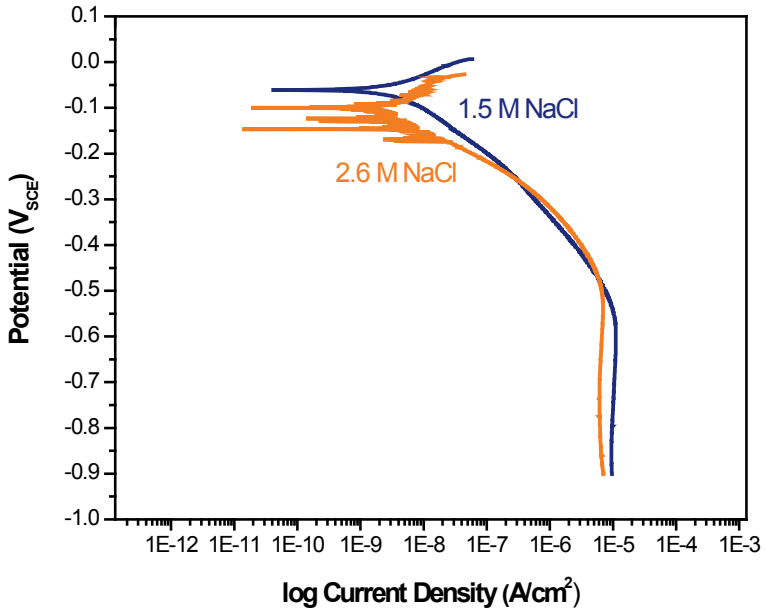

Figure 5.15 The cathodic polarization scans from +100 mV_{SCE} to -900 mV_{SCE} at 0.5 mV/s for 316L in 1.5 and 2.6 M sodium chloride solutions and with corrosion potentials of -63.4 mV_{SCE} and -118 mV_{SCE}, respectively.

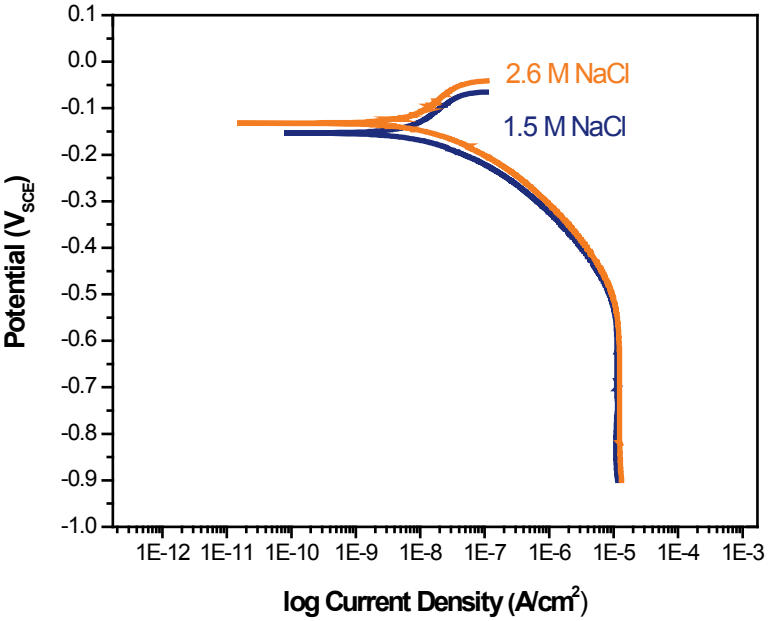

Figure 5.16 The cathodic polarization scans from +100 mV_{SCE} to -900 mV_{SCE} at 0.5 mV/s for 316L in 1.5 and 2.6 M sodium chloride solutions and with corrosion potentials of -153 mV_{SCE} and -123 mV_{SCE}, respectively.

In contrast to the open-circuit potential of the stainless steels, the open-circuit potential of Aermet decreased immediately when the sample was placed in the 1.5 and 2.6 M sodium chloride solutions. Therefore, the open-circuit potential monitoring was limited to 30 minutes for Aermet to prevent the loss of any cathodic potential (Figure 5.17). The Aermet alloy had lower E_{corr} values at approximately -505 mV_{SCE} and 522 mV_{SCE} in 1.5 and 2.6 M sodium chloride solutions (Figure 5.18).

All of the alloys had the same diffusion limiting current density of 1E-5 A/cm^2. The polarization curves of the stainless steel alloys had an activation-controlled region, with which both the E_{corr} values and the repassivation potential were contained. An activation-controlled region was not observed in the polarization curve of Aermet. Its potential immediately dropped into a diffusion-controlled regime after falling below the E_{corr} value of Aermet.

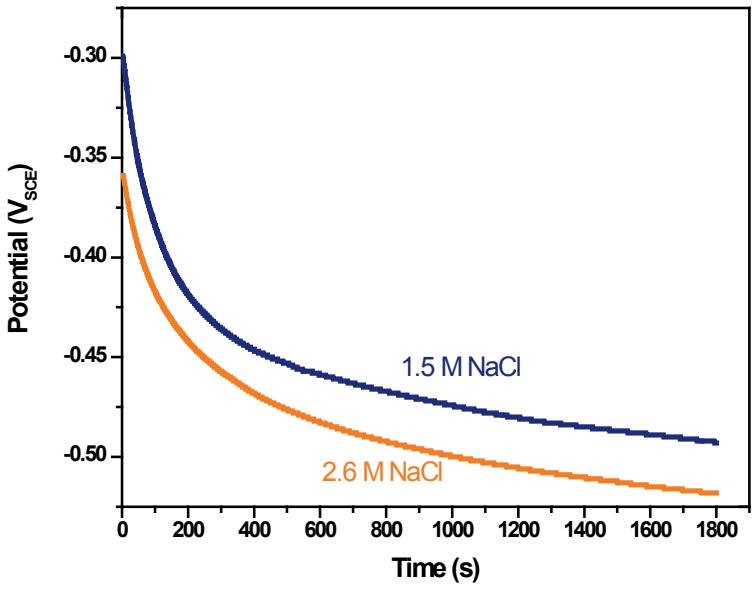

Figure 5.17 The open-circuit potential of Aermet 100 decreased over the course of thirty minutes in 1.5 and 2.6 M sodium chloride solutions.

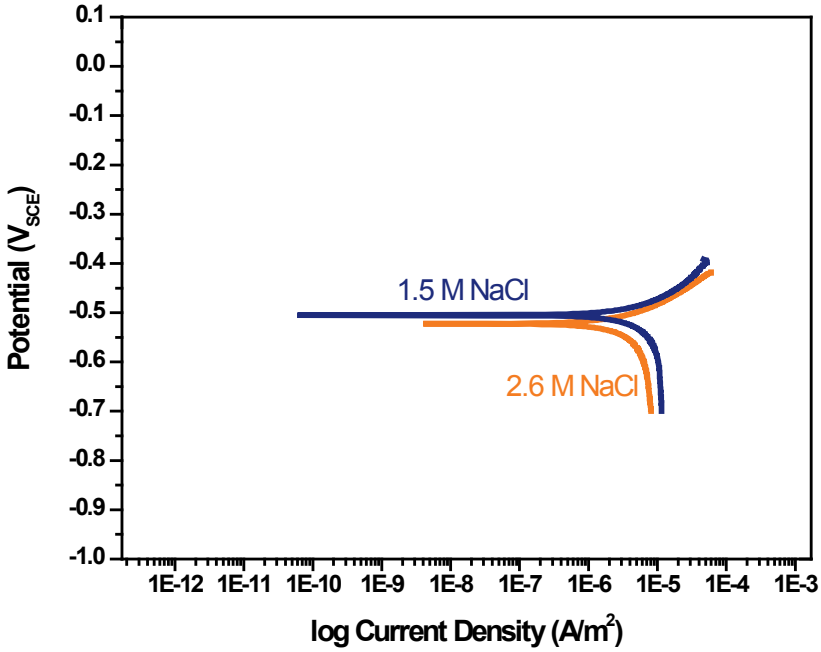

Figure 5.18 The cathodic polarization scans from +100 mV_{SCE} to -900 mV_{SCE} at 0.5 mV/s for 316L in 1.5 and 2.6 M sodium chloride solutions and with corrosion potentials -505 mV_{SCE} and 522 mV_{SCE}, respectively.

Cathodic polarization curves also were obtained for 304L, 316L, and Custom 465 in 0.3 M ferric chloride. 316L had the highest E_{corr} value of -38 mV_{SCE}, followed by an E_{corr} value of -65.3 mV_{SCE} for Custom, and -122 mV_{SCE} for 304L (Figure 5.19).

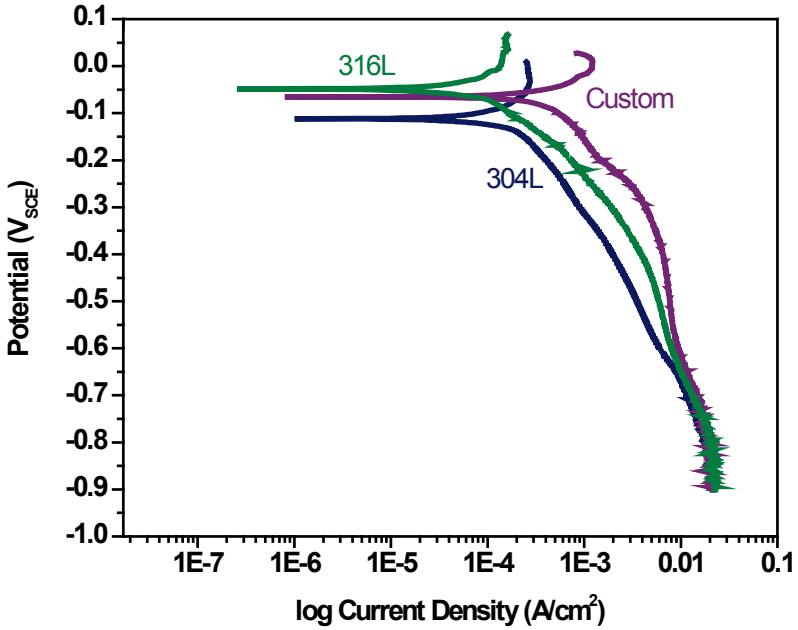

Figure 5.19 Cathodic polarization scans from +100 mV_{SCE} to -900 mV_{SCE} at 0.5 mV/s for 316L, Custom 465, and 304L in a 0.3 M ferric chloride solution and with corrosion potentials -38 mV_{SCE}, -65.3 mV_{SCE}, and -122 mV_{SCE}, respectively.

Cathodic polarization curves also were obtained for 304L in 0.3 M, 1.4, 2.8 M ferric chloride solutions, corresponding to the RH values of 98, 85 and 64% used in the thin film experiments. All of the polarization curves obtained for ferric chloride show limited activation-controlled regions (Figure 5.20). Specifically for the high concentrations of ferric chloride, the potential dropped immediately into the diffusion-controlled regime after dropping below the E_{corr} value.

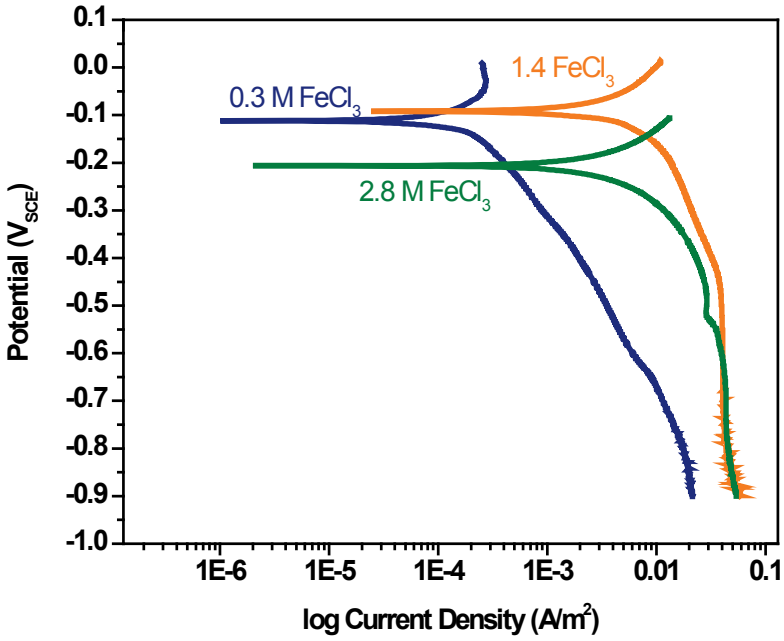

Figure 5.20 Cathodic polarization scans from +100 mV_{SCE} to -900 mV_{SCE} at 0.5 mV/s for 304L in 0.3, 1.4, and 2.8 M ferric chloride solution indicate limited activation-controlled regions.

5.4 Predicted model values

The predicted maximum pit radius for each alloy under certain environmental conditions and pertaining to specific experiments will be presented here. Model values for the sodium chloride exposures will be discussed along with values for both the drop and thin film exposures with deposited ferric chloride.

Figure 5.21 shows the predicted model values for the four alloys with deposited sodium chloride of two loading densities 240 μg/cm^2 and 600 μg/cm^2 exposed to two RH values, 90 and 95%. For the most severe environment of 600 μg/cm^2 of sodium chloride and a RH of 95%, 304L had the highest predicted pit radius of approximately 131 μm. The highest predicted pit radius for Custom was 109 μm, while Aermet had a maximum pit radius of 89 μm. The 316L alloy had the lowest predicted pit radius, for this specific

environmental condition, of 46 μm. The results also indicate for all alloys that the maximum predicted pit radius increased with increasing loading density as well as with increasing relative humidity. For a constant relative humidity value, increasing the loading density increased the maximum pit radius by the largest amount.

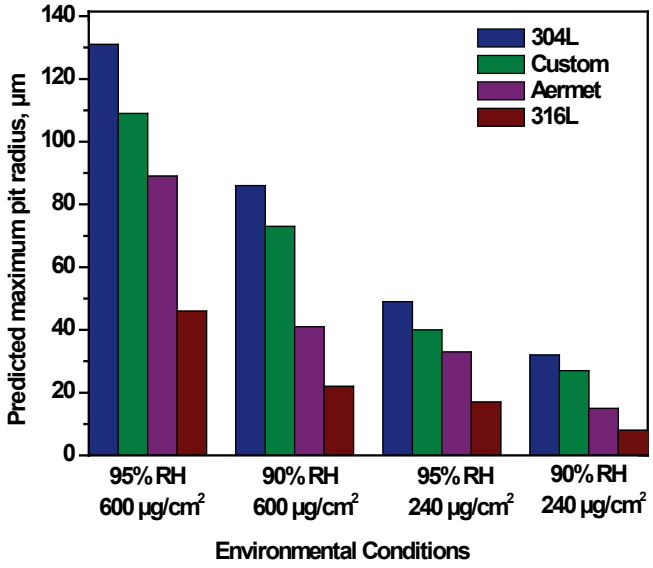

Figure 5.21 Predicted maximum pit radii for 304L, Custom, Aermet, and 316L with loading densities of 240 or 600 μg/cm^2 sodium chloride and 90 or 95% RH.

The E_{rp} of an alloy is an intrinsic property that has a strong effect on the size of the pits that will form under atmospheric exposure conditions. Predicted values for the computational model 304L, 316L, and Custom 465 (Figure 5.22-5.24) show that alloys with lower repassivation potentials have cathodes that can supply more current, thus enabling larger stable pits. Figure 5.25 shows the maximum cathode current available as a function of repassivation potential. The data points in Figure 5.25 correspond to maximum pit radius values. 304L has a lower repassivation potential -400 mV_{SCE}[36] than 316L -250 mV_{SCE}[37], and thus, 304L can provide higher cathodic currents. With more current available, 304L samples exposed to different environmental conditions develop

larger pits than 316L samples exposed to the same conditions. Newman et al., found the difference in repassivation potential between 316L and 304L to be the result of molybdenum, which is only present in the 316L alloy.[38] Using a scratch technique, this study confirmed that molybedum has an inhibiting effect on active dissolution of the alloy and therefore, to maintain a critical chemistry in a pit, a higher potential is required.

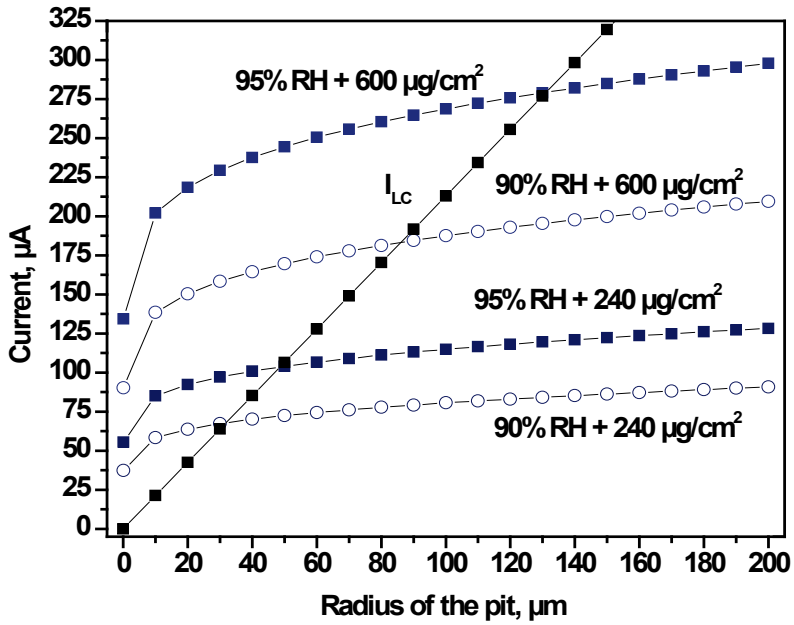

Figure 5.22 $I_{cath,max}$ and I_{LCmin} plotted as a function of pit radius for 304L in four environmental conditions with deposited sodium chloride.

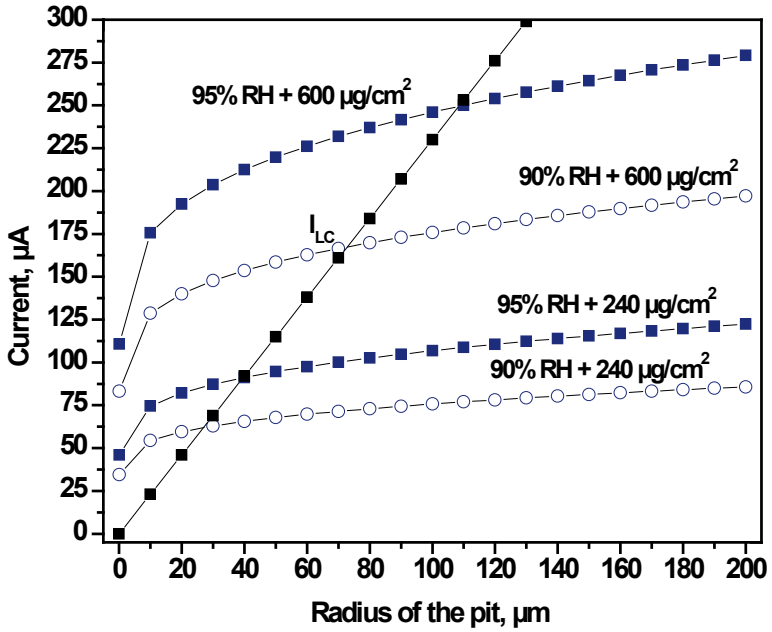

Figure 5.23 $I_{cath,max}$ and I_{Lcmin} plotted as a function of pit radius for Custom 465 in four environmental conditions with deposited sodium chloride.

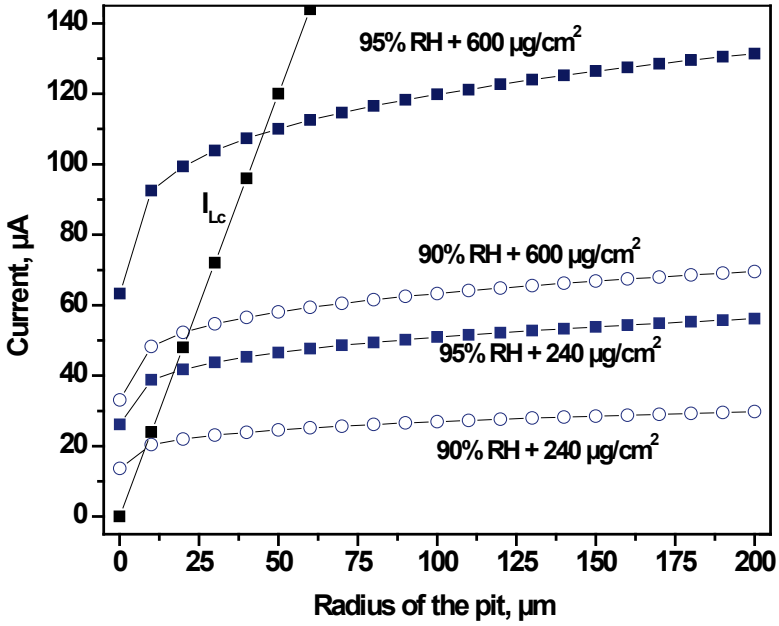

Figure 5.24 $I_{cath,max}$ and I_{Lcmin} plotted as a function of pit radius for 316L in four environmental conditions with deposited sodium chloride.

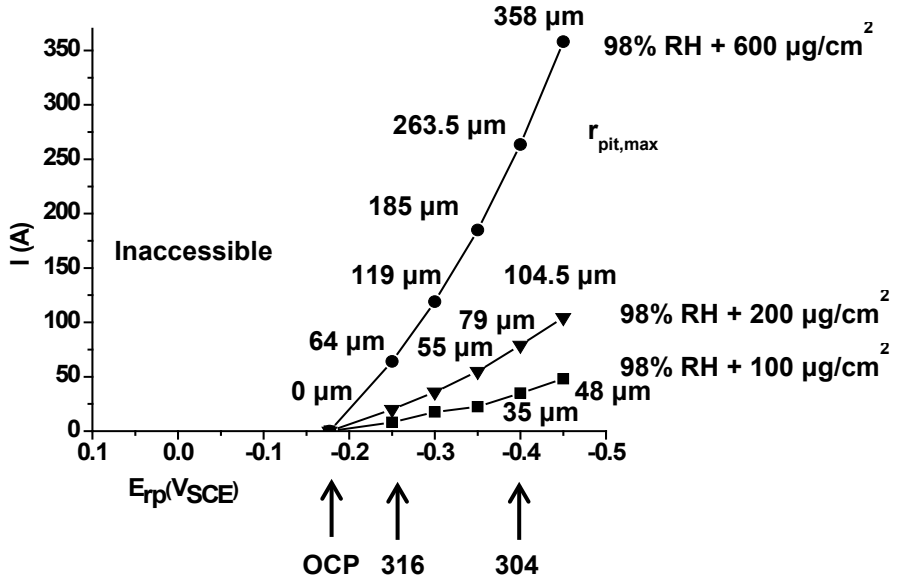

Figure 5.25 Pit radii plotted as a function of repassivation potential and current for three environmental conditions. Alloys with lower repassivation potentials have higher currents available and thus larger pit radii are observed.

Figures 5.26-5.28 present the results for the maximum predicted pit radius that could form on the stainless steel alloys with deposited ferric chloride. These figures were created to correlate with the laboratory drop exposures.

For the first drop experiment, Custom 465, 316L, and 304L were exposed at 98% RH with 100 µg/cm^2 of deposited ferric chloride. Figure 5.26 shows that Custom 465 had the highest predicted pit radius, 130 µm, followed by 304L with a pit radius of 75 µm and 316L with a pit radius of 47 µm.

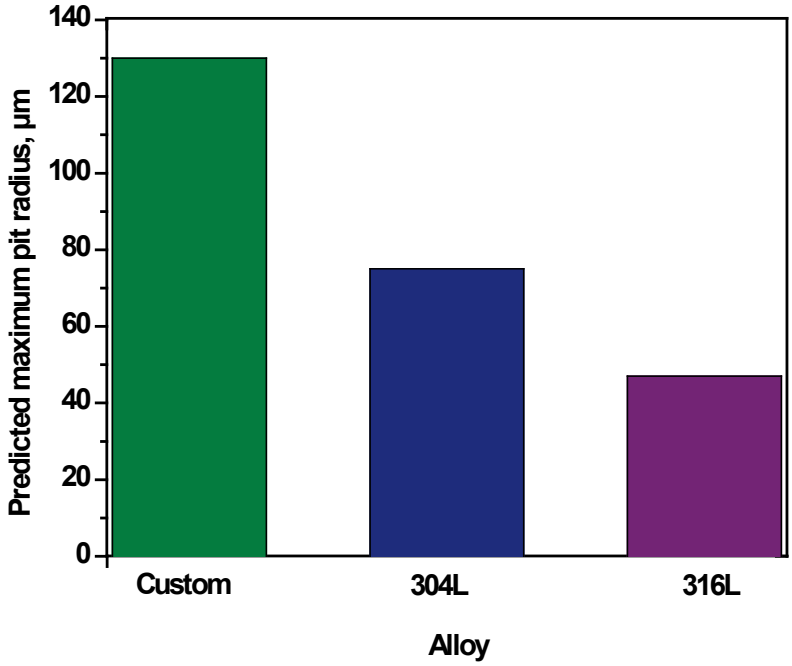

Figure 5.26 Predicted maximum pit radii for Custom, 304L, and 316L, with an environmental condition of 98% RH and 100 µg/cm^2 deposited ferric chloride.

The effect of loading density and RH on the 304L alloy with deposited ferric chloride was studied in separate drop experiments. Figure 5.27 shows that with increasing loading density the size of the pit radius increased significantly. For a loading density of 400 µg/cm^2 of ferric chloride, the predicted pit radius was 375 µm. The size of the pit radius decreased to 196 µm for a loading density of 250 µg/cm^2 and even further to 75 µm for a loading density of 100 µg/cm^2 of ferric chloride. With a decreased loading density of 40 µg/cm^2 ferric chloride and a relative humidity of 64%, the maximum pit radius decreased for 304L to 13 µm (Figure 5.28).

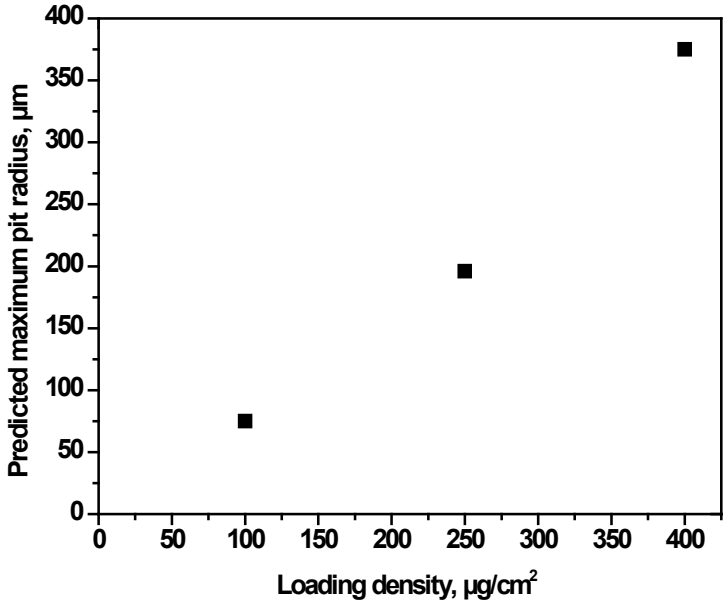

Figure 5.27 The increase in predicted maximum pit radius with increasing loading density for a 304L sample exposed to 98% RH and with three loading densities of ferric chloride, 100, 250, and 400 µg/cm^2.

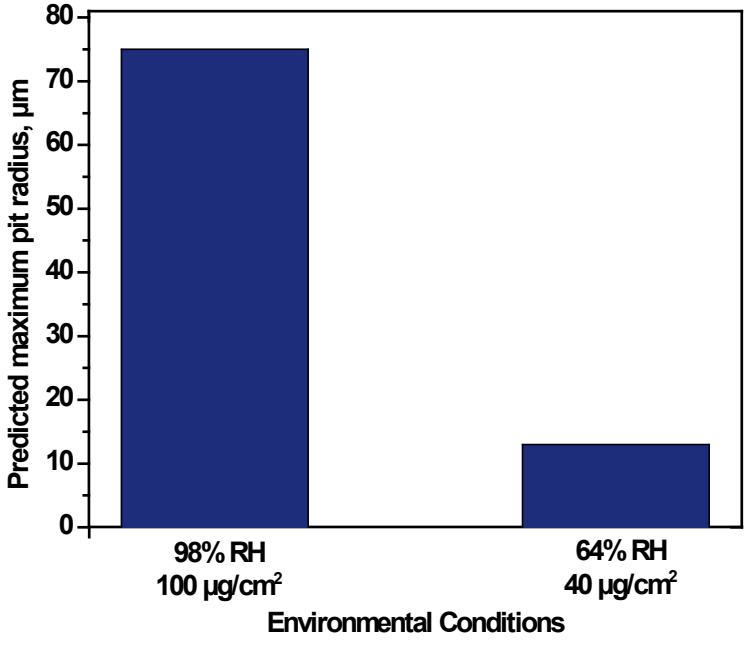

Figure 5.28 Comparison of predicted maximum pit radius for 304L in two environmental conditions with deposited ferric chloride, 98% RH and 100 µg/cm^2 and 64% RH and 40 µg/cm^2.

The maximum predicted pit radius for 304L is plotted in Figures 5.29 – 5.30 with three loading densities, 100, 250, and 400 μg/cm^2 of ferric chloride and with the three relative humidity values of 98, 85, and 64% used in the thin film experiments. The effect of relative humidity on the maximum pit radius is shown in Figure 5.29 for the three loading densities, while the effect of loading density at a constant relative humidity is shown in Figure 5.30. With either an increase of the loading density or an increase of the relative humidity the maximum pit radius also increased. The larger increase in pit size was observed by increasing the loading density while keeping the relative humidity value constant.

The trend of increased pit size with an increase of loading density or relative humidity, however, did not apply to the lowest relative humidity value of 64% and the highest loading density 400 μg/cm^2. This environmental condition had the largest maximum pit radius of the three relative humidity values. Examining the inputs into the model helped determine that the increase of the value of the integration in the computational model along with an increase in water layer thickness produced larger cathodic currents and thus a larger maximum pit radius for this environmental condition. For the lower loading densities, although the value of the integral was large, the water layer thickness was small, leading to smaller predicted pit radii. This variation in pit size due to a change in the integration value or the water layer thickness shows the importance of the input parameters to the predicted model values. The sensitivity of these parameters will be discussed further in later sections.

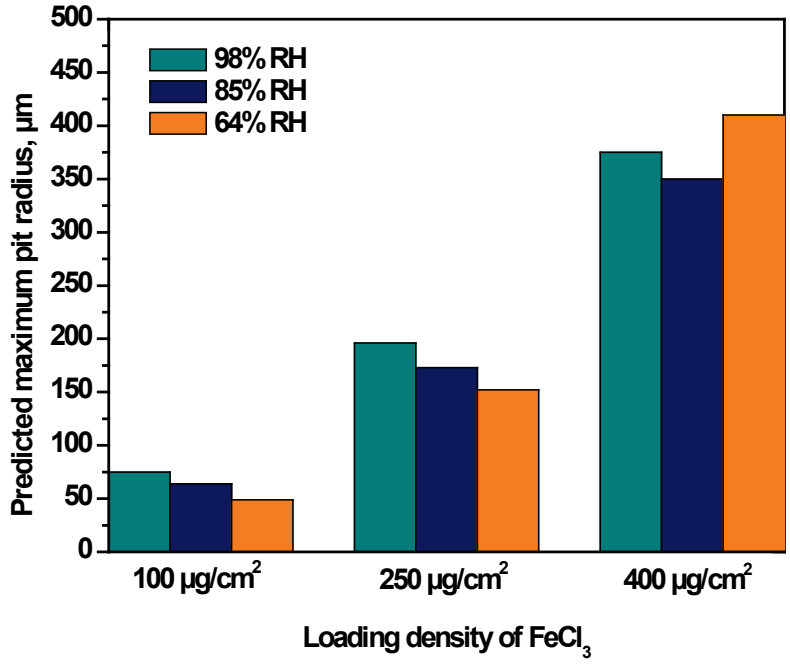

Figure 5.29 The effect of RH with constant loading densities of 100, 250, and 400 µg/cm^2 ferric chloride on the maximum predicted pit radius for 304L.

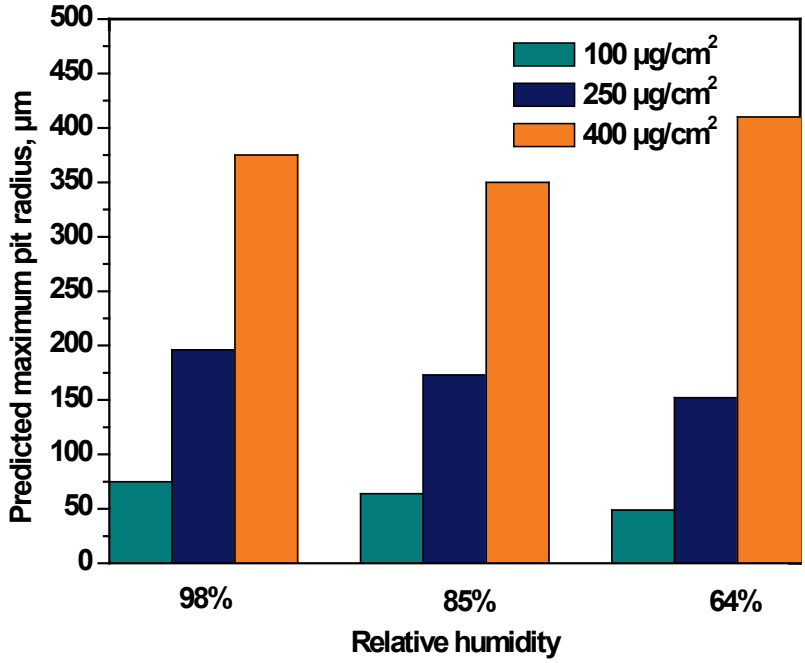

Figure 5.30 The effect of loading density with constant RH values of 98, 85, and 64% on the maximum predicted pit radius for 304L.

5.5 Analysis of sodium chloride laboratory exposures

As mentioned in Section 5.4, the three stainless steels, 304L, 316L, and Custom 465 and the high-strength steel, Aermet, with deposited sodium chloride and loading densities of 240 μg/cm^2 and 600 μg/cm^2 were exposed in controlled relative humidity containers at 90 and 95% RH. Samples were removed from the containers at 1 month, 3 months, 6 months, and 1 year intervals. The maximum pit sizes found on these exposures will be discussed in Section 5.5.1 and 5.5.2.

5.5.1 304L, 316L, and Custom exposures

The 1-year 304L and 316L samples were analyzed using a FIB to cross-section and image pits found on the surface of these alloys. No undercutting was observed, and pits were found to have radii < 2 μm (Figure 5.31). Similarly for Custom 465, pits with radii < 2 μm were found on all of the exposed samples. Possible explanations for the small pit sizes observed will be examined in Section 6.2.

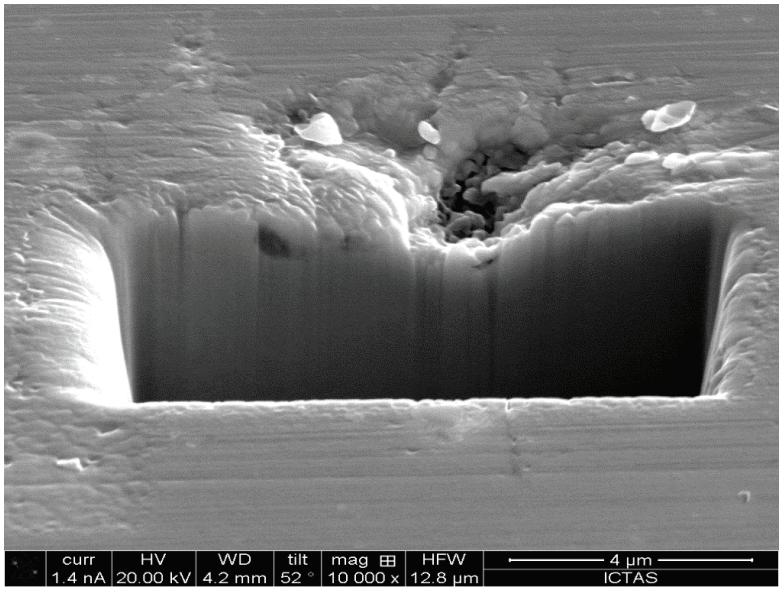

Figure 5.31 A cross-sectional image of a 316L sample exposed for 3 months to 95% RH and 600 μg/cm^2 sodium chloride in which no tunneling was observed.

5.5.2 Aermet exposures

Although the pits observed on the stainless steels were small, distinct areas of localized corrosion or pitting were found on the surface of these samples. However on the Aermet samples, localized corrosion as well as general corrosion occurred on the surface of all of the exposed samples. Areas of uniform corrosion were found surrounding and bordering large pits on the Aermet alloy. The 1-month samples of Aermet of both loading densities, 240 $\mu g/cm^2$ and 600 $\mu g/cm^2$, had areas of uniform corrosion as well as pits. Over the course of the 1-year exposure, localized corrosion on the samples with the higher loading density of 600 $\mu g/cm^2$ mostly ceased and general corrosion was more prevalent (Figure 5.32). However, Figure 5.33 shows that for a 1-year exposure sample with a loading density of 240 $\mu g/cm^2$ deep pits still were observed, along with some general corrosion. This trend is reflected in the average pit depths plotted versus exposure time in Figure 5.34. Although in the beginning of the exposure similar pit depths were observed for both loading densities and relative humidity values, over the course of the exposure time the maximum pit depth increased for the lower loading density and decreased for the higher loading density as it was consumed by general corrosion.

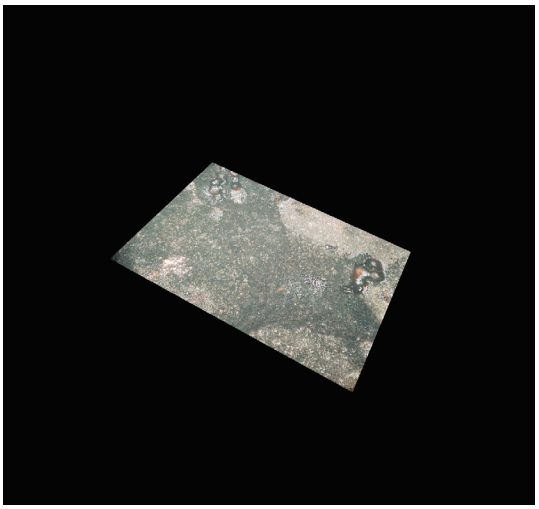

Figure 5.32 Severe general corrosion over the entire surface of a 1 year Aermet exposure, exposed to 95% RH and with 600 μg/cm^2 sodium chloride.

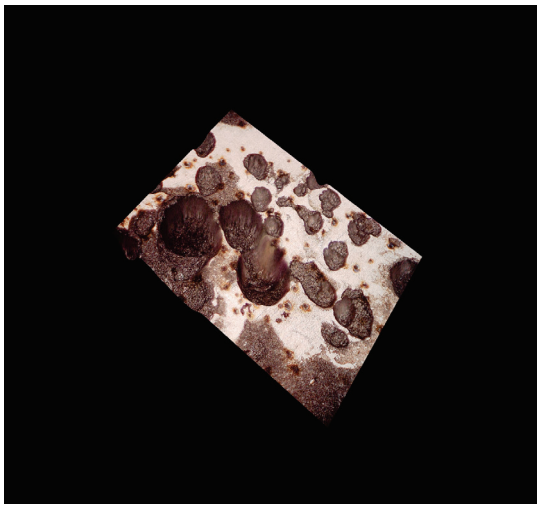

Figure 5.33 Localized corrosion along with some general corrosion on a 1 year Aermet exposure, exposed to 95% RH and with 240 μg/cm^2 sodium chloride.

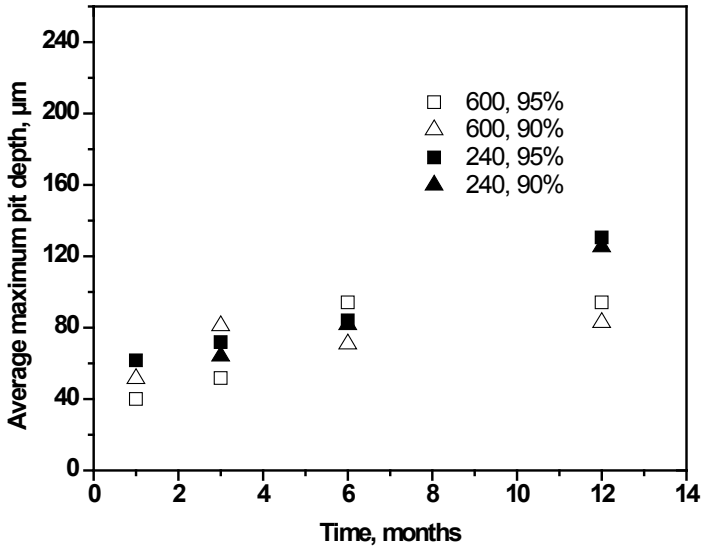

Figure 5.34 The average maximum pit depth plotted versus time for Aermet samples exposed to four environmental conditions with deposited sodium chloride indicates that with increasing time the lower loading density had higher pit depths.

To show the distribution of pit depths as well as the probability of obtaining a certain pit depth, data corresponding to twelve pit depths, four across the top, middle, and bottom were measured each from areas of 0.59 mm^2 on the Aermet exposures, was fit

using probability distributions. To calculate the proper distribution for the data two environmental conditions were examined using Minitab 16's Individual Distribution Identification. The lognormal distribution was determined to be the best fit for the data, with high P-values of 0.399 and 0.226 indicating a good fit for the two conditions (Figures 5.35 and 5.36)

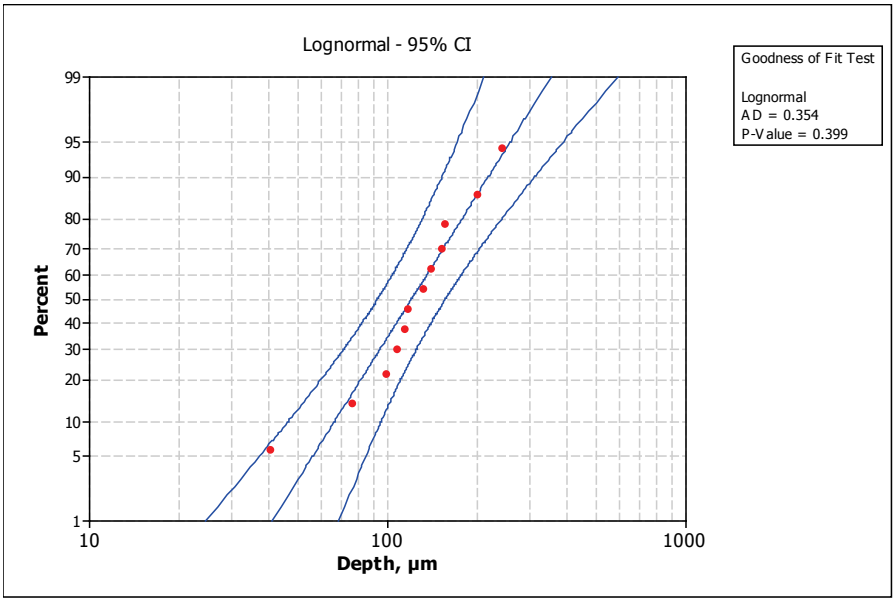

Figure 5.35 The Individual Distribution Identification indicates that the lognormal distribution has a high correlation with a P-value of 0.399 with the pit depth data for 1 year Aermet exposures, exposed to 95% RH and with 240 µg/cm^2 sodium chloride.

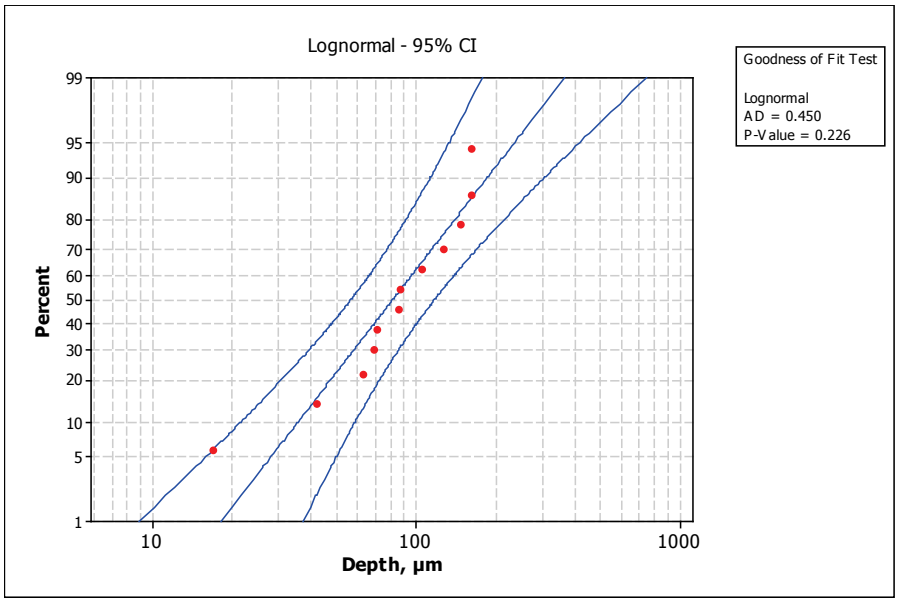

Figure 5.36 The Individual Distribution Identification indicates that the lognormal distribution has a high correlation with a P-value of 0.266 with the pit depth data for 1 year Aermet exposures, exposed to 95% RH and with 600 µg/cm^2 sodium chloride.

Figures 5.37 – 5.40 show the maximum pit depths observed on the Aermet samples exposed to four environmental conditions. For all of the Aermet exposures with deposited sodium chloride, maximum pit depth values increased with time. As mentioned earlier, the lowest loading density of 240 µg/cm^2 had the highest maximum pit depths.

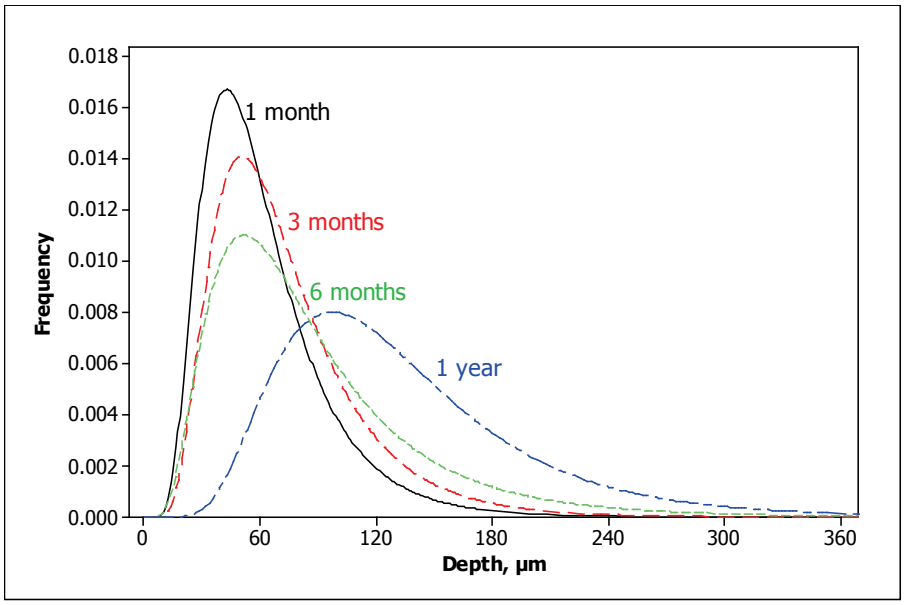

Figure 5.37 The lognormal distribution for pit depth data fit for Aermet exposures, exposed to 95% RH and with 240 µg/cm^2 sodium chloride indicates pit depth increased with exposure period.

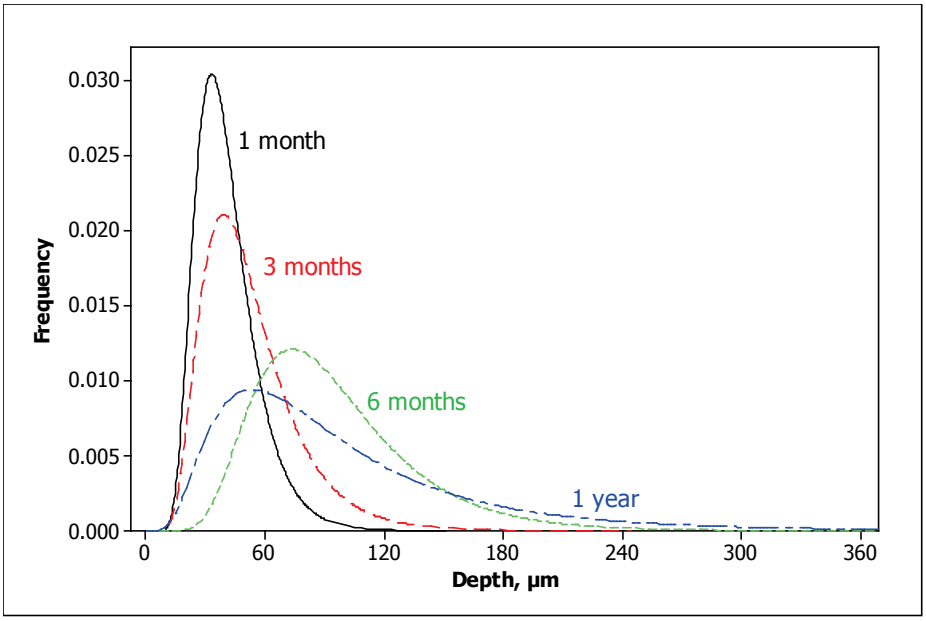

Figure 5.38 The lognormal distribution for pit depth data fit for Aermet exposures, exposed to 95% RH and with 600 µg/cm^2 sodium chloride indicates pit depth increased with exposure period.

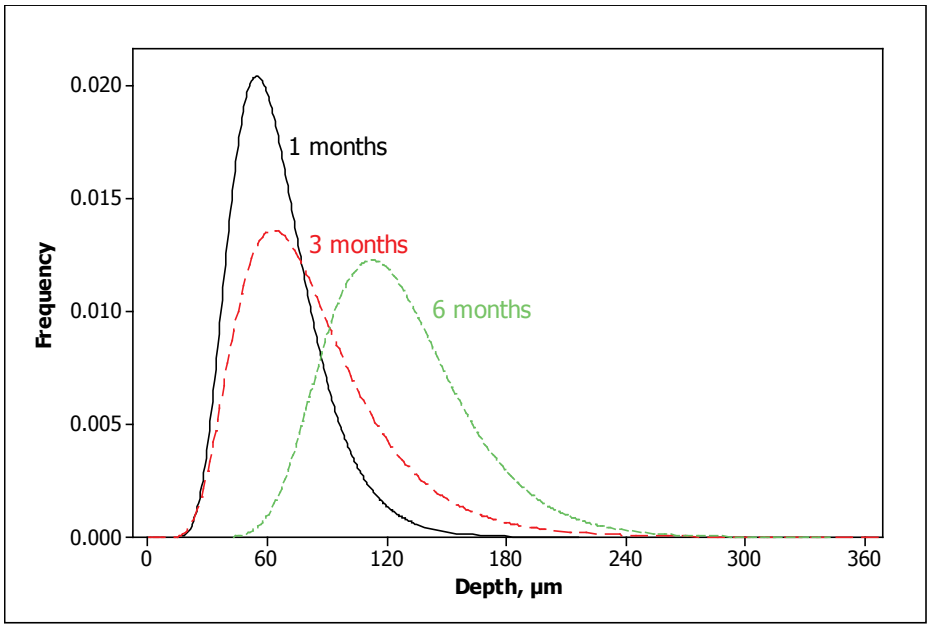

Figure 5.39 The lognormal distribution for pit depth data fit for Aermet exposures, exposed to 90% RH and with 240 µg/cm^2 sodium chloride indicates pit depth increased with exposure period.

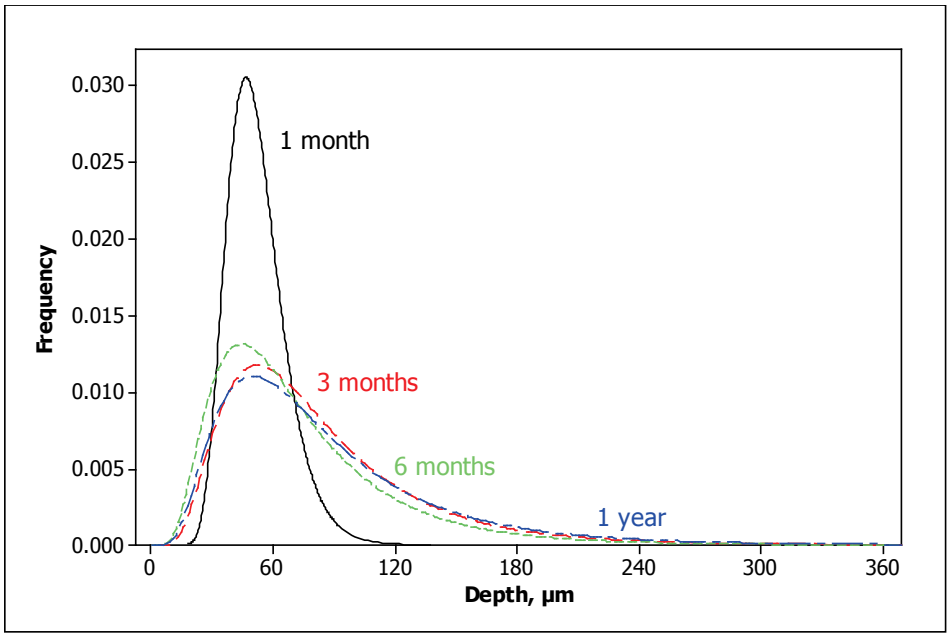

Figure 5.40 The lognormal distribution for pit depth data fit for Aermet exposures, exposed to 90% RH and with 600 µg/cm^2 sodium chloride indicates pit depth increase with exposure period.

5.6 Ferric chloride exposures

The ferric chloride exposures were performed in order to enhance the pitting process and obtain larger pits that could be analyzed using the Hirox Digital Microscope. Two different methods of depositing ferric chloride were employed, as drops using the piezoelectric printer and as a thin film using a procedure detailed in Section 4.5.3. Pit depths were obtained from 0.16 mm^2 areas under the drops and from 0.59 mm^2 areas under the thin film. All three stainless steels 304L, 316L, and Custom were examined for the drop experiments, while only 304L was studied for the thin film experiments. Results from all of the laboratory exposures will be discussed in Sections 5.6.1 – 5.6.4.

5.6.1 Drop experiments

Four loading densities, 40, 100, 250, and 400 $\mu g/cm^2$ of ferric chloride were deposited as drops on samples for the initial ferric chloride exposures. Figure 5.40 shows the discrete drops that were formed for the lower loading density of 40 $\mu g/cm^2$. However, for the higher loading density of 400 $\mu g/cm^2$, coalescence of the drops occurred immediately after deposition before the exposure began at 98% RH (Figure 5.41). Figures 5.42 and 5.43 show the same samples after an exposure time of 168 hours. Although the drops remained discrete for the loading density of 40 $\mu g/cm^2$ (Figure 5.42), the thin film continued to spread to form a larger film across the printed area for the higher loading density (Figure 5.43). These images show for the drop experiment that both drops and thin films existed depending on the loading density of ferric chloride on the sample. This knowledge is useful when comparing maximum pit depths found under drops compared to those found under thin films.

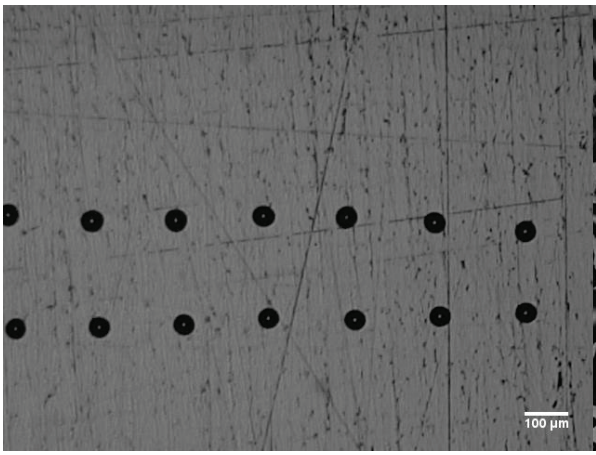

Figure 5.41 Discrete drops with loading density 40 µg/cm^2 ferric chloride on 304L before exposure.

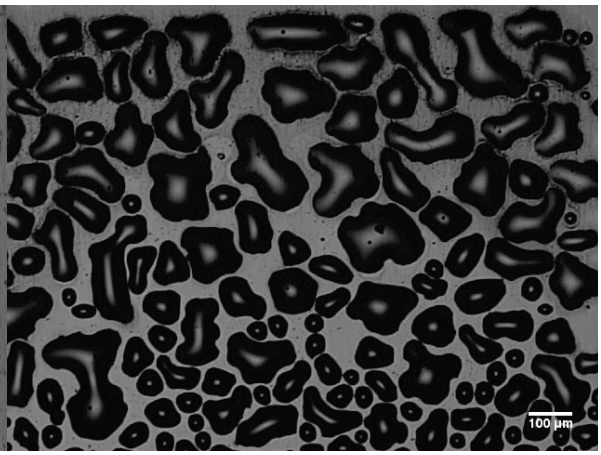

Figure 5.42 Coalescence of drops with loading density 400 µg/cm^2 ferric chloride on 304L before exposure.

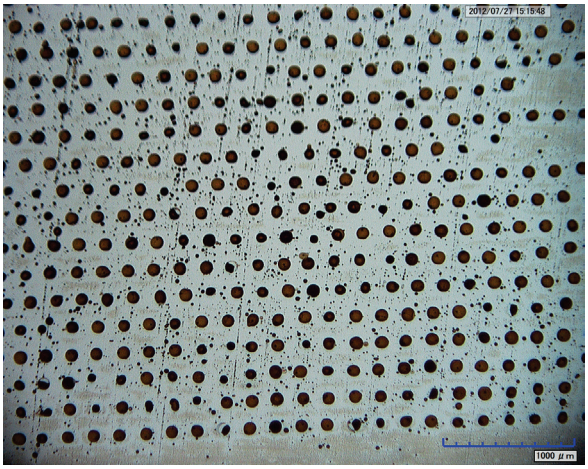

Figure 5.43 Discrete drops with loading density 40 µg/cm^2 ferric chloride on 304L after exposure to 98% RH for 168 hours.

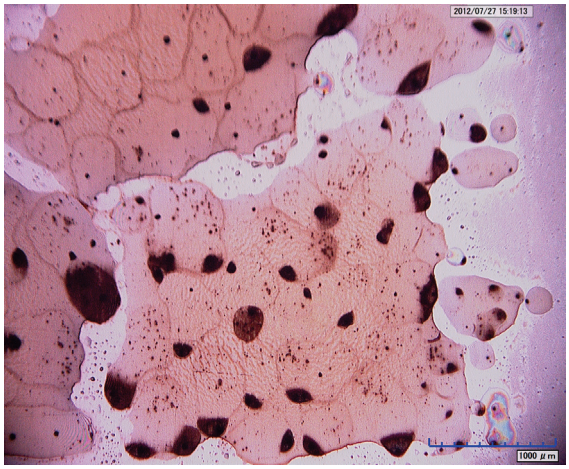

Figure 5.44 Further spreading of drops with loading density 400 µg/cm^2 ferric chloride on 304L after exposure to 98% RH for 168 hours.

Similarly to the Aermet data, the maximum pit depths found on the ferric chloride drop exposures were fit to a lognormal distribution to show the distribution of pit depths. In comparison to the Aermet exposures, values of 0 µm were found on the samples. To fit the data, these values were omitted, and only positive values were used. Figure 5.45 shows a strong correlation for this distribution with the data, with a P-value of 0.259.

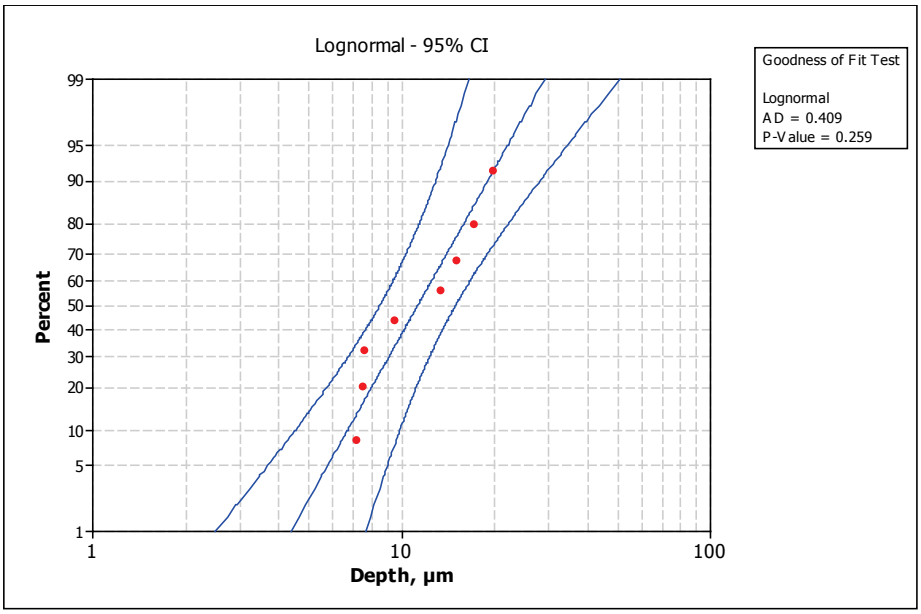

Figure 5.45 The Individual Distribution Identification indicates that the lognormal distribution has a high correlation with a P-value of 0.259 with the pit depth data for a 304L sample, exposed to 95% RH and with 400 µg/cm^2 ferric chloride for 336 hours.

For the same loading density of 100 µg/cm^2, Custom 465 had the largest maximum pit depths on its surface, followed by 304L, and 316L (Figure 5.46-5.48). No pit depths were found greater than 12 µm (Figure 5.49).

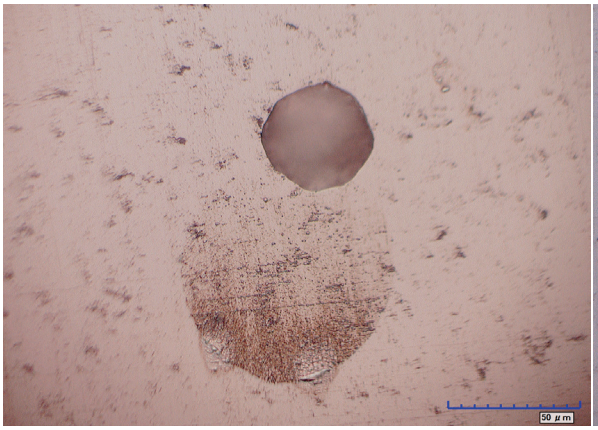

Figure 5.46 Pit with depth 12 µm on a Custom 465 sample with loading density 100 µg/cm^2 and exposed to 98% RH.

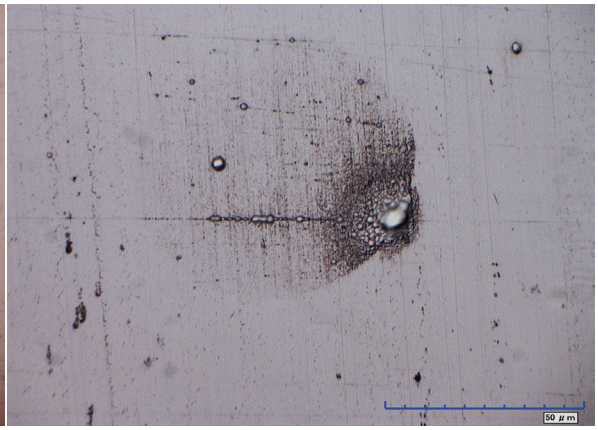

Figure 5.47 Pit with depth 5 µm on a 304L sample with loading density 100 µg/cm^2 and exposed to 98% RH.

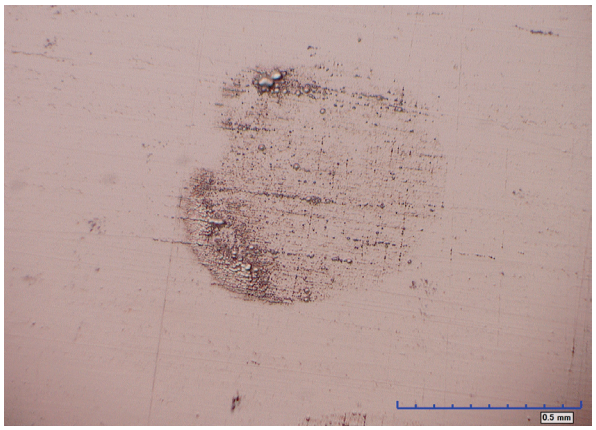

Figure 5.48 Pit with depth 4 μm on a 316L sample with loading density 100 μg/cm^2 and exposed to 98% RH

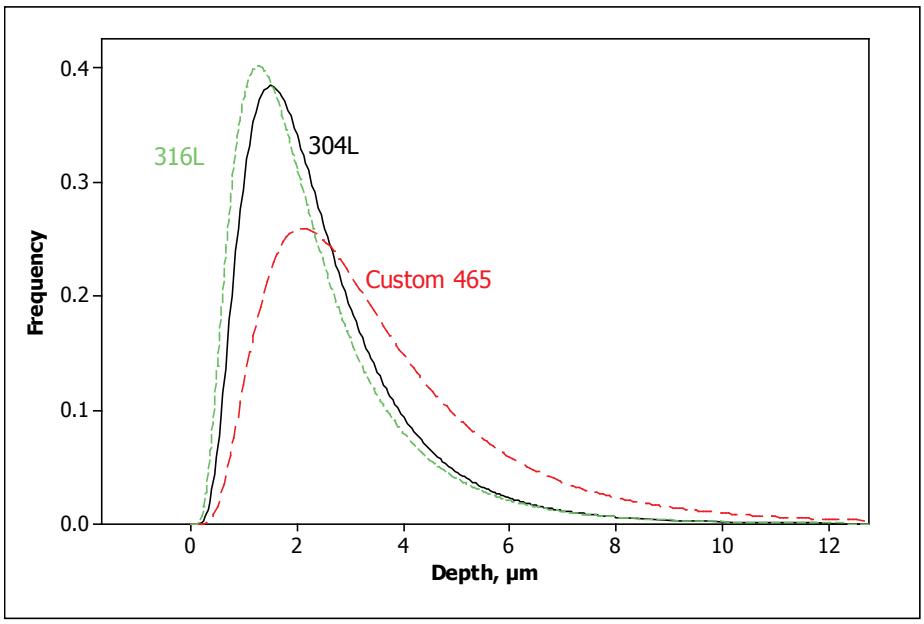

Figure 5.49 The lognormal distribution fit to pit depth data for 316L, 304L, and Custom exposed to 98% RH and with 100 μg/cm^2 ferric chloride indicates pit depths < 12 μm.

The values of the maximum pit depths found on 304L samples increased with increasing loading density as expected (Figures 5.50-5.52). All values of pit depth were bounded by 30 μm (Figure 5.53).

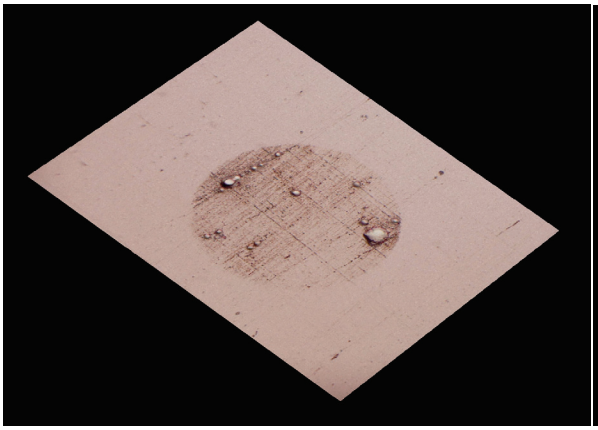

Figure 5.50 Pits with maximum depth 5 μm on a 304L sample with loading density 100 μg/cm^2 and exposed to 98% RH.

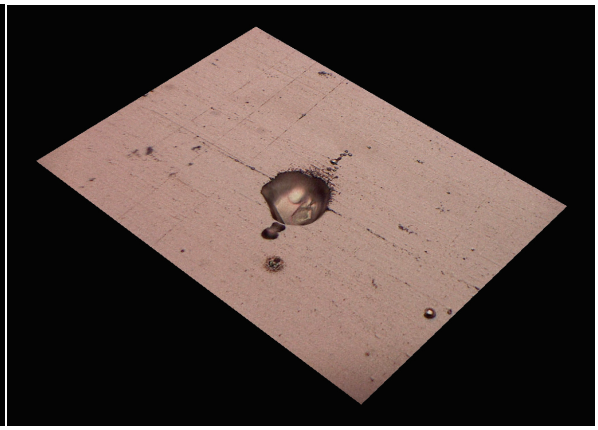

Figure 5.51 Pit with depth 12 μm on a 304L sample with loading density 250 μg/cm^2 and exposed to 98% RH.

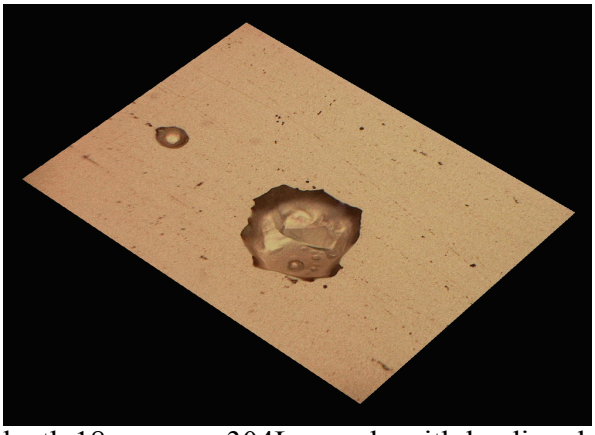

Figure 5.52 Pit with depth 18 μm on a 304L sample with loading density 100 μg/cm^2 and exposed to 98% RH

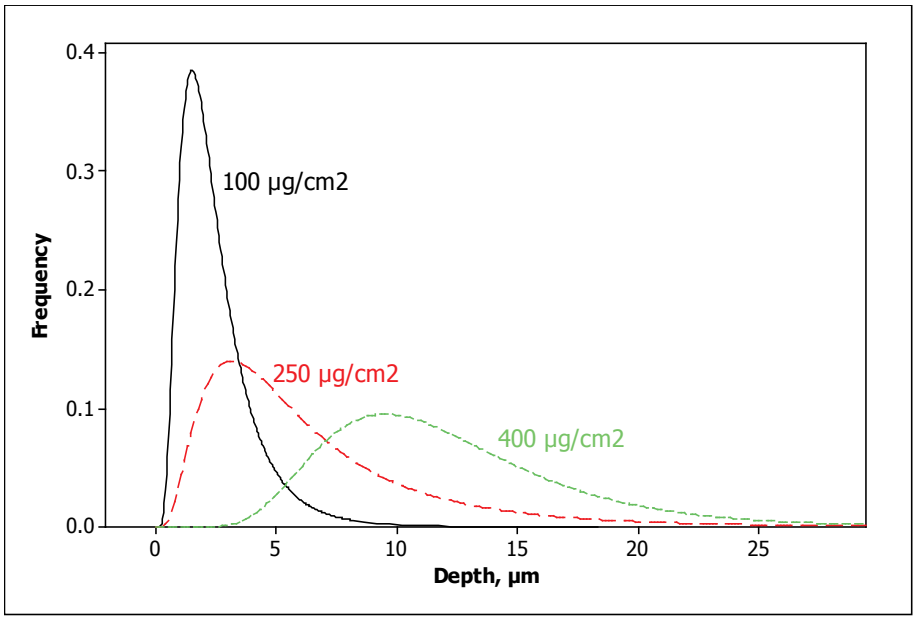

Figure 5.53 The lognormal distribution fit to pit depth data for 304L with loading densities of 100, 250, and 400 µg/cm^2 ferric chloride indicates pit depths increased with increasing loading density and pit depths < 30 µm

An unexpected result was the increase of pit depths found on a 304L sample with lower loading density, 40 µg/cm^2 and RH, 64% (Figure 5.54). This trend was examined further in the thin film experiments (Figure 5.55).

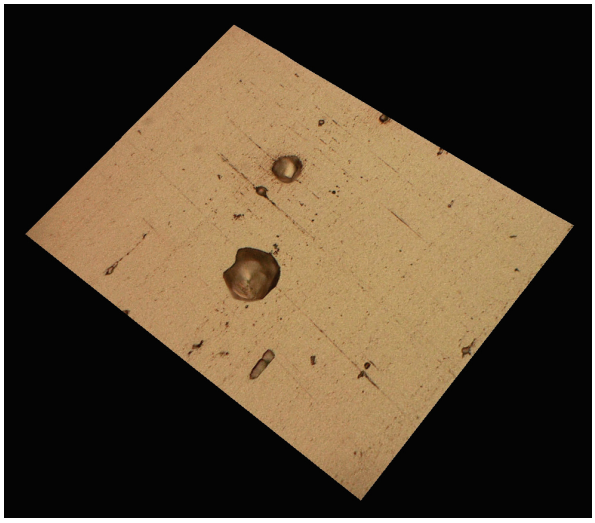

Figure 5.54 Pit with depth 7 µm on a 304L sample with loading density 40 µg/cm^2 and exposed to 64% RH

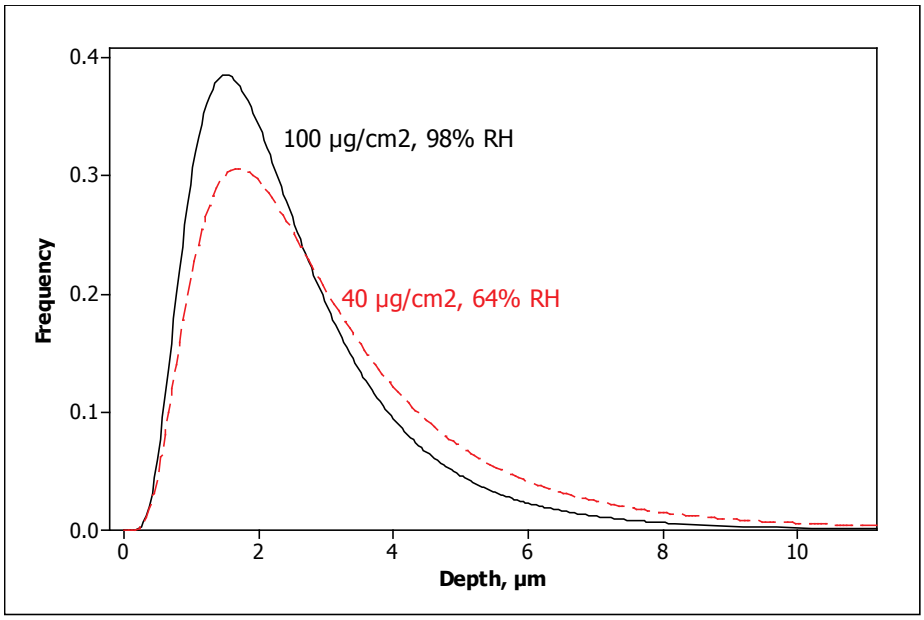

Figure 5.55 The lognormal distribution fit to pit depth data for 304L for two environmental conditions with deposited ferric chloride, 98% RH and a loading density of 100 µg/cm^2 and 64% RH and 40 µg/cm^2 indicates pit depths increased with decreasing RH and loading density.

5.6.2 Thin film experiments

The 304L alloy was exposed to three relative humidity values of 98, 85, and 64% with loading densities of ferric chloride of 100, 250, and 400 µg/cm^2 in the thin film experiments. The same loading densities as the drop experiments were used in the film experiments to compare samples with the same loading density and volume of deposited ferric chloride, but with different areas. A thin film on a 250 µg/cm^2, 85% RH samples is shown after the exposure in Figure 5.56.

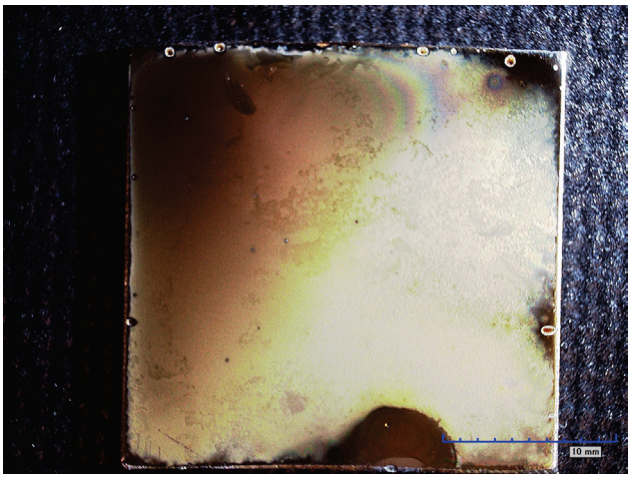

Figure 5.56 A thin film on a 304L sample after exposure with loading density 250 μg/cm^2 ferric chloride and exposed to 85% RH.

The appearance of general corrosion with decreasing loading density was the first noticeable trend observed. Figures 5.57 and 5.58 show the progression of the 304L sample from localized corrosion to general corrosion with decreasing RH and increasing concentration. The first image shows a pit on a 250 μg/cm^2, 98% RH sample (Figure 5.57). The second image for a 400 μg/cm^2, 64% RH sample, shows that a spot of general corrosion appeared with a pit in the middle (Figure 5.58).

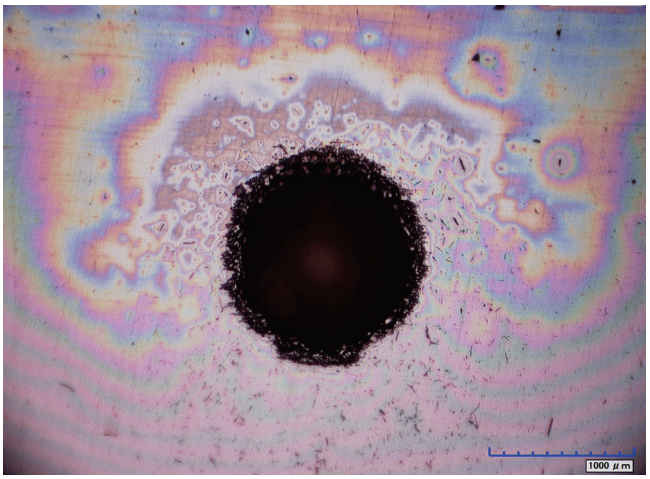

Figure 5.57 Localized corrosion on a 304L sample with loading density 250 μg/cm^2 ferric chloride and exposed to 98% RH for four days.

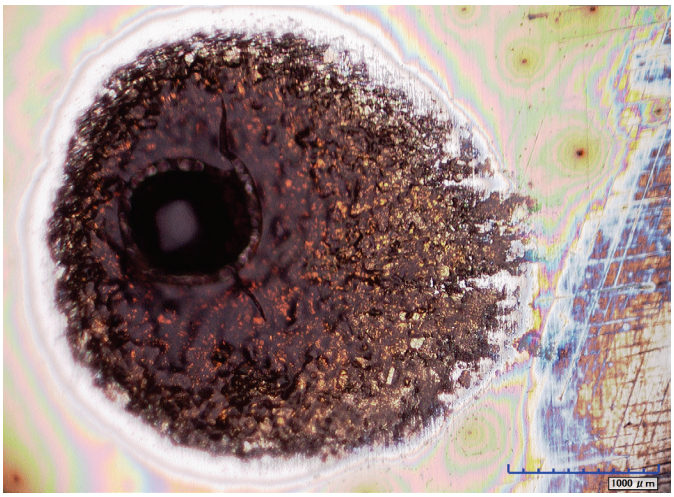

Figure 5.58 Evidence of general corrosion along with localized corrosion on a 304L sample with loading density 400 µg/cm^2 ferric chloride and exposed to 64% RH for four days.

The maximum pit depths were analyzed for each sample by fitting the depth data for the thin film experiments to the lognormal distribution (Figures 5.59 – 5.61). For 98 and 85% RH, pit depth values followed the expected trend of decreasing with decreasing RH and increasing with increasing loading density. However at the lower RH, 64%, and lower loading densities 100 and 250 µg/cm^2, the pit depths were higher than expected. At the highest loading density of 400 µg/cm^2 and 65% RH, the pit depths decreased, most likely due to an increase in general corrosion and a decrease in localized corrosion similar to the results found on the Aermet samples.

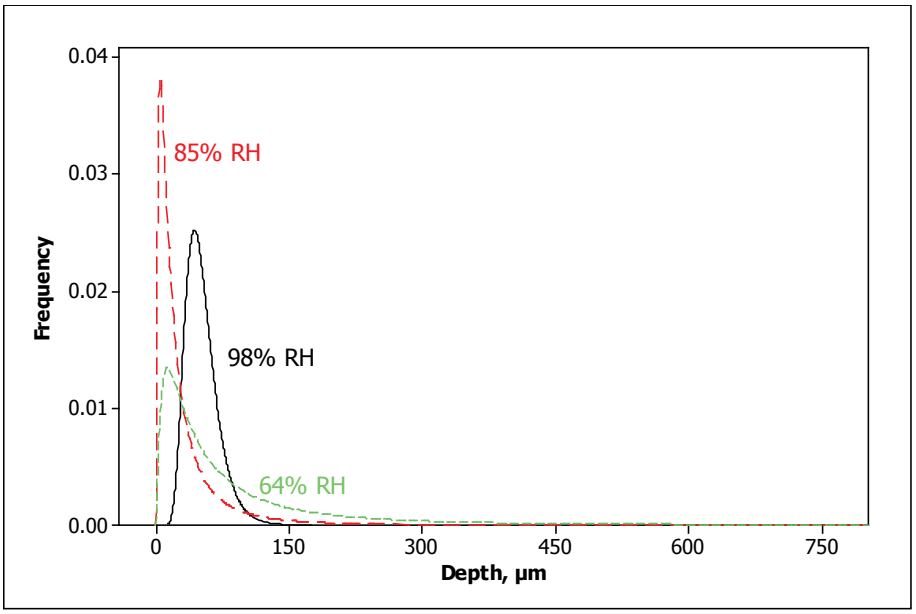

Figure 5.59 The lognormal distribution fit to depth data for 304L exposed to three RH values 98, 85, and 64% with a loading density 100 µg/cm^2 indicates pit depth increased with increasing relative humidity.

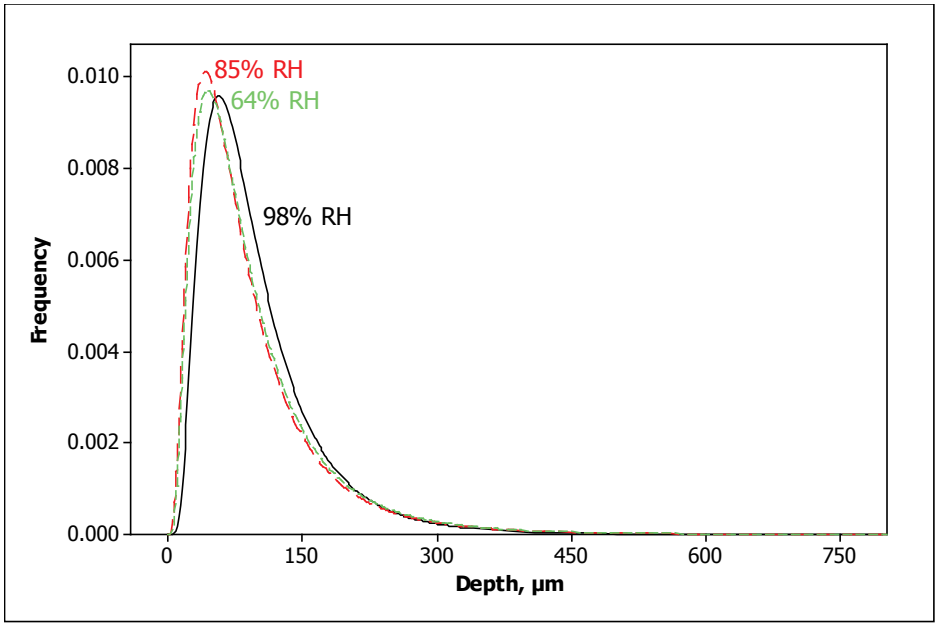

Figure 5.60 The lognormal distribution fit to depth data for 304L exposed to three RH values 98, 85, and 64% with a loading density 250 µg/cm^2 indicates pit depth increased with increasing relative humidity.

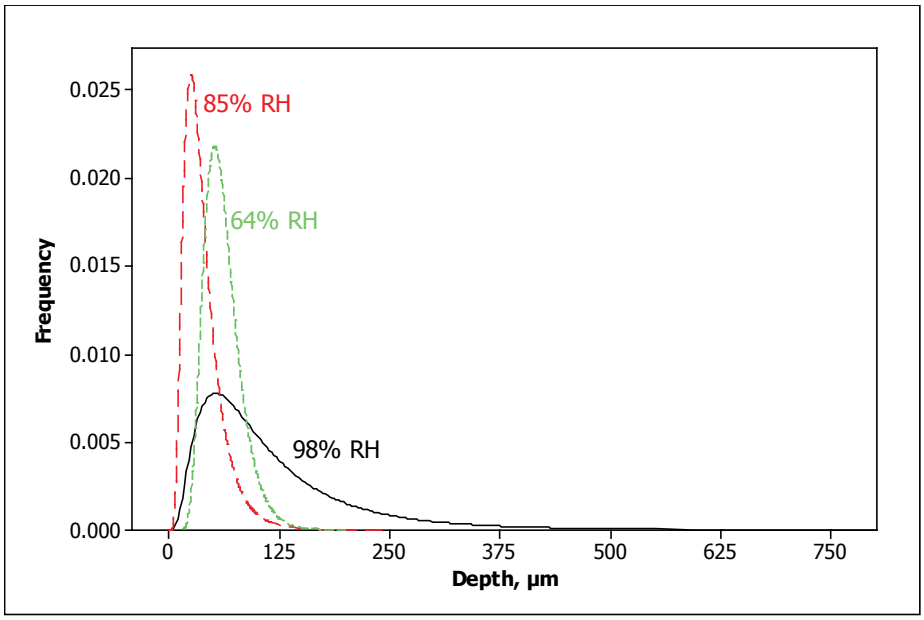

Figure 5.61 The lognormal distribution fit to depth data for 304L exposed to three RH values 98, 85, and 64% with a loading density 400 µg/cm^2 indicates pit depth increased with decreasing relative humidity.

Samples of 304L were exposed with a 250 µg/cm^2 thin film to a RH of 98% for three weeks to examine pit growth with time. Samples were removed after five exposure periods. Figure 5.62 shows that over time the maximum pit depths decreased and were at their highest value after only 50 hours. Only slight general corrosion occurred on all samples. The pit depths for the thin films obtained after four days were therefore representative of the maximum pit depths that could develop on 304L.

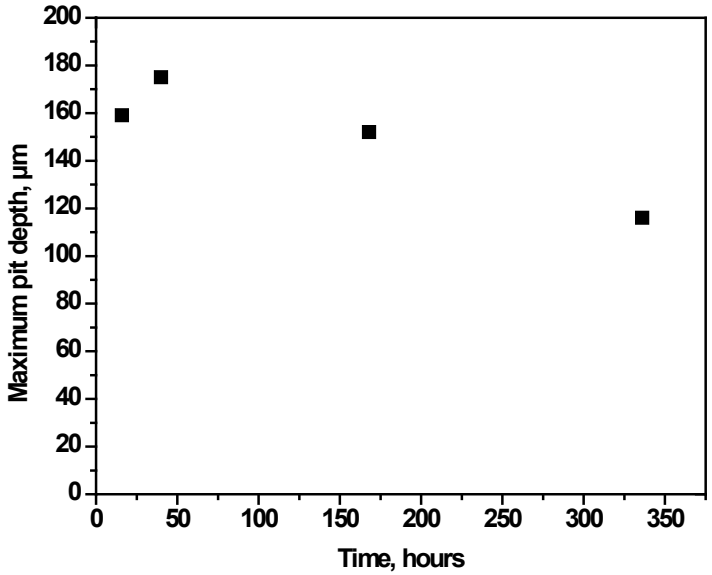

Figure 5.62 The maximum pit depth on a 304L sample exposed to 98% RH with 250 µg/cm^2 over the course of two weeks indicates pit depth does not increase with time after the initial twenty-four hours of the exposure.

5.6.3 Comparison of the drop and thin film experiments to predicted model values

The lognormal probability distribution was used to fit the maximum pit depth data for the drop and thin film exposures. The pit depths for a drop exposure with an environmental condition of 98% RH and three loading densities 100, 250, and 400 µg/cm^2 are marked with x symbols on the lognormal distributions (Figure 5.63). These markers show only the distribution of depth and do not convey any information about the frequency. As indicated in Figure 5.55 most of the pit depths are clustered on the left end of the distribution, with the predicted model values not shown on the figure because they are much further to the right, on the order of 75 to 400 µm. All of the pit depth values, that were unaffected by general corrosion, for the drop and thin film experiments were bounded by the predicted model value.

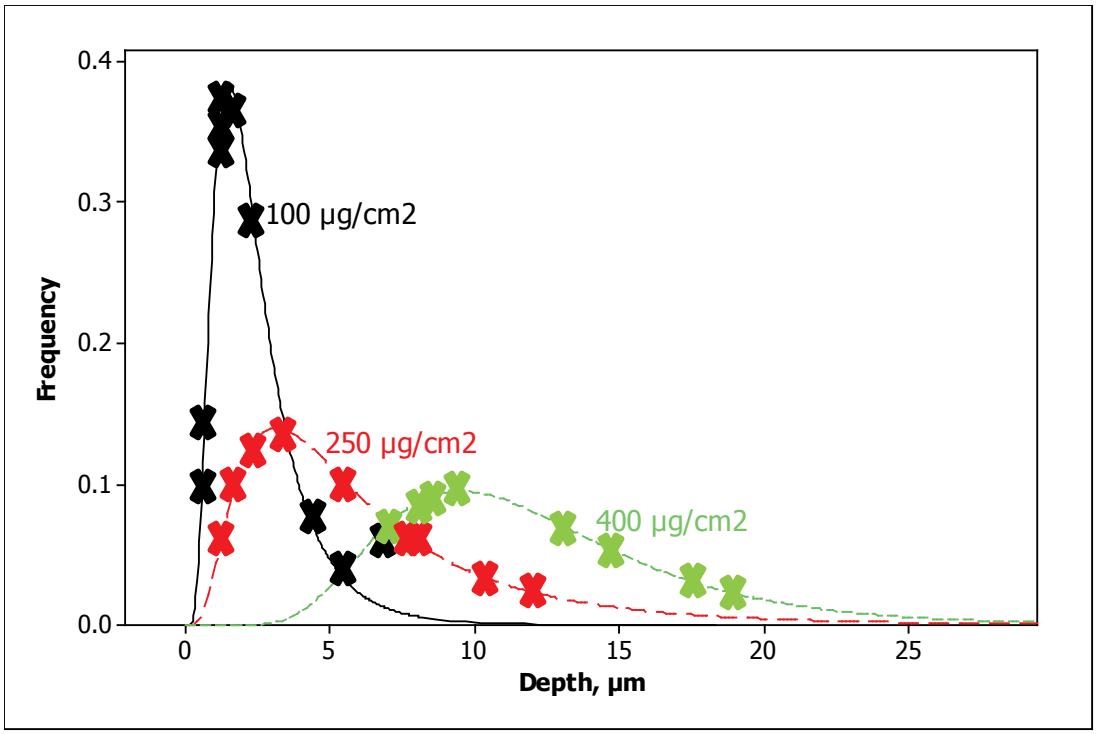

Figure 5.63 Pit depths marked by an x on the lognormal distributions fit to pit depth data for 304L exposed to 98% RH with loading densities of 100, 250, and 400 µg/cm^2 ferric chloride indicate pit depth data falls mostly on the left side of the distributions.

Although the computational model only predicts the maximum pit radius not the probability, data from the exposures can be fit to probability distributions to determine the probability of observing a specific maximum pit size. The probability of obtaining a pit depth larger than the predicted maximum pit size is presented in Table 5.1 for the drop and thin film experiments. These values were obtained in Minitab 16, using the lognormal probability distribution for a particular environmental condition. Some of the probabilities are higher than others because the experimental pit depths were closely bounded by the model values, and a small data set was used for each condition. With additional experiments, more accurate values for the probability of observing a pit depth greater than the predicted model value could be calculated by using a larger data set.

Table 5.1 Maximum pit depths for the drop and thin film experiments with same loading density and volume of ferric chloride

RH	Alloy – Loading Density, μg/cm^2	Predicted maximum pit radius, μm	Observed maximum pit depth, μm	Probability of a pit > model value	Geometry of the thin electrolyte
98%	316L – 100	47	5.6	2.437E-7	Drop
	Custom – 100	130	18.5	3.0303E-10	Drop
	304L – 100	75	6.1	4.0268E-10	Drop
	304L – 250	196	12.1	1.3934E-7	Drop/thin film
	304L – 400	375	19.7	0	Drop/thin film
65%	304L – 40	12	8.4	0.004700	Drop
98%	304L – 100	75	65.3	0.1067	Thin film
	304L – 250	196	142	0.07741	Thin film
	304L – 400	375	204	0.02750	Thin film
85%	304L – 100	64	34.7	0.1262	Thin film
	304L – 250	173	133	0.1099	Thin film
	304L – 400	350	95.3	5.4213E-6	Thin film
65%	304L – 100	49	316	0.5082	Thin film
	304L – 250	152	223	0.1584	Thin film
	304L – 400	410	87.1	2.2078E-9	Thin film

5.6.4 Comparison of a drop versus a thin film with same area

For the initial drop and thin film experiments, the loading density and volume of ferric chloride deposited were equal, while the area of the deposition was varied. In this comparison of pit depth under a drop and under a thin film, the area of the drop and the thin film were the same, while the loading density and the volume of ferric chloride on the samples were varied. As mentioned in 4.5.4, two exposures were performed in 98% RH. For one exposure, the radius of the drop and of the thin film, 1.2 cm, was greater than the equivalent cathode radius, 0.75 cm, or the radius necessary to achieve a certain maximum pit size as mentioned in Section 2.3.2. For the other exposure, the radius of the drop and of the thin film, 0.38 cm, was less than the equivalent cathode radius.

Several trends were observed for this experiment. The maximum pit depth under the thin film was approximately equal to the pit depth observed under the drop for the larger area (Table 5.2 and Figure 5.64). For the smaller area, as well, the maximum pit depth was approximately equivalent under the drop and the thin film (figure 5.65).

Table 5.2 Maximum pit depths for the drop and thin film experiments with same area

Geometry of the thin electrolyte	Area (cm^2)	Volume (µL)	Radius (cm)	Loading Density (µg/cm^2)	Water layer thickness (cm)	Maximum pit depth observed (µm)	Pit depth after removal of lacy cover (µm)	Predicted pit radius (µm)
Drop	5.76	700	1.2	5,900	0.122	12	614	>1000
Film	5.76	18	1.2	152	0.003	19	19	102
Drop	0.44	4	0.38	440	0.009	162	162	400
Film	0.44	20	0.38	2,200	0.045	125	125	>1000

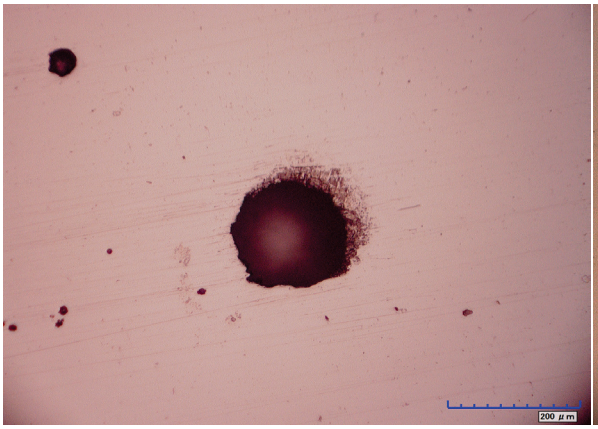

Figure 5.64 Pit with depth 125 µm on a 304L sample with a thin film of ferric chloride with radius 0.38 cm and exposed to 98% RH.

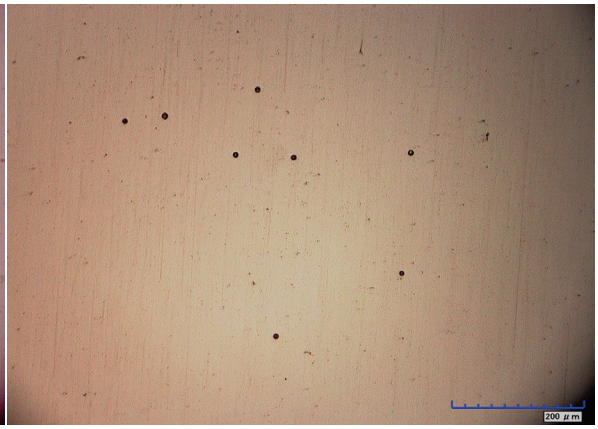

Figure 5.65 Small pits with maximum pit depth 19 µm on a 304L sample with a thin film of ferric chloride with radius 1.2 cm and exposed to 98% RH.

Under both drops of ferric chloride, indications of a lacey covering, as mentioned in Section 2.2.4 was observed (Figures 5.66-5.67). After polishing the surface of the sample with 120 grit paper, part of the material was removed under the drop with radius

0.38 cm, and the pit remained approximately the same size with the same depth (Figure 5.68). However, after polishing the surface of the sample with 1200 grit and then 120 grit paper, the pit underneath the drop of ferric chloride, with radius 1.2 cm, was larger with a depth of 614 μm (Figures 5.69-5.70). Larger pit sizes now were observed under the large drop than the thin film. The lacey covering is indicative of undercutting of the pit and a limitation on the anode since the pit is unable to grow as an open cavity but still grows with a metallic film covering it. In Section 7, studies to further examine the undercutting of pits on 304L samples with deposited ferric chloride using a FIB will be mentioned.

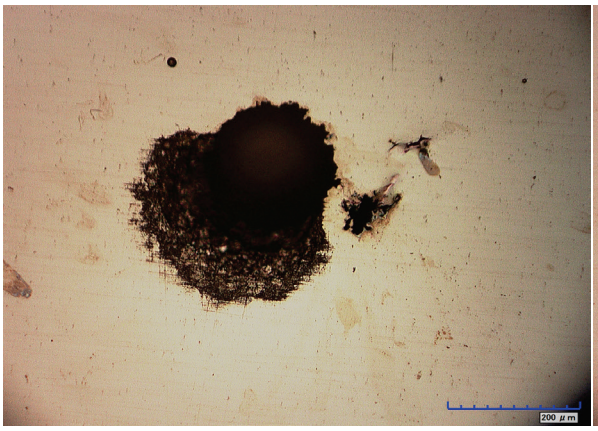

Figure 5.66 Pit with depth 162 μm on a 304L sample with a drop of ferric chloride with radius 0.38 cm and exposed to 98% RH.

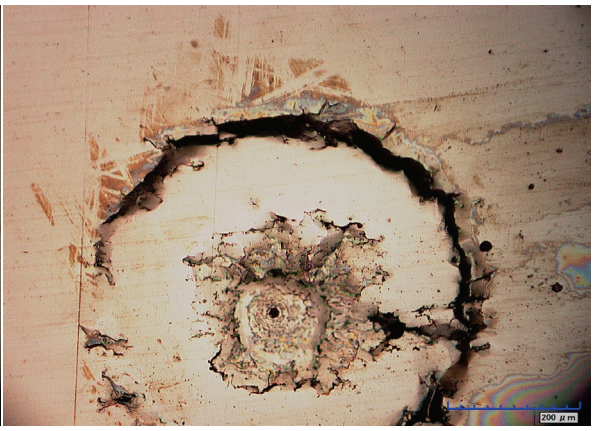

Figure 5.67 Pit on a 304L sample with a drop of ferric chloride with radius 1.2 cm and exposed to 98% RH.

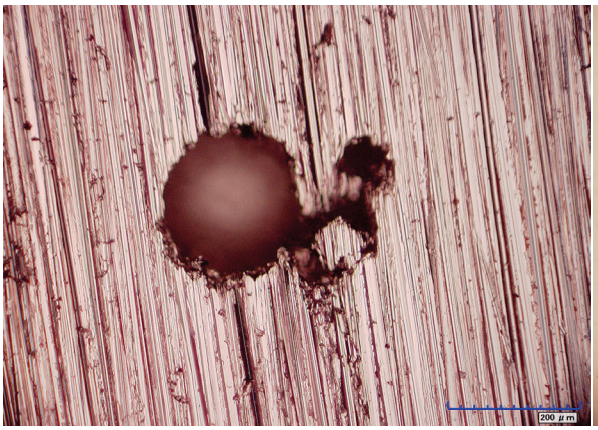

Figure 5.68 Pit with depth 162 μm after polishing the surface with 120 grit paper on a 304L sample with a drop of ferric chloride with radius 0.38 cm and exposed to 98% RH.

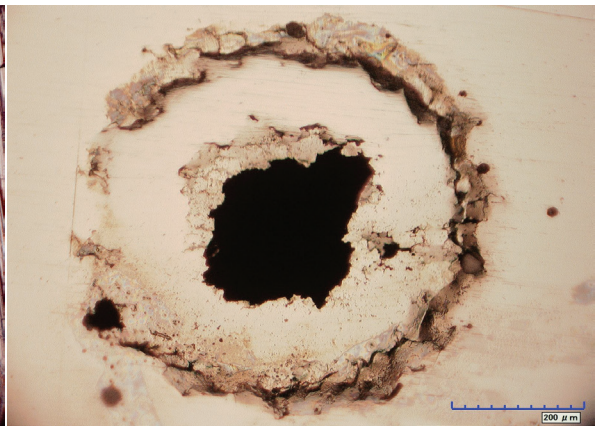

Figure 5.69 Pit beneath a lacy covering after polishing the surface with 1200 grit paper on a 304L sample with a drop of ferric chloride with radius 1.2 cm and exposed to 98% RH.

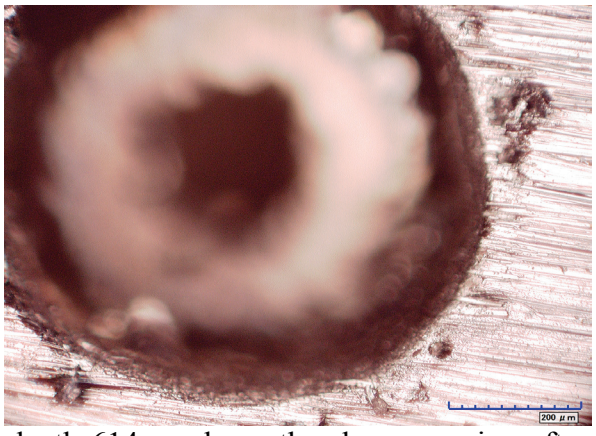

Figure 5.70 Pit with depth 614 μm beneath a lacy covering after polishing the surface with 120 grit paper on a 304L sample with a drop of ferric chloride with radius 1.2 cm and exposed to 98% RH.

5.7 Chemical modeling using OLI

Chemical modeling was done using OLI Systems Analyzer Studio 3.1 to determine the deliquescence properties of binary and ternary mixtures. The values calculated, such as the conductivity and the relationship of salt concentration, were then used in the determination of the water layer thickness that was input into the computational model.

The accuracy of the data determined using OLI software was validated by comparing predicted values to experimental values found in literature. Values for sodium chloride concentration as a function of relative humidity were found to correlate well with a R^2 value of 0.9999 (Figure 5.71).

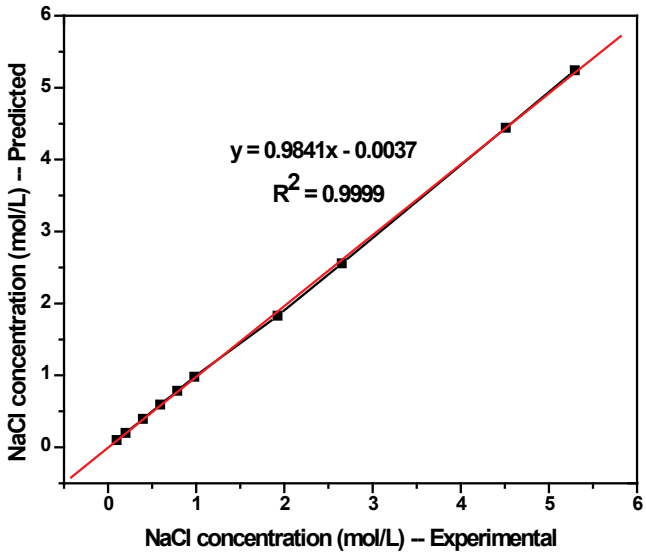

Figure 5.71 Comparison of literature values for sodium chloride as a function of relative humidity to predicted values using OLI software indicates a high correlation with a R^2 value of 0.9999.

5.7.1 Binary salt solutions

The deliquescence properties of sodium chloride and ferric chloride were determined and will be discussed in this section.

Figure 5.72, shows that concentration of sodium chloride increased with decreasing relative humidity. The deliquescence RH of sodium chloride is approximately 75% RH.

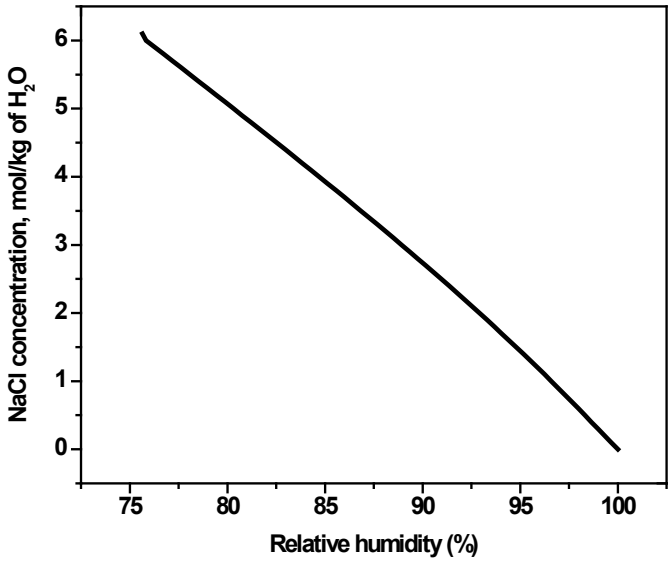

Figure 5.72 Predicted values using OLI software indicate increased concentration with decreased relative humidity for sodium chloride.

The oxygen solubility at 1 atm in sodium chloride increased with increasing RH (Figure 5.73).

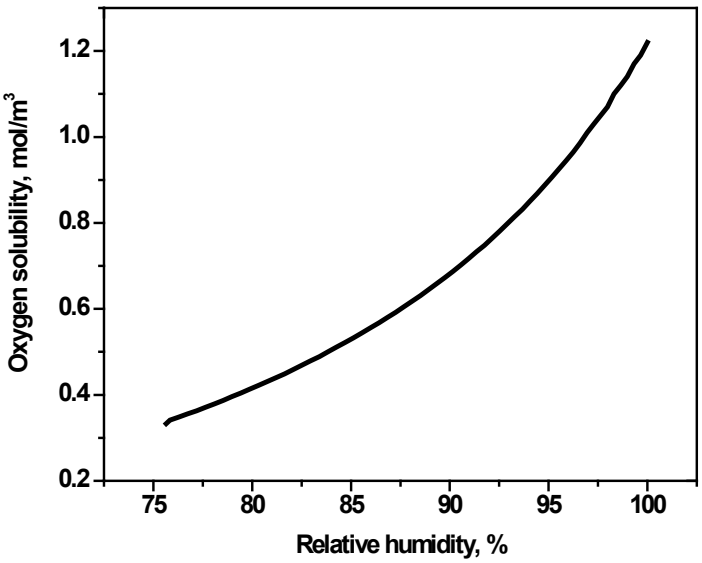

Figure 5.73 Predicted values using OLI software indicate increased oxygen solubility with increased relative humidity for sodium chloride.

Density and conductivity were both found to decrease with increasing relative humidity for sodium chloride (Figure 5.74 and 5.75).

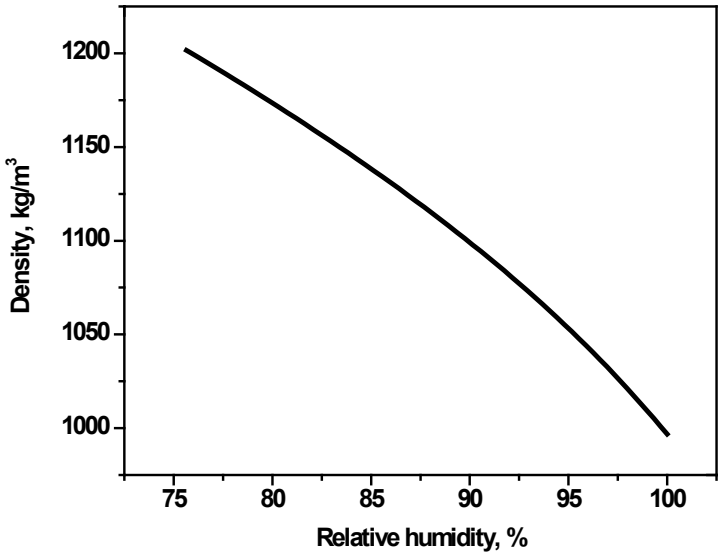

Figure 5.74 Predicted values using OLI software indicate decreased density with increased relative humidity for sodium chloride.

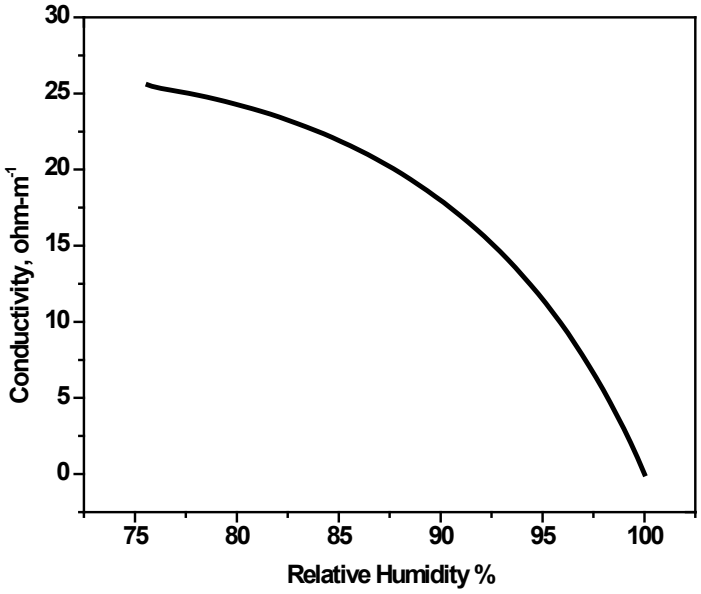

Figure 5.75 Predicted values using OLI software indicate decreased conductivity with increased relative humidity for sodium chloride.

The deliquescence properties of ferric chloride also were determined. Similarly to the sodium chloride solution, concentration increased with increasing RH (Figure 5.76). The deliquescence RH of ferric chloride was calculated as approximately 40% RH.

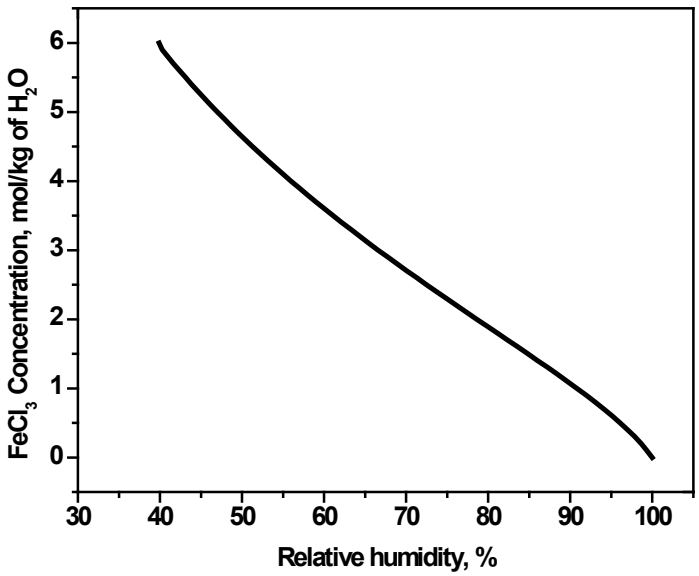

Figure 5.76 Predicted values using OLI software indicate increased concentration with decreased relative humidity for ferric chloride.

In comparison to the sodium chloride solution, the oxygen solubility followed the opposite trend in ferric chloride at 1 atm, decreasing with increasing RH (Figure 5.77).

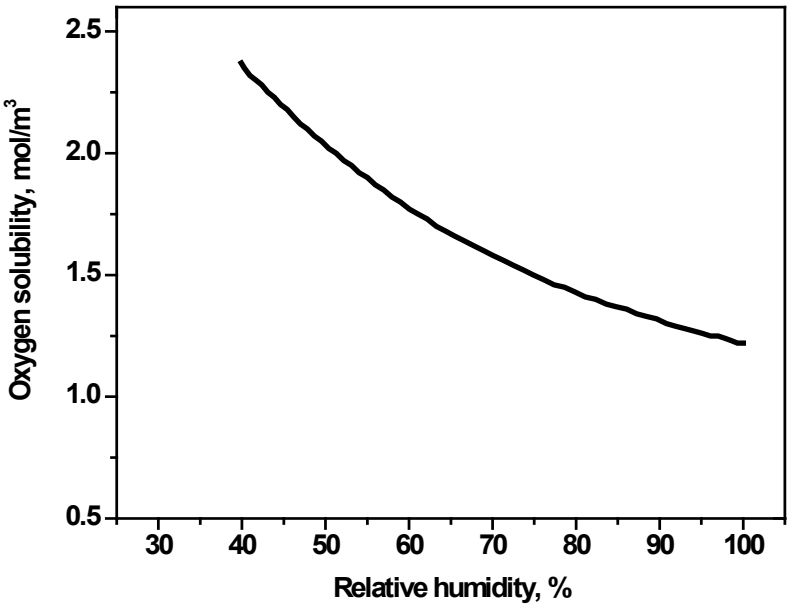

Figure 5.77 Predicted values using OLI software indicate decreased oxygen solubility with increased relative humidity for ferric chloride.

The density and conductivity both decreased with increasing relative humidity in the ferric chloride solution as seen for sodium chloride (Figure 5.78 – 5.79).

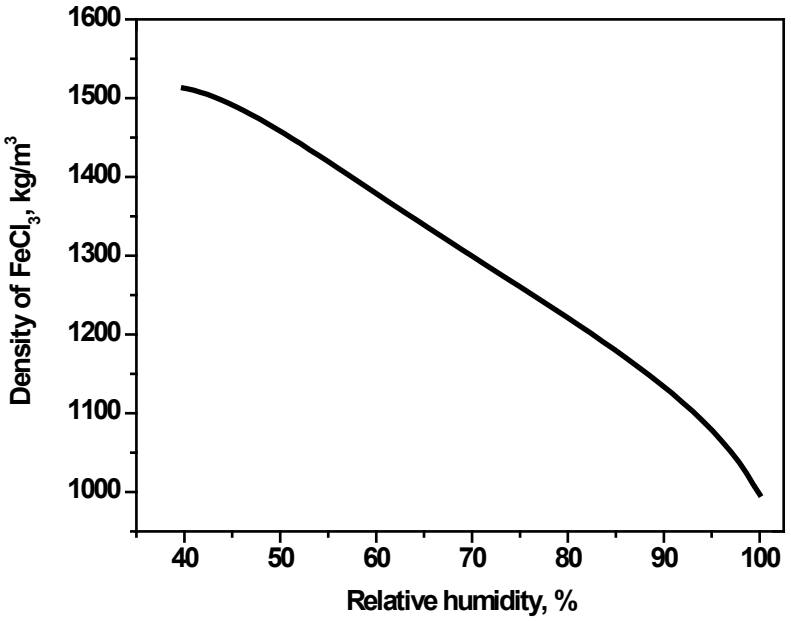

Figure 5.78 Predicted values using OLI software indicate decreased density with

increased relative humidity for ferric chloride.

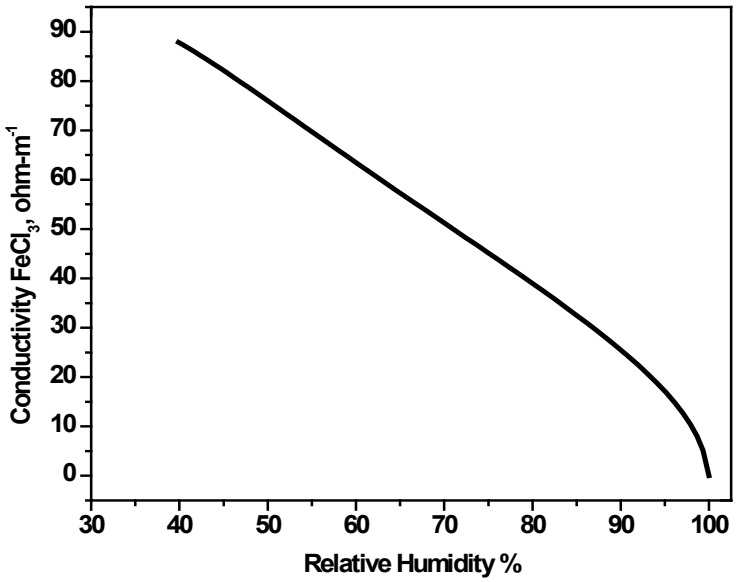

Figure 5.79 Predicted values using OLI software indicate decreased conductivity with increased relative humidity for ferric chloride.

5.7.2 Ternary salt mixtures

The deliquescence RH of the individual salts and of the mixture was modeled using OLI. Although this information was not used for the experiments performed for this thesis, to extend the model to more realistic solutions that would be seen in the field, the deliquescence properties of mixed salt solutions were determined.

The $NaCl$-NH_4Cl-H_2O mixture first was examined to confirm the methodology using the OLI software (Figure 5.80). The figure produced matched well to the ternary found in literature. The mutual deliquescence relative humidity of 69.2% had 0.58% deviation from the value of 68.8% in Wexler and Seinfield.[39] The individual relative humidity values of 75.5% and 77.2% had percent deviations of 0.40% and 0%, respectively.

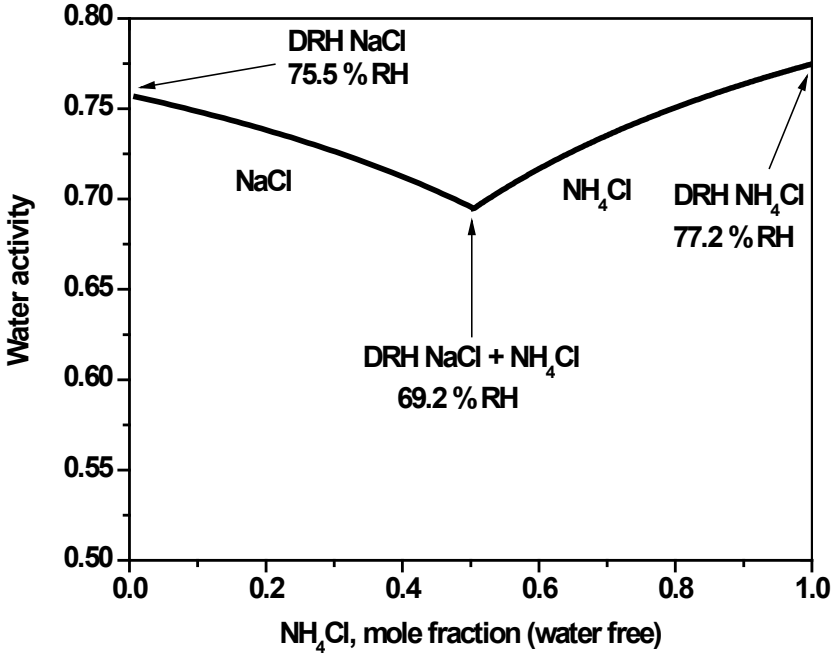

Figure 5.80 The mutual deliquescence relative humidity of 69.2% has a 0.58% deviation from the RH of 68.8% found in literature calculated for a ternary mixture NaCl-NH_4Cl-H_2O.

The NaCl-$FeCl_3$-H_2O ternary next was modeled using OLI. A deliquescence RH of 75.5 % was calculated for sodium chloride, while a RH of 39.9% was determined for the deliquescence RH of ferric chloride (Figure 5.81). The theoretical mutual deliquescence relative humidity was less than that of either of the individual components, at 39.6% RH.

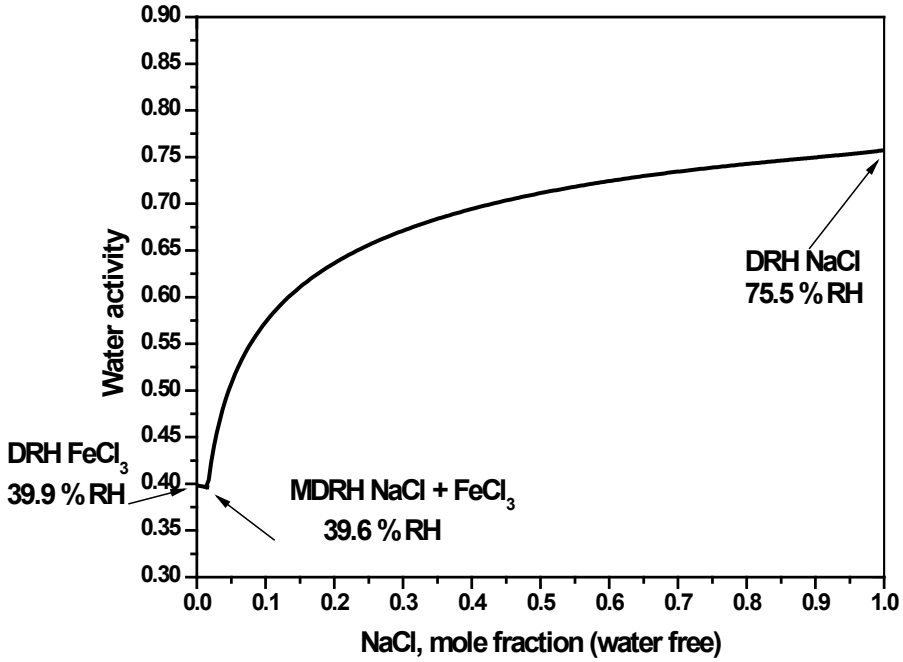

Figure 5.81 The mutual deliquescence relative humidity of 39.6% calculated for the ternary mixture NaCl-$FeCl_3$-H_2O.

5.8 Sensitivity of the computational model to input parameters

The sensitivity of the predicted model values for pit size to variations in input parameters, such as the pit stability product, the Tafel slope, the corrosion potential, the repassivation potential, and the chemical properties of the thin electrolyte will be discussed in this section. The Custom 465 alloy will be used as an example to show the effect these parameters have on pit size for an alloy exposed to the environmental condition of 600 $\mu g/cm^2$ sodium chloride and a RH of 98%.

5.8.1 Pit stability product

Using experimental values for the pit stability product for Custom 465, the effect of the pit stability product on the predicted maximum pit radius was examined (Figure 5.82). Of the three pit stability products chosen, 1.85 and 2.40 A/m were the lowest and

highest values observed for Custom, and 2.12 A/m was the average of the five values obtained for Custom in different sodium chloride concentrations. By increasing the pit stability product by 0.28 A/m from 2.12 A/m to 2.40 A/m, the maximum pit size increased from 103 to 108 μm. A greater difference in pit depth was observed when decreasing the pit stability product from 2.12 to 1.85 A/m. For this decrease in pit stability product, the maximum pit radius increased from 108 to 141 μm.

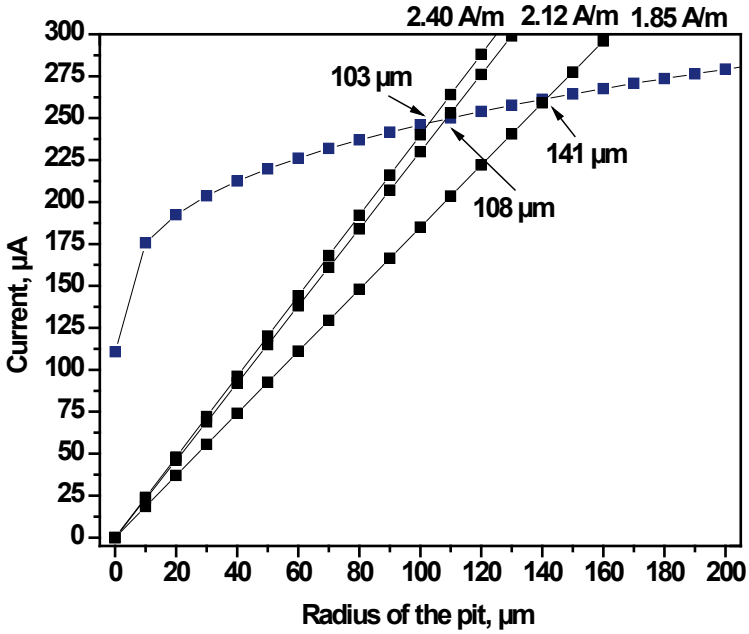

Figure 5.82 The sensitivity of the predicted pit radii to variations in the pit stability product for a Custom 465 sample with 600 μg/cm^2 sodium chloride and a RH of 98%.

5.8.2 Tafel slope

The Tafel slope was investigated for its effect on the maximum pit radius. As Figure 5.83 indicates for the polarization scan for Custom 465, two different slopes, -0.0653 V/dec and -0.111V/dec could be fit to the same data.

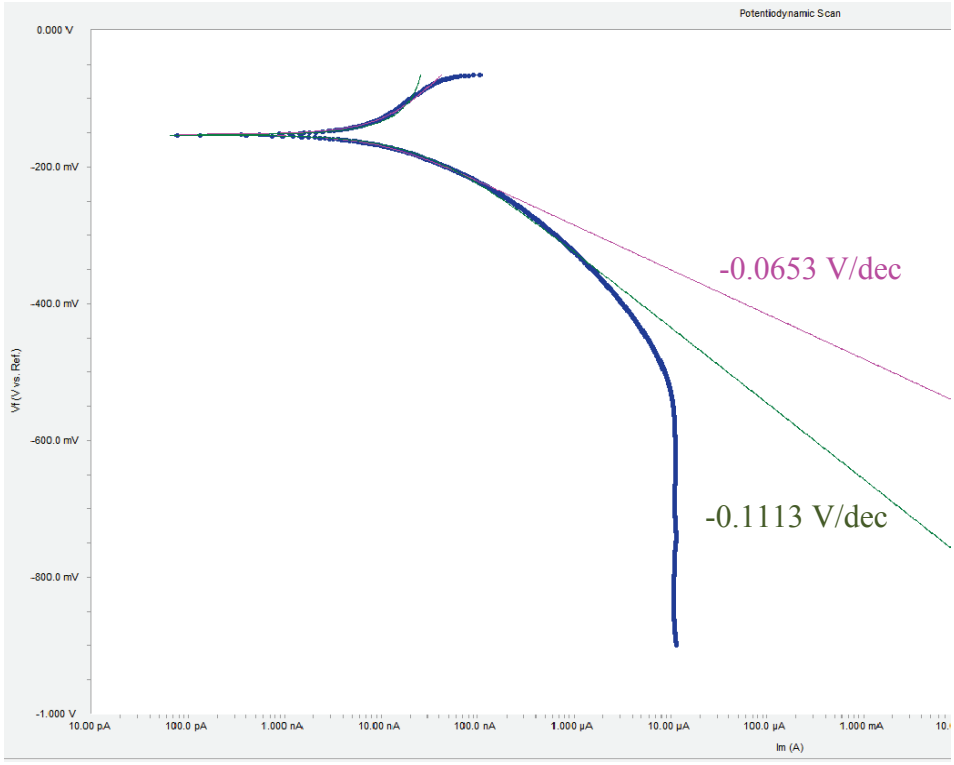

Figure 5.83 Two Tafel slopes, -0.0653 V/dec and -0.1113 V/dec fit to the same cathodic polarization scan for Custom 465 with 600 µg/cm^2 sodium chloride and a RH of 98%.

To examine this effect the Tafel slope for a Custom 465 sample was varied by +/- 5% and by +/- 50%. Variations of +/-5% changed the pit radius by +/- 5 µm (Figure 5.84). A 50% increase of the Tafel slope decreased the maximum pit radius by approximately 22% of the original value. A 50% decrease of the Tafel slope, however, greatly increased the maximum pit radius. Although a large increase could occur with a Tafel slope < 0.05 V/dec, such a low Tafel slope is unlikely to be observed.

For this data set a Tafel slope was estimated to fit the polarization curve. In the future, a better methodology for determining the the integral in Equation 2.8 would be to numerically integrate the polarization curves using Mathematica. This method would reduce any error in the predicted model value due to force-fitting Tafel behavior.

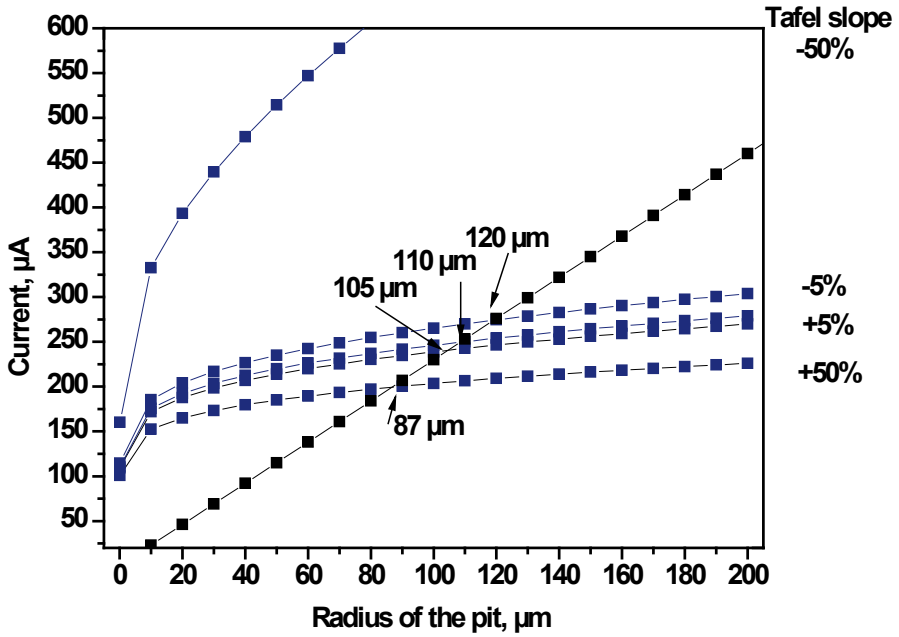

Figure 5.84 The sensitivity of the predicted pit radii to variations in the Tafel slope for a Custom 465 sample with 600 µg/cm^2 sodium chloride and a RH of 98%.

5.8.3 Corrosion potential

The length of the open-circuit potential monitoring before the cathodic scan has an effect on the potential at the end of the monitoring. As mentioned in Section 5.3, for the three stainless steel alloys, the potential rises over the course of the 24-hour monitoring. If the scan is paused early, some of the cathodic potential is lost and a lower corrosion potential (E_{corr}) will be calculated for the cathodic scan. A lower corrosion potential value is reflected in the model by a smaller difference in E_{corr} and E_{rp} and thus smaller pit values.

E_{corr} values for Custom 465 in 1.5 M sodium chloride solution are examined for their effect on the maximum pit radius. The highest E_{corr} value of -153 mV_{SCE} was determined for a sample with a 24-hour open-circuit potential monitoring. The four other E_{corr} values were calculated by decreasing the E_{corr} value by 50, 100, 150, and 200 mV_{SCE},

respectively. These E_{corr} values could have been obtained if the open-circuit potential monitoring of Custom 465 in 1.5 M sodium chloride solution had been shortened (Figure 5.13).

Figure 5.85 indicates that changing the E_{corr} values by 100 mV_{SCE} decreased the maximum pit radius, from 109 to 89 μm. Decreasing the E_{corr} value even further by 100 mV_{SCE}, decreased the maximum pit radius from 109 to 77 μm or by 32 μm.

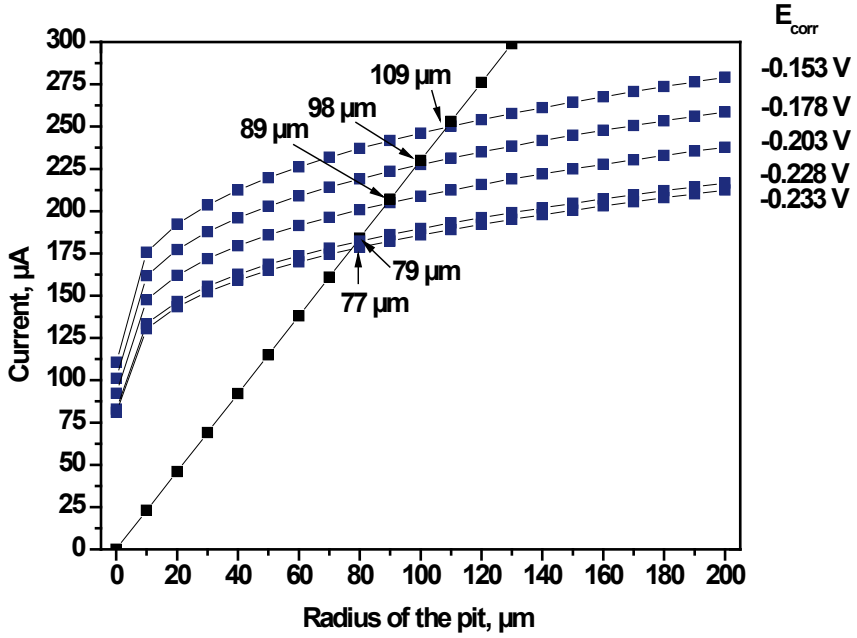

Figure 5.85 The sensitivity of the predicted pit radii to variations in the corrosion potential for a Custom 465 sample with 600 μg/cm^2 sodium chloride and a RH of 98%.

5.8.4 Repassivation potential

The effect of E_{rp} on the maximum pit radius was examined for Custom 465, for an environmental condition of 600 μg/cm^2 of sodium chloride and a RH of 98%, by varying the E_{rp} by +/- 50 mV_{SCE} and then by +/- 100 mV_{SCE} (Figure 5.86).

These results indicate E_{rp} has a strong effect on maximum pit radius. With a change of +/- 50 mV_{SCE} of the E_{rp}, the maximum pit radius varied by approximately +/-

20 μm. Similarly an increase of 100 mV_{SCE}, increased the maximum pit radius by 44 μm, while decreasing the E_{rp} by 100 mV_{SCE}, decreased the pit radius by 32 μm.

As observed in Sections 5.8.3 and 5.8.4, varying the E_{corr} or the E_{rp}, changes the difference between the E_{corr} and the E_{rp}. As reflected in Figures 5.85 and 5.86, this has a strong effect on the maximum pit radius and will be examined further in Section 6.1.

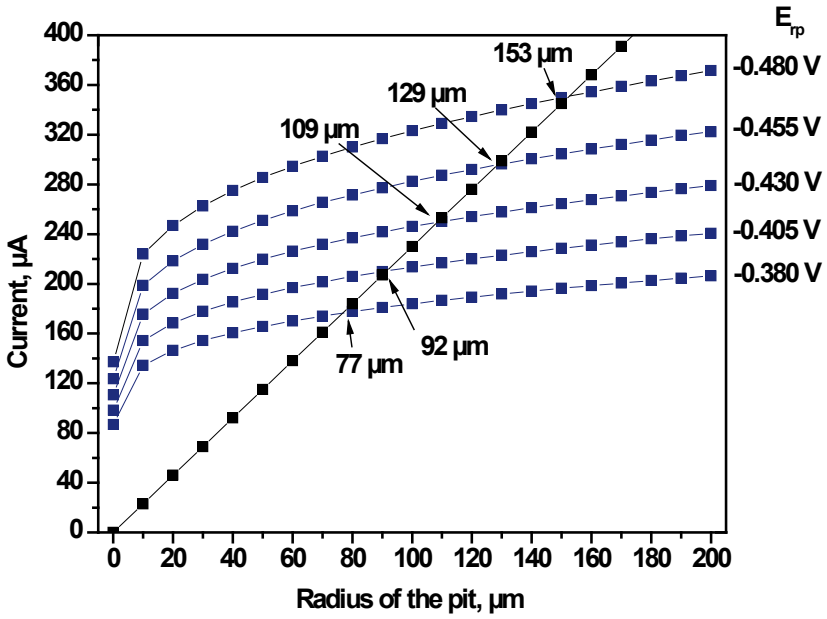

Figure 5.86 The sensitivity of the predicted pit radii to variations in the repassivation potential for a Custom 465 sample with 600 μg/cm^2 sodium chloride and a RH of 98%.

5.8.5 Chemical properties of the thin electrolyte

The chemical properties determined for the binary mixtures using OLI Analyzer Studio 3.1 were necessary for the determination of input parameters into the computational model. Although experimental data exists for sodium chloride for factors, such as conductivity and density, no such information exists for ferric chloride. Therefore, the values determined in OLI were important in the prediction of pit radius for samples with deposited ferric chloride.

As shown in Table 5.3, this information has an effect on the predicted pit radius. For the two environmental conditions, with 100 μg/cm^2 ferric chloride and relative humidity values of 98 and 64%, the predicted pit radii are 75 and 49 μm, respectively. If for the 64% environmental condition, the conductivity for 98% is used, the predicted pit radius is 4 μm, a 45 μm difference in pit radius. Similarly if the density for 98% is used instead of the density corresponding to 64%, the predicted pit radius is 70 μm, a 21 μm difference. The largest variation is pit radius is observed when the molality is not adjusted for 64% RH. The pit radius is then predicted as > 600 μm. These findings indicate that the relationship of these chemical properties to RH is important to predicting an pit radius. If the correct value is not used, an inaccurate value of pit radius will be predicted.

Table 5.3 The effect of variations of the deliquescence properties of ferric chloride on the predicted pit radii for 304L

Environmental Conditions	Conductivity, $(\Omega\text{-m})^{-1}$	Density, kg/m^2	Molality, mol/kg H_2O	Water layer thickness, m	Predicted Pit Radius, μm
98% RH, 100 μg/cm^2	10.5241	1037.25	0.3	2.26*10-5	75
64% RH, 100 μg/cm^2	58.1067	1344.18	3.2	2.37*10-6	49
64% RH, 100 μg/cm^2, change in conductivity	**10.5241**	1344.18	3.2	2.37*10-6	4
64% RH, 100 μg/cm^2, change in density	58.1067	**1037.25**	3.2	3.07*10-6	70
64% RH, 100 μg/cm^2, change in molality	58.1067	1344.18	**0.3**	1.74*10-5	> 600

6 Discussion

Pitting on ferrous alloys under atmospheric exposure conditions has been difficult to model in the past. An indicator of a material's likelihood to undergo localized corrosion would be extremely desirable for use in the defense industry, where ferrous alloys are widely employed. As mentioned in Section 1, structural integrity calculations are used to calculate the lifetime of many defense structures. In the past, these calculations were unable to account for the damage accumulation from atmospheric corrosion. A computational model has been developed, however, that predicts the maximum pit size on ferrous alloys under atmospheric conditions. This predicted damage size for a specific material can be combined with data on the hydrogen uptake associated with the same pit size to calculate the effective damage accumulation from atmospheric corrosion. This damage size can then be used as an indicator to rank corrosion susceptibility of ferrous alloys to atmospheric corrosion and can also be input into structural integrity calculations to calculate the lifetime of a material.

The goal of this study was to evaluate how well the computational model bounded pit depths on laboratory exposures, where environmental conditions were strictly controlled. The accuracy of the model was determined by comparing predicted values of pit radii to experimental values observed on laboratory exposures. The extent to which several factors, including the pit stability product, the corrosion potential, the repassivation potential, the Tafel slope, and finally the geometry and chemistry of the thin electrolyte have an effect on pit size also were taken into account when assessing how well the model bounded experimental values. With this knowledge, suggestions will

be developed for a laboratory exposure that will give the most accurate representation of the corrosion susceptibility of materials to atmospheric corrosion in the field.

The accuracy of a model often is sensitive to several factors as mentioned. For this computational model, the input parameters, which have an effect on the predict value of pit size, will be discussed. Properties of the exposures, including exposed area of the coupons and geometry of the deposited thin electrolyte, can have an effect on the size to which a pit can grow. The impact of these properties on the comparison of the experimental values to predicted model values also will be discussed in this section. Lastly, other findings from the laboratory exposures, such as cycling relative humidity values, the effect of general corrosion on pit size, and the use of probability distributions to model predicted pit values will be mentioned.

6.1 Sensitivity of the model to the input parameters

Several input parameters, including the pit stability product, the Tafel slope, the corrosion potential, the repassivation potential, and the chemical properties of the thin electrolyte were examined in Section 5.8 for their effect on pit size.

The pit stability product is equivalent to the slope of the line for the minimum anodic current. Changing this value, or the slope of the line, will vary the intersection of the minimum anodic current with the maximum cathodic current and thus change the maximum predicted radius. Over the range of pit stability products observed for Custom 465 in the three sodium chloride concentrations (Figure 5.7), the predicted pit radius varied by no more than 40 μm. Using the average of the pit stability product values in the computational model reduces the error in pit size due to variability of pit stability product values.

The Tafel slope is important in the determination of the value of the integration in Equation 2.8. As observed in Figure 5.71, some variation was seen with changing Tafel slope. Generally, the difference in pit size for varying Tafel slope was small, approximately +/-25 μm. In the future, this variation can be eliminated by using the integration of the polarization curve over a range of potentials, E_{corr} to E_{rp}, instead of fitting a line to the polarization curve. Although the Tafel slope changes the value of the integration, the range of potentials, from E_{corr} to E_{rp} over which the integration is calculated, has a much larger effect on the maximum pit radius as mentioned in Section 5.8.4. As observed in the Figures 5.85 and 5.86, the maximum pit radius changes with any variation in E_{corr} or E_{rp}.

To determine which potential had the greater effect on maximum pit size, values for the maximum pit radius were plotted for different E_{corr} and E_{rp} values as a function of difference in potential between the E_{corr} and E_{rp} or ΔE (Figure 6.1). The intersection of the two lines, corresponds to the maximum pit radius for Custom 465, with the experimental values determined in Sections 5.2 and 5.3, for an environmental condition of 600 $\mu g/cm^2$ of sodium chloride and a RH of 98%. For this condition, the E_{corr} is -143 mV_{SCE}, and the E_{rp} is -430 mV_{SCE}, with a ΔE of 0.277 V_{SCE}. To the left of this value, the E_{corr} and E_{rp} were varied as shown in Figure 6.2. The E_{corr} was decreased by 100 mV_{SCE}, while the E_{rp} was held constant, and the E_{rp} increased while the E_{corr} was held constant, for a ΔE of 0.177 V_{SCE}. These potentials were then used to predict the maximum pit radius. This procedure was repeated to obtain pit values for a ΔE of 0.077 V_{SCE}. To the right of the intersection of the E_{corr} and the E_{rp} maximum pit radius values, the E_{corr} was increased by 100 mV_{SCE}, while the E_{rp} was held constant and the E_{rp} was decreased by

100 mV_{SCE}, while the E_{corr} was held constant for a ΔE of 0.377 V_{SCE} (Figure 6.3). At low values of ΔE, the E_{corr} had the greater effect on pit radius, with a difference in pit values of approximately ≤ 20 μm (Figure 6.1). However at large values of the ΔE, the E_{rp} had a larger impact on maximum pit radius, with a difference in the pit radii of 71 μm.

For experimentally determined input parameters, the model is most sensitive to the difference in potential between the E_{corr} and the E_{rp}. Although the E_{corr} changes the maximum pit radius, the E_{rp} has the greater impact on the integration values and thus pit size because it corresponds to higher current densities.

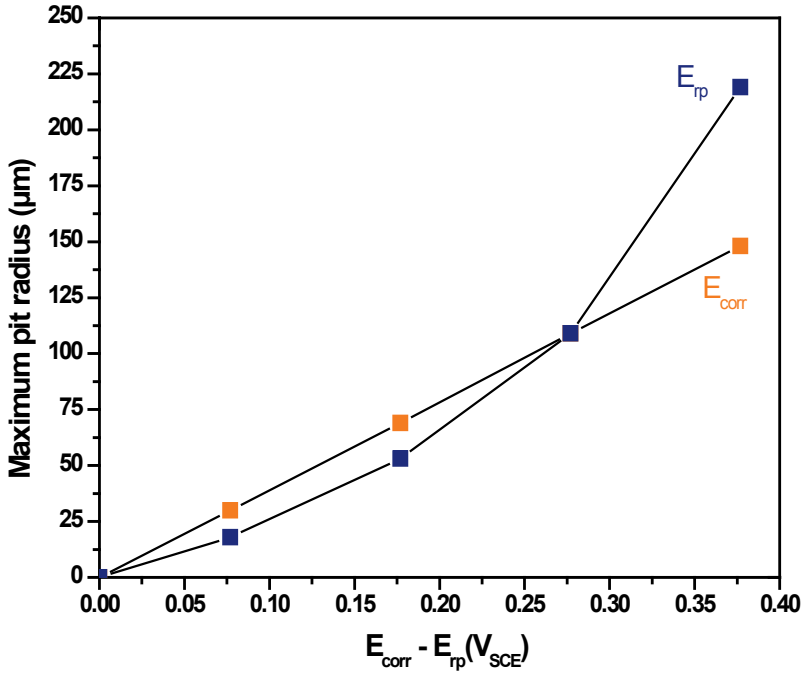

Figure 6.1 The increase in maximum pit radius with an increase in the difference between E_{corr} and E_{rp} for Custom 465 with a loading density of 600 μg/cm^2 sodium chloride and a RH of 98%.

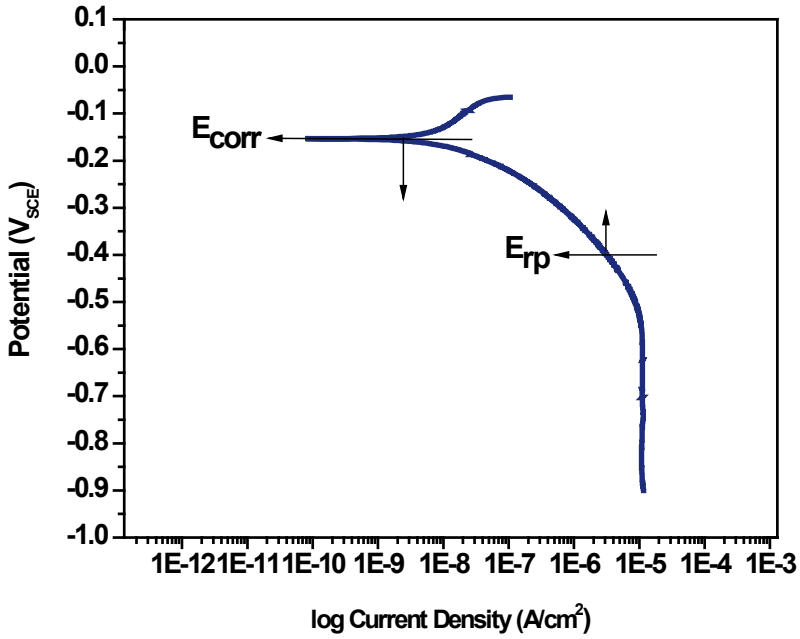

Figure 6.2 Determination of the predicted radius values by first holding E_{rp} constant while lowering E_{corr} and then holding E_{corr} constant while increasing E_{rp} for Custom 465 with a loading density of 600 μg/cm^2 sodium chloride and a RH of 98%.

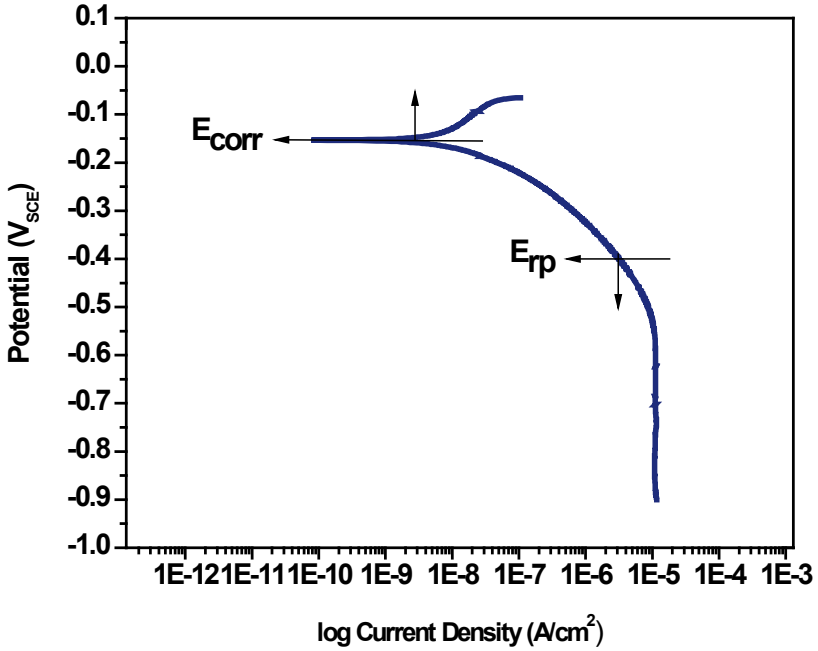

Figure 6.3 Determination of the predicted radius values by first holding E_{rp} constant while increasing E_{corr} and then holding E_{corr} constant while lowering E_{rp} for Custom 465 with a loading density of 600 μg/cm^2 sodium chloride and a RH of 98%.

The deliquescence properties determined using OLI software are the last input parameter needed to accurately determine the predicted maximum pit size for a specific thin electrolyte chemistry. The salt concentration and density of the salt mixture as a function of relative humidity are both necessary in the calculation of the water layer thickness that is then used in the calculation of pit size. The results in Table 5.3 indicate that both of these chemical properties along with the conductivity will have a large effect on the predicted pit radius. As mentioned in Section 5.4 and shown in Figure 5.29, the predicted pit radii for 64% RH, were dependent on the values of the water layer thickness. The pit values predicted for the two lower loading densities 100 and 250 $\mu g/cm^2$ were smaller than the higher loading density of 400 $\mu g/cm^2$ because of their small water layer thicknesses.

With increasing complexity of the salt mixture, modeling the deliquescence properties becomes even more important. For an alloy that has deposited sodium chloride and also corrodes, determining the NaCl-$FeCl_3$-H2O ternary is vital for calculating the mutual deliquescence relative humidity that will change values such as the conductivity and density, all of which were shown to have a large effect on pit size. For any laboratory exposure performed to correlate with a specific environmental condition, it is critical that the chemical properties are determined and adjusted in the model for each different mixture.

6.2 Equivalent cathode

The equivalent cathode area necessary to support a pit of a certain size is an important value to consider when determining the area of a coupon to be exposed in a laboratory-controlled or outdoor exposure. The three stainless steels, Custom 465, 316L,

and 304L with deposited sodium chloride and exposed to 90 and 95% RH, had pit radii that were < 2 μm as reported in Section 5.5.1. The coupons used for the 304L and 316L samples had area 5.76 cm^2, while the coupons used for Custom 465 had area 0.20 cm^2. These areas are significantly smaller than the panels of area, 150 cm^2, used for outdoor exposures in Muto et al, where pits with radii approximately 50 μm were observed. For the 304L alloy, with the most aggressive environment of 600 $\mu g/cm^2$ of sodium chloride and a RH of 98%, the calculated equivalent area is 436 cm^2 for the maximum predicted pit radius of 130 μm. Therefore, the pits on the stainless steels could have been smaller because not enough cathode area was available to reach larger pit sizes. Although before beginning the exposures, the effect of the equivalent cathode area on pit size was not realized, in the future, the impact of the equivalent cathode area on pit size could be examined experimentally with laboratory exposures of coupons of different sizes.

6.3 Geometry of the thin electrolyte

The geometry of the thin electrolyte was found to have a great effect on the depths of the pits observed for the ferric chloride exposures. For the first comparison exposure, two samples with the same loading density and volume of deposited ferric chloride, but with different configurations (i.e., a drop and a thin film) of different areas were examined. Pit depths were larger under the thin film. For the second exposure, two samples with a drop and thin film were examined with the same area but different loading densities and volume of ferric chloride. Two areas were used, one greater than the equivalent cathode area with radius 1.2 cm and one less than the equivalent cathode area with radius 0.38 cm for a predicted pit size. Pits of the same depth were observed under the drop and thin film with area less than the equivalent cathode area. However, when

the area was greater than the equivalent cathode area, pits with larger depths were observed under the drop.

The effect of area on pit size, with different loading densities and volume, can be modeled by first examining the cathodic kinetics. The diffusion limiting current is not dependent on potential for ferric chloride. As mentioned in Section 5.3, as the potential of the alloy drops below the E_{corr}, it immediately enters a diffusion-controlled region. Thus because the diffusion limiting current is not dependent on potential, it is only dependent on area. For areas of the thin film greater than the equivalent cathode, the potential reaches a higher value under the drop than the thin film. A larger integrated area under the potential curve can therefore be calculated for the drop, and the pit depths are higher as shown in Table 5.2. However when the area of the thin film is less than the area of the equivalent cathode, the depths of the pits found under the drop and thin film are approximately the same as a result of similar integrated areas under their potential curves.

Modeling the depth of the pits under a drop and thin film with the same loading density and volume is more difficult because the areas are not the same. In the future, this exposure could be modeled using COMSOL 4, to predict the effect of several parameters.

The thin films of ferric chloride were deposited on the 304L samples, using two different methodologies. For the thin films with the same loading density and volume as the drop experiments, 304L samples first were plasma cleaned to increase their wettability before a volume of ferric chloride was deposited to create a thin film. The thin films in the constant area experiments were created by placing a petri dish on top of

a solution of ferric chloride, causing the solution to spread and form a thin film. As observed in Table 5.1 the predicted pit radius for an environmental condition of 98% RH and 100 μg/cm^2 ferric chloride for a thin film was 75 μm. The plasma-cleaned sample with a thin film had a maximum pit depth 0f 65.3 μm, close in value but bounded by the predicted model value. For a similar environmental condition of 98% RH and 152 μg/cm^2 the predicted pit radius was 102 μm. The maximum pit depth observed on this exposure, however, was much less at 19.1 μm.

The thin films prepared by the plasma cleaning methodology had the closest maximum pit depth values to the predicted pit size for a specific environmental condition. The maximum pit depths under drops shown in both Table 5.1 and 5.2 were smaller than the predicted model values. Additional experiments could be done to examine the effect of plasma cleaning on the corrosion properties of the 304L alloy. The plasma-cleaned samples, however, most closely reassembled the predictions of the computational model.

6.4 Other findings critical to the computational model

Other results for the laboratory exposures such as the appearance of general corrosion and undercutting of pits were not expected but have an effect on the maximum pit depths observed on the samples in comparison to the predicted model values. The effect of cycling the relative humidity on the pit depth, which was not explored experimentally in this study, will be discussed. Lastly, the probability distributions that were calculated, although not the best for the small data set used, could be a useful tool for modeling the maximum pit depths of a larger data set.

6.4.1 Transition from localized corrosion to general corrosion

The ferric chloride exposures were helpful in determining the transition from localized corrosion to general corrosion on both the ferric chloride exposures and the Aermet exposures with deposited sodium chloride. With a decrease in RH and an increase in concentration of ferric chloride, the beginning of general corrosion, along with localized corrosion was observed on the 304L samples as observed in Figures 5.57 and 5.58. For both the 304L ferric chloride and Aermet exposures, with the beginning of general corrosion, higher pit depths were recorded (Figure 5.29). For the 304L and Aermet samples with deposited sodium chloride or ferric chloride, the pit depths also decreased with increasing loading density (Figure 5.29), a trend that was not expected. Usually, an increase in loading density resulted in an increase in maximum pit depth (Figure 5.26).

The higher pit depths on the 304L samples with ferric chloride at low RH, 64%, is likely the result of a decrease in the pit stability product due to the increase in concentration. As mentioned in Section 2.4.1 in Equation 2.14, the saturation concentration usually can be used in place of $D\Delta C$. However, for the case of ferric chloride solutions, the saturation concentration of ferric chloride is approximately 3.4 M, while the concentration corresponding to 64% RH is 2.7 M. Therefore the difference between the two values, 0.7 M is significantly lower than the saturation concentration. Using a ratio of 0.7/3.4, the pit stability product could be approximately one-fourth to one-third the value of the pit stability product using the saturation concentration. The variation of the pit stability product shown in Figure 6.4 indicates that a decrease in the pit stability product to one-third of its original value results in larger pit values for all

loading densities. The observed pit depths detailed in Table 5.2 are bounded by these new predicted model values. Lastly, while with lower relative humidity values the pit depth increased with increasing loading density, for a RH of 64% the pit depth decreased with increasing loading density. This effect could be due to the aggressiveness of the 2.7 M ferric chloride solution, causing more pits to initiate with increasing loading density and thus less current was available to form large pits.

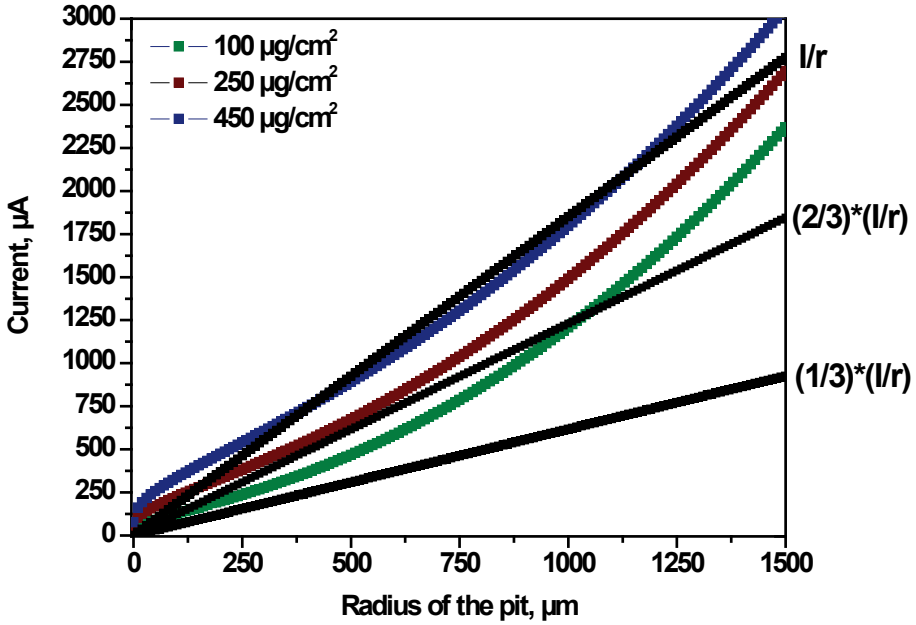

Figure 6.4 Predicted pit depths for a 304L sample with deposited ferric chloride with loading densities 100, 250, and 400 µg/cm^2 increase with a decrease in the pit stability product of two-thirds and one-third of its original value using the saturation concentration.

From these results, a limitation of the computational model is its ability to predict maximum pit size when general corrosion also is occurring. In the future, OLI Systems could be used to model the changing chemical properties of thin electrolyte as a result of general corrosion. These properties could then be incorporated into the model to take into account the effects of general corrosion.

6.4.2 Cyclic relative humidity conditions and efflorescence

Although only the chemical properties of the thin electrolyte associated with static conditions of relative humidity were calculated for the model, materials are exposed to cyclic conditions of relative humidity in the field. Cyclic conditions of relative humidity can have an effect on the initiation of pits. For example, more pits may be initiated on a ferrous alloy with deposited sodium chloride at a lower relative humidity because of the more aggressive nature of the concentrated solution. However, growth of these pits cannot be supported without the necessary area of available cathode. Increasing the relative humidity can improve stability of the pits and growth of the pits can occur. The largest pit size is observed at a static condition of relative humidity. Since the computational model assumes that initiation occurs and its goal is to predict the maximum size to which a pit can grow not pit density, cycling of relative humidity, from low to high, can be ignored in the calculation of maximum pit size.

In the field, however, cycling also can occur in which the relative humidity is lowered until the efflorescence point or crystallization point of the salt. In literature, there is a recognized hysteresis between the deliquescence and the efflorescence points.[40] The drying behavior of corroding surfaces is not well understood, however, so for the purpose of the model, the surface of the alloy was assumed wet above the deliquescence point. In the future, when more research has been done on the drying behavior of corroding surfaces, chemical modeling of efflorescence with OLI Systems could be done to include this effect into the computational model's predictions.

6.4.3 Pit shape

Most of the pits observed on the ferric chloride exposures were close to hemispherical or pan-shaped, in which the radius was larger than the pit depth (Figure 6.5). Undercutting was observed for a 304L sample with a deposited drop of ferric chloride (Figure 5.56), so the radii estimated for the pits could have been less than the true size of the open pit. Pit depth was, therefore, the parameter chosen to quantify the pits observed on the exposure samples because it was the most accurate measurement of pit size that could be determined using the Hirox Digital Microscope.

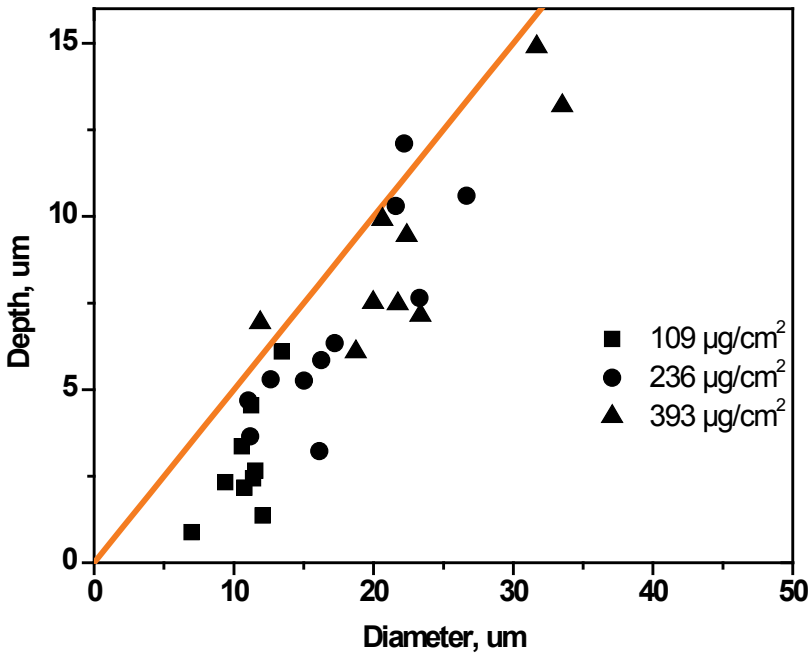

Figure 6.5 Values of pit depth versus pit diameter for 304L with three loading densities 100, 250, and 400 µg/cm^2 ferric chloride indicate pits were hemispherical or pan-shaped.

Since both hemispherical and pan-shaped pits were observed on the exposures, both shapes were examined for their potential to lead to cracking of the material. The higher stress-concentration profiles for hemispherical and pan-shaped pits suggest that

hemispherical pits have a higher likelihood of inducing cracking than pan-shaped pits (Figures 6.6 and 6.7). At the base of the pit, the stress concentration is 2.0 for a hemispherical pit compared to 1.8 for an elongated oval, used as an example similar to a pan-shaped pit. These values indicate that materials are less susceptible to cracking from the pan-shaped pits than hemispherical pits. Therefore, the pan-shaped pits also observed on the exposures are less likely to cause damage in the form of cracking.

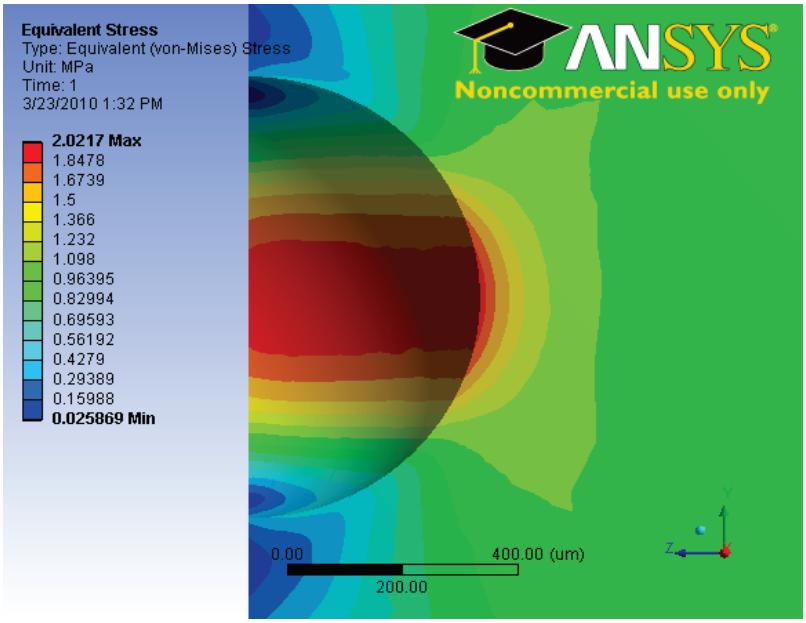

Figure 6.6 A stress-concentration profile for a sphere, representative of a hemispherical pit. Courtesy James T. Burns, University of Virginia.

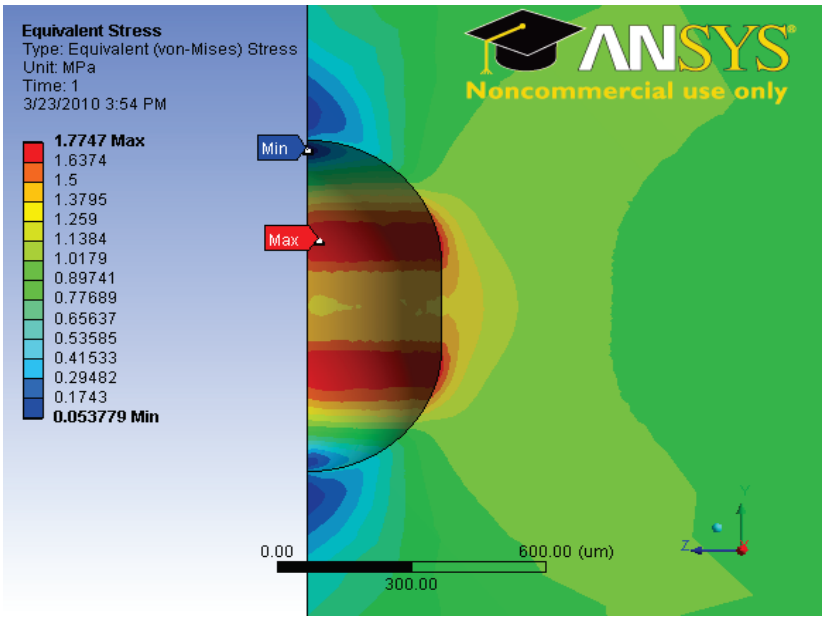

Figure 6.7 A stress-concentration profile for an elongated oval, representative of a pan-shaped pit. Courtesy James T. Burns, University of Virginia.

6.5 Probability of getting a certain size pit

As discussed in Section 5.6.3, the probability distributions obtained for the ferric chloride exposures do not accurately represent the tail of the distribution because a small data set was used and most of the values are clustered on the left end of the distribution (Figure 5.55). However, all of the pit depths for the drop and thin film experiments, unaffected by general corrosion, were bounded by the predicted pit radii. No pit size values greater than this value were observed.

For the Aermet exposures with deposited sodium chloride and the ferric chloride exposures, general corrosion occurred as well as localized corrosion. The pit depths, as mentioned in Section 6.4.1, were larger than the predicted model values. However, though some values exceeded the predicted model values, most of the values were again clustered to the left of the distribution plot.

Although the probability distributions could not be used to accurately show the probability of obtaining maximum pit depths in the tail of the distribution, they did show that with a larger data set they could be a useful tool for determining the probability of observing a certain pit depth.

7 Conclusions

The goal of this work was to evaluate the effectiveness of the computational model developed at the University of Virginia to predict pit radius values that correctly bounded values observed for controlled laboratory exposures. From a series of exposures electrochemical experiments, and chemical modeling performed, the characteristics of the exposures and the input parameters necessary for accurate predictions of maximum pit radius, using the computational model, were determined. These findings will be summarized here in the hope that this information can be used along with the model and other studies on hydrogen uptake and cracking as a tool for accurate prediction of corrosion susceptibility of materials in the field.

Of the experimental parameters input into the model, including the pit stability product, the Tafel slope, the E_{corr}, and the E_{rp}, the E_{rp} was found to have the greatest effect on predicted pit size. As shown in Figure 6.1, the difference between the corrosion potential and the E_{rp} are important in the determination in the pit radius. When the difference between the two potentials is large, and the E_{rp} is at its lowest value, large increases in pit size will be observed. Therefore it is critical to prediction that the Er_p determined experimentally is accurate. For this study the E_{rp} was calculated using the artificial pit method. As the results in Section 5.2 show, with increasing charge density the E_{rp} decreased and eventually leveled off to a constant value, which was reproduced at a even higher charge density.

The chemical properties also were found to have a large effect on predicted pit size. As shown in Table 5.3, properties such as the concentration, density, and conductivity should be determined for each new solution. If they are not, inaccurate pit

radius values will be determined. For additional experiments, if more complicated solutions are used, it will be necessary to model their deliquescence properties using OLI software.

Properties of the exposures, such as area of the coupon exposed and geometry of the thin electrolyte are also critical to simulating conditions similar to that predicted by the computational model. For the predicted maximum pit radius, the equivalent cathode should be determined, and an area similar in value should be used on the coupon for exposure. The geometry of the deposited salt also is important to determine before beginning the exposures. The plasma-cleaned samples with thin films had maximum pit depths that most closely matched the predicted model values. The effect of the plasma cleaning on the corrosion resistance of the alloy, however, should be investigated with additional exposures.

General corrosion was an unexpected observation on the Aermet samples with deposited sodium chloride and on the ferric chloride exposures with a RH value of 64%. Maximum pit depths, overall, increased when general corrosion was observed along with localized corrosion. Variations in the pit stability product with increasing concentration were found to have an effect on pit depth, and future experiments could be done to validate this hypothesis. Currently the occurrence of general corrosion with localized corrosion is a limitation of the computational model and methods to incorporate its effects into the model should be explored in the future.

The cycling of relative humidity, although, it affects the initiation of pits does not affect the maximum size to which a pit can grow, so it was not included in the computational model. In the future, the effects of efflorescence could be included in the

model by using OLI Systems to model the changing chemical properties of the thin electrolyte at the crystallization point.

The pit depth was chosen as the most accurate parameter to use to quantify the pit sizes observed on the exposures. Since undercutting was found to occur, using the radius of the pit observed with a digital microscope would yield values that were smaller than values for the radius at the base of the pit. Hemispherical and pan-shaped pits were observed on the exposures. Stress concentration data indicated that the susceptibility of a material to cracking was worse for hemispherical pits, so the pan-shaped pits observed were not as likely to lead to crack formation.

Finally when interpreting the maximum pit depth data from the exposures, a large data set should be used to fit the values to a probability distribution. With a large data set the probability of obtaining a value larger than the predicted maximum pit depth can be determined. The results from this study indicate that the model will correctly bound the pit depth data and the probability of obtaining a pit depth larger than the predicted value will be small.

8 Recommendations

Thin films of ferric chloride were deposited on 304L samples using a plasma-cleaning procedure. The effects of this plasma-cleaning procedure on the corrosion resistance of the alloy were not investigated. Additional experiments could be done to investigate the effect by varying the length of the plasma cleaning before deposition of the thin film onto samples. These samples then could be exposed to a RH of 98% and values for the maximum pit depths observed could be compared to values obtained in this study for a plasma cleaning time of one hour.

If the plasma cleaning is not found to alter the corrosion resistance of the alloy, this procedure may be used to deposit thin films of sodium chloride on the four alloys. Similar experiments to those done for ferric chloride could be performed to investigate the effect of drops versus a thin film for other solutions, such as sodium chloride. The samples could be exposed to 90 and 95% RH as well as relative humidity values closer to sodium chloride's deliquescence point at 75.5% to investigate the effect of lower relative humidity values on pit depth.

As mentioned earlier, additional experiments could be performed to study the effect of changing the exposed area on the maximum pit depths found under the thin electrolyte. These finding would be helpful in the determination of the area necessary to replicate the atmospheric environmental conditions of the material in the field. The effect of general corrosion also could be studied by looking at the changing chemical properties of the thin electrolyte using OLI software.

Undercutting was observed under thin films of ferric chloride. Cross-sectioning some of the pits obtained on the laboratory exposures with a FIB would help to determine

the extent of undercutting occurring. A profilometer could then be used to scan large sections of the sample to obtain a larger data set for use in probability distributions.

Lastly, comparison of the predicted model values to pit sizes found on outdoor exposures would further validate the computational model, confirming that is reasonable and bounding. The deliquescence properties of the mixed solutions could be determined with OLI, building off the modeling already performed for this study.

References

1. I. Muto, E. Sato, S. Ito, and H. Kihira, in *Proceedings of the International Symposium on Plant Aging and Life Prediction of Corrodible Structures*, NACE, Houston, TX, p. 153 1997.
2. Z. Y. Chen and R. G. Kelly, *J. Electrochem. Soc.*, **157**, C69 (2010).
3. Z. Y. Chen, F. Cui, and R. G. Kelly, *J. Electrochem. Soc.*, **155**, C360 (2008).
4. R.C. Newman, *Nature*, **415** (6873), 743 (2002).
5. M.P. Ryan, D.E. Williams, R.J. Chater, B.M. Hutton, and D.S. McPhail, *Nature*, **415**(6873), 770 (2002).
6. E.G. Webb, T. Suter, R.C. Alkire, *J. Electrochem. Soc.*, **148**, B186 (2001).
7. G.S. Frankel, *J. Electrochem. Soc.,* **145**, 2186 (1998).
8. I.L. Rosenfeld, I.S. Danilov, R.N. Oranskaya, *J. Electrochem.Soc.*, **125**, 1729 (1978).
9. M. Nakata, N. Ono, and Y. Usada, *Corros. Eng.*, **46**, 655 (1997).
10. M. Tochihara, *Corrosion Engineering*, **46**, 679 (1997).
11. P. C. Pistorius and G. T. Burstein, *Philos. Trans. R. Soc. London, Ser. A*, **341**, 531(1992).
12. P. Ernst, N.J. Laycock, M.H. Moayed, and R.C. Newman, *Corrosion Science*, **39** (6), 1133 (1997).
13. J.R. Galvele, J. Electrochem. Soc.,**123** (4), 464 (1976).
14. H. W. Pickering and R. P. Frankenthal, *J. Electrochem. Soc*., **119**, 1297 (1972).

15. K. J. Vetter, *Electrochemical Kinetics*, p. 180, Academic Press, New York (1961).

16. N.J. Laycock and R.C. Newman, *Corrosion Science*, **39**, 1771 (1997).

17. M. H. Moayed and R.C. Newman, *J. Electrochem. Soc.*, **153**, B330 (2006).

18. P. Ernst and R.C. Newman, *Corrosion Science,* **44**, 927 (2002).

19. P. Ernst and R.C. Newman, *Corrosion Science,* **44**, 943 (2002).

20. J. W. Tester and H.S. Isaacs, *J. Electrochem. Soc*., **122**, 1438 (1975).

21. G.S. Frankel, *J. of ASTM International* **5**, 1 (2008).

22. G.T. Gaudet, W.T. Mo, T.A. Hatton, J.W. Tester, J. Tilly, H.S. Isaacs, and R.C. Newman, *AIChE Journal*, **32**, 949 (1986).

23. H.S. Isaacs and R.C. Newman*, Corrosion Chemistry Within Pits, Crevices and Cracks*, HSMO, London (1987).

24. B.E. Wilde and E. Williams, *J. Electrochem. Soc.,* **118**, 1057 1971.

25. B.E. Wilde, in: R.W. Staehle, B.F. Brown, J. Kruger, A. Agarwal (Eds.), *Localized Corrosion*, NACE International, Houston, TX, p. 342, (1974).

26. N. Sridhar, D.S. Dunn, M. Seth, *Corrosion,* **57**, 598 (2001).

27. A. Anderko, N. Sridhar, D.S. Dunn, *Corrosion Science*, **46**, 1583 (2004).

28. B.A. Kehler, G.O. Ilevbare, J.R. Scully, *Corrosion*, **57**, 1042 (2001).

29. D.S. Dunn, G.A. Cragnolino, N. Sridhar, *Corrosion*, **56**, 90 (2000).

30. Data courtesy of Shinohara, Tahara, Hosoya, National Institute for Materials Science, Japan, Personal communication.

31. A. Anderko, et al., *Fluid Phase Equilibria*, **194**, 123 (2002).

32. P. Wang, et al., *Fluid Phase* Equilibria, **203**, 141 (2002).

33. T. Engel and P. Reid, *Physical Chemistry*, pp, 230-235, Pearson Education, San Francisco, (2006).

34. M. Gruszkiewicz *et al., Journal of Solution Chemistry*, **36**, 723 (2007).

35. E. Schindelholz and R. G. Kelly, *Electrochem. and Solid-State Letters,* **13** (10) C29 (2010).

36. N. Sridhar, C. S. Brossia, D. S. Dunn, and A. Anderko, *Corrosion,* **60**, 915 (2004).

37. A. Anderko, OLI Systems, Morris Plains, NJ, Personal communication.

38. R.C. Newman, *Corr. Sci.,* **25**(5), 331 (1985).

39. J. Seinfeld and S. Pandis, *Atmospheric Chemistry and Physics*, p. 519, Wiley and Sons, New York, (1996).

40. I.N. Tang, *Symposium on Biological Studies of Environmental Pollutants: Aerosol Generation and Exposure Facilities,* Honolulu, Hawaii, 1979.

Appendix A

Pit depth determination in Mountains Map

The automated procedure to calculate the pit depth created in Mountains Map Imaging Topography 6.0 is as follows. A three-dimensional image of the pit was first leveled using least square planes. The axis values were changed to absolute values, and the entire image was then mirrored along the z-axis. A Gaussian filter was then applied to reduce the waviness of the surface, and lastly, a procedure to determine the volume of the islands was performed. The pits were now inverted and examined as islands. This procedure determined not only the volume of the islands but also calculated the pit depth (height when inverted) and area. The pit radius was determined by eye using a filter to outline the area of the pit.